

# Accelerated MR Thermometry for High Intensity Focused Ultrasound Therapy

Author: Chang-Sheng Mei

Persistent link: <http://hdl.handle.net/2345/2425>

This work is posted on [eScholarship@BC](#),  
Boston College University Libraries.

---

Boston College Electronic Thesis or Dissertation, 2011

Copyright is held by the author, with all rights reserved, unless otherwise noted.

Boston College

The Graduate School of Arts and Sciences

Department of Physics

ACCELERATED MR THERMOMETRY FOR  
HIGH INTENSITY FOCUSED ULTRASOUND  
THERAPY

a dissertation

by

**CHANG-SHENG MEI**

submitted in partial fulfillment of the requirements

for the degree of

**Doctor of Philosophy**

December 2011

© copyright by CHANG-SHENG MEI

2011

# **ACCELERATED MR THERMOMETRY FOR HIGH INTENSITY FOCUSED ULTRASOUND THERAPY**

by

**Chang-Sheng Mei**

**Research Advisors: Prof. Nathan J. McDannold,  
Prof. Lawrence P. Panych, and Prof. Bruno Madore**

## **Abstract**

The purpose of this dissertation was to investigate the temporal limit on the ability to measure temperature changes using magnetic resonance imaging (MRI). The limit was examined in experiments using a variety of imaging techniques for MRI-based temperature measurements. We applied these methods for monitoring temperature changes in focused ultrasound (FUS) heating experiments.

FUS is an attractive alternative to surgical resection due to its noninvasive character. FUS treatments have been successfully conducted in several clinical applications. MRI and MR thermometry is a natural choice for the guidance of FUS surgeries, given its ability to visualize, monitor, and evaluate the success of treatments. MR thermometry, however, can be a very challenging application, as good resolution is often needed along spatial, temporal as well as temperature axes. These three quantities are strictly related to each other, and normally it is theoretically impossible to simultaneously achieve high resolutions for all axes. In this dissertation, techniques were developed to achieve this at cost of some reduction in spatial coverage.

Given that the heated foci produced during thermal therapies are typically much smaller than the anatomy being imaged, much of the imaged field-of-view is not actually being heated and may not require temperature monitoring. By sacrificing some of the in-plane spatial coverage outside the region-of-interest (ROI), significant gains can be obtained in terms of temporal resolution. In the extreme, an ROI can be chosen to be a narrow pencil-like column, and a sampling time for temperature imaging is possible with a temporal resolution of a few milliseconds.

MRI-based thermal imaging, which maps temperature-induced changes in the proton resonance frequency, was implemented in two projects. In the first project, three previously described, fast MR imaging techniques were combined in a hybrid method to significantly speed up acquisition compared to the conventional thermometry. Acceleration factors up to 24-fold were obtained, and a temporal resolution as high as 320 milliseconds was achieved. The method was tested in a gel phantom and in bovine muscle samples in FUS heating experiments. The robustness of the hybrid method with respect to the cancellation of the fat signal, which causes temperature errors, and the incorporation of the method into an ultrafast, three dimensional sequence were also investigated. In the second project, a novel MR spectroscopic sequence was investigated for ultrafast one-dimension thermometry. Temperature monitoring was examined during FUS sonications in a gel phantom, SNR performance was evaluated in vivo in a rabbit brain, and feasibility was tested in a human heart. It was shown capable in a FUS heating experiment in a gel phantom of increasing temporal resolution to as high as 53 milliseconds in a three Tesla MRI. The temporal resolution achieved is an order of

magnitude faster than any other rapid MR thermometry sequences reported. With this one-dimensional approach, a short sampling time as low as 3.6 milliseconds was theoretically achievable. However, given the SNR that could be achieved and the limited heating induced by FUS in the gel phantom in a few milliseconds, any temperature changes in such a short period were obscured by noise. We have analyzed the conditions whereby a temporal resolution of a few-milliseconds could be obtained.

## Acknowledgements

I would like to express my deep and sincere gratitude to my thesis advisors Profs. Nathan J. McDannold, Lawrence P. Panych, and Bruno Madore, for their extraordinary supervision throughout my graduate career. It has been my great pleasure to work with Prof. McDannold, one of the top scientists and pioneers in the field of our study. He is a great supervisor and shows immense enthusiasm in research. I am extremely indebted to Prof. Panych, for his patience, guidance, and hands-on mentorship, and to Prof. Madore for his invaluable input and great encouragement. I feel proud to be their student. Their guidance will remain with me always, wherever my career takes me.

I would like to thank to Prof. Michael Graf. I couldn't have conducted my thesis without his constant support. I would also like to thank to Prof. Robert V. Mulkern, for his mentorship and inspiration, and to Prof. Oshio for his kind help providing his research imaging sequence.

My heart is full of thankfulness to the faculty and staff of Physics Department at Boston College. To Profs. Uritam and Naughton, I thank you heartily for allowing me doing research of my interest off-campus without any discontinuity of the mental and financial support. To Profs. Bedell, Kalman, and Ren, for being a role model as successful researchers. To Prof Haines, for helping me, academically and mentally, all the way through my long year of graduate study. And to Susan Hoban, Joyce Light, Nancy Chevy, and Gisele Byda, I thank you for settling me down working at Brigham and Women's Hospital, Harvard Medical School. I do know the administrative business between BC and BWH is full of tediousness and sometimes frustration.

It has been my luck and honor to be a member in both groups at different periods: the Focused Ultrasound Laboratory and Medical Imaging Physics Group. I am grateful to all the current and former members. I am especially grateful to Lisa Treat, Jason White, E.J. Park, Yun Jing, Jing Yuan, Renxin Chu, and George Chiou for their contribution to this thesis research, and to Greg Clement, Natalia Vykhodtseva, Yongzhi Zhang, Juyoung Park, Faik Can Meral, Costas Arvanitis, Keiko Fujiwara, Krisztina Fisher, Ben Schwartz, Cheng-Chieh Cheng, and Muna Aryal for their warm and pleasant collegueship.

I could not have thanked more to the dearest friends of my family: Wen-yu Vicky Haines, Jeff Lin, Jinger Ning, and Mandy Huang. Thanks for taking care of my family whenever the overwhelming workload has fell upon me. I also want to express my sincere gratitude to my best friends: Fo-Ming Liu and Ching-Ting Pi for their encouraging support. You deserve the share in my joy of the thesis' completion.

I owe my loving thanks to my wife Wan-Mei Wei, for her endless support, and my special thanks to my mother in law, for her continued affection. Most importantly, I wish to thank my parents, for their unconditional love. To them, I dedicate this dissertation.

# Table of contents

<b>1</b>	<b>INTRODUCTION.....</b>	<b>11</b>
1.1	MOTIVATION .....	11
1.2	FOCUSED ULTRASOUND (FUS) .....	14
1.2.1	Background .....	14
1.2.2	MR-guided FUS thermal ablation .....	17
1.3	MAGNETIC RESONANCE IMAGING (MRI) .....	20
1.3.1	Radio frequency (RF) excitation .....	20
1.3.2	Magnetic gradients .....	21
1.3.3	k-space.....	22
1.3.4	Pulse sequences .....	28
1.3.4.1	Spin echo sequence .....	28
1.3.4.2	Gradient echo sequence (GRE) .....	30
1.3.4.3	Echo planar imaging (EPI) .....	32
1.4	MRI THERMOMETRY .....	35
1.4.1	Introduction .....	35
1.4.2	Temperature sensitive MR parameters .....	35
1.4.2.1	T1 relaxation time .....	35
1.4.2.2	T2 relaxation time .....	36
1.4.2.3	Proton Density .....	37
1.4.2.4	Diffusion-Brownian molecular motion .....	38
1.4.3	The temperature sensitivity of the water proton resonance frequency (PRF).....	39
1.4.3.1	Magnetic field in matter .....	39
1.4.3.2	Temperature dependence of the local magnetic field .....	40
1.4.3.3	Temperature mapping using PRF shift.....	42
1.4.3.4	Source of error .....	44
1.5	SCOPE OF THIS DISSERTATION .....	47
<b>2</b>	<b>EXPERIMENTAL METHODS.....</b>	<b>51</b>
2.1	ULTRASOUND .....	51
2.2	MRI .....	54
2.3	EXPERIMENTAL SET-UP .....	55
2.3.1	MR-compatible FUS positioning system .....	55
2.3.2	MR-compatible FUS system for use in MRI array receivers .....	56
2.4	ADVANCED MRI TECHNIQUES .....	58
2.4.1	Volume-selective two-dimensional RF (2DRF) excitation .....	58
2.4.2	Unaliasing by Fourier-encoding the overlaps using the temporal dimension (UNFOLD) .....	61
2.4.3	Multiple receiver coil technology (parallel imaging) .....	64
<b>3</b>	<b>COMBINING VOLUME-SELECTIVE RF PULSE WITH PARALLEL IMAGING AND UNFOLD FOR ACCELERATED MR THERMOMETRY IMAGING.....</b>	<b>69</b>
3.1	INTRODUCTION .....	69
3.2	THEORY .....	71
3.2.1	Reduced FOV imaging using 2DRF excitation .....	71
3.2.2	Artifact removal using UNFOLD and parallel imaging .....	74
3.3	MATERIALS AND METHODS .....	76
3.3.1	Imaging pulse sequences .....	76
3.3.2	FUS experimental setup .....	76
3.3.3	2D thermometry in gel phantom .....	77
3.3.4	2D thermometry in bovine muscle .....	78
3.3.5	3D thermometry in gel phantom .....	79

3.3.6	Real-time processing and display .....	79
3.3.7	Image reconstruction .....	80
3.3.8	Statistical analysis .....	82
3.4	RESULTS .....	83
3.4.1	2D thermometry .....	83
3.4.2	3D thermometry .....	89
3.4.3	Real-time processing and display .....	91
3.5	DISCUSSION AND CONCLUSIONS .....	93
<b>4</b>	<b>ULTRAFAST 1D MR THERMOMETRY USING PHASE OR FREQUENCY MAPPING .....</b>	<b>99</b>
4.1	INTRODUCTION .....	99
4.2	MATERIALS AND METHODS .....	100
4.2.1	Line scan echo planar spectroscopic imaging (LSEPSI) sequence .....	100
4.2.2	Heating experiments .....	102
4.2.2.1	Calibration experiments .....	102
4.2.2.2	Rapid measurement experiments .....	105
4.2.2.3	LSEPSI temperature estimation .....	105
4.2.3	In vivo experiments .....	107
4.2.3.1	Rabbit brain imaging .....	107
4.2.3.2	Volunteer imaging .....	108
4.3	RESULTS .....	109
4.3.1	Phase mapping .....	109
4.3.1.1	Calibration experiments .....	109
4.3.1.2	Rapid measurement experiments .....	111
4.3.1.3	Rabbit brain imaging .....	113
4.3.2	Frequency mapping .....	115
4.3.2.1	Volunteer imaging .....	115
4.4	DISCUSSION AND CONCLUSIONS .....	118
<b>5</b>	<b>SUMMARY .....</b>	<b>125</b>
<b>6</b>	<b>APPENDIX A: THE IMPLEMENTATION OF THE HYBRID METHOD IN AN ADIPOSE PHANTOM.....</b>	<b>129</b>
6.1	INTRODUCTION .....	129
6.2	MATERIALS AND METHODS .....	130
6.3	RESULTS .....	134
6.4	DISCUSSION .....	137
<b>7</b>	<b>APPENDIX B: THE MODIFICATION OF THE HYBRID METHOD FROM GRE TO EPI..</b>	<b>139</b>
7.1	INTRODUCTION .....	139
7.2	MATERIALS AND METHODS .....	141
7.3	RESULTS .....	146
7.4	DISCUSSION .....	149
<b>8</b>	<b>APPENDIX C: PUBLICATION LIST .....</b>	<b>151</b>
PUBLICATIONS	.....	151
CONFERENCE PROCEEDINGS	.....	151
<b>9</b>	<b>APPENDIX D: ABBREVIATIONS.....</b>	<b>153</b>
<b>10</b>	<b>REFERENCES.....</b>	<b>155</b>

## List of Figures

Figure 1-1: $k$ -space sampling function during a frequency-encoding gradient.....	22
Figure 1-2: A GRE sequence vs. its $k$ -space path.....	23
Figure 1-3: A variety of $k$ -space trajectories.....	25
Figure 1-4: The timing diagram of a spin echo sequence.....	26
Figure 1-5: The timing diagram of a GRE sequence.....	28
Figure 1-6: The timing diagram of a spin-echo based EPI sequence.....	30
Figure 2-1: An eight-element sector-vortex array transducer.....	49
Figure 2-2: Ultrasound beam plots of a sector vortex (1.1 MHz) transducer in modes 0-4.....	50
Figure 2-3: Scheme for the MR-compatible FUS positioning system.....	51
Figure 2-4: Axial view of the FUS set-up within MRI bore.....	52
Figure 2-5: The 2DRF pulse vs. its excitation $k$ -space trajectory.....	56
Figure 2-6: Sampling scheme for UNFOLD in acquisition $k$ -space.....	59
Figure 2-7: Demonstration of UNFOLD modulation in a homogeneous doped water phantom...59	59
Figure 2-8: Example of an array coil configuration.....	60
Figure 2-9: Schematic representation of the SENSE reconstruction with four receiver coils.....	61
Figure 2-10: Sampling scheme for parallel imaging.....	62
Figure 3-1: 2DRF excitation profiles depend on 2DRF-pulse parameters.....	69
Figure 3-2: The hybrid 2DRF excitations and SENSE plus UNFOLD filtering were tested on a GE 3T scanner by imaging a homogeneous doped water phantom.....	71
Figure 3-3: MR temperature measurements and numerical simulations from the ROI at the focus of heating.....	80
Figure 3-4: Temperature maps of the time frames with the maximum heating.....	81

Figure 3-5: Scatterplots (top) and Bland-Altman plots (bottom).....	83
Figure 3-6: Temperature changes of the hottest voxel of 6 middle slices.....	86
Figure 3-7: Screen snapshot from 3D-Slicer.....	88
Figure 4-1: Diagram of an LSEPSI pulse sequence.....	96
Figure 4-2: Imaging prescription for both SPGR and LSEPSI sequences.....	99
Figure 4-3: The cross section of the scan column superimposed on a 2D image.....	100
Figure 4-4: Results of LSEPSI calibration experiments.....	105
Figure 4-5: The time evolution of the 1D LSEPSI images and the temperature changes in the focus.....	108
Figure 4-6: Noise levels in °C and radians for two TR datasets.....	110
Figure 4-7: Spectroscopic analysis along TE and TR dimensions from cardiac images.....	112
Figure 6-1: The waveform of the echo-planar 2DRF pulse used for fat suppression and rFOV imaging.....	126
Figure 6-2: Excitation profile in a water-oil phantom.....	127
Figure 6-3: Excitation profile in a cheese phantom.....	128
Figure 6-4: The temperature map of the time frame with the maximum heating in a cheese experiment.....	131
Figure 6-5: Temperature changes of the hottest voxel in 2D cheese experiments.....	131
Figure 6-6: Temperature changes of a 3×3 ROI within focus for five (out of eight) slices in the 3D cheese heating experiments.....	132
Figure 7-1: The modified 3D-EPI pulse sequence diagram in one TR.....	137
Figure 7-2: Diagram of the 3D <i>k-space</i> sampling function, for UNFOLD-GRAPPA acquisition.....	139
Figure 7-3: Experimental set-up for the human skull heating experiments.....	141
Figure 7-4: MR temperature measurements using 3D EPI in the gel heating experiment.....	142

Figure 7-5: Thermal maps of various slices with the maximum temperature rises in the skull heating experiments.....144

## List of Tables

Table 3-1: Noise propagation considerations for Bland-Altman plots.....	84
Table 3-2: TNR estimation for scenarios involving different sequences.....	92
Table 4-1: LSEPSI sequence parameters used in the experiments.....	97
Table 9-1: Abbreviations used in this thesis.....	149

# 1 Introduction

## 1.1 Motivation

Thermal ablation using RF, microwave, laser, or focused ultrasound (FUS) devices offers minimally-invasive alternatives to surgical resection. FUS is of particular interest due to its non-invasive nature and successful treatments in several clinical applications [1]. Magnetic resonance imaging (MRI) has been recognized as the best thermometry for FUS surgery in terms of visualization, monitoring, and evaluating success of the treatments. MR thermometry is made possible by the fact that several MR parameters exhibit a temperature-dependence. Among these parameters, the measurement of water proton resonance frequency (PRF) [2, 3] is currently the most practical means available to map quantitative temperature changes in vivo. The water PRF shifts linearly with temperature in the range of interest for thermal ablation [4]. It can be mapped using spectroscopic imaging to detect the water proton chemical shift between the water peak and a reference peak that remains constant with temperature, such as lipids [5]. Alternatively, one can use the phase change resulting from the temperature-induced PRF shift with a gradient echo (GRE) imaging sequence. Both approaches are able to quantitatively monitor tissue temperature.

PRF-shift thermometry, however, is associated with difficult challenges in terms of imaging performance. Because of the large thermal gradients and rapid temperature changes produced during thermal ablation, temporal resolution must be sufficient to capture important temporal variations, both temperature- and motion-induced. Furthermore, spatial resolution must be reasonably high to accurately locate the edges of

the ablated volume (where thermal gradients are large) and the focal point [6]. For example, the focal region produced by the ExAblate 4000 Transcranial MR-guided focused ultrasound (TcMRgFUS) system (InSightec, Haifa, Israel) is roughly 3.0x3.0x5.8 mm (as provided by the manufacturer), and resolution should thus be significantly better than 3 mm to resolve it. Spatial coverage may also be important, to detect possible secondary (unintended) heating sites and avoid damage to healthy tissues.

Several approaches have been proposed to speed-up the image acquisition process in temperature mapping. For example, echo-planar [7, 8] and spiral [9] techniques can achieve sub-second temporal resolution for one image plane, with temperature sensitivity comparable to the gradient echo technique. The use of fast imaging sequences such as PRESTO [10, 11] and SSFP [12-14] has also been investigated, and parallel imaging has been proposed to accelerate the image acquisition process [15, 16]. However, especially in the presence of motion and despite promising recent developments [17], further imaging speed is still very much needed in PRF thermometry, to achieve 3D coverage with sufficient spatial and temporal resolution.

In this thesis, we investigated methods that increase temporal resolution by sacrificing some spatial coverage outside the region-of-interest (ROI). In MR temperature mapping to monitor thermal ablation methods such as FUS, only the certain portions of the FOV in which heat is concentrated may be of interest. By selecting a reduced FOV (rFOV), fewer  $k$ -space lines are needed to achieve the same spatial resolution, leading to faster imaging. However, simply reducing the imaging FOV is normally unacceptable because it typically results in aliasing artifacts (also called “wraparound” artifacts). A

straightforward way to avoid such artifacts is to avoid exciting spins outside the desired ROI, as can be done using 2D spatially-selective RF (2DRF) excitation pulses [18, 19]. Such pulses perform a spatial selection along the slice direction in addition to selecting a limited region in the phase-encoding direction. Alternatively, one can select a narrow pencil-like column of interest (i.e., the FUS focal region) can be contained within such a region. This can be done using orthogonal  $90^\circ$  and  $180^\circ$  slice selective RF pulses, which form a spin echo from in the column at the intersection of two planes (see section 4.2.1 for details). By confining the excitation to such regions, we significantly speed up the imaging acquisition process while maintaining high spatial resolution. Acceleration factors as high as 24 were obtained with the rFOV method in the first project, and a sampling time as low as 53 ms was achieved with the column excitation in the second project.

## **1.2 Focused ultrasound (FUS)**

### *1.2.1 Background*

Ultrasound can be created by applying an oscillating electrical voltage to a piezoelectric material, such as certain crystals or ceramics, which responds with mechanical deformation in proportion to the applied voltage. The expansion/contraction of the material leads to the condensation/rarefaction of its surrounding medium, such as air or water, and results in mechanical pressure waves. These waves are considered “ultrasound” when the frequency is greater than the upper limit of human hearing, which is approximately 20 kHz in healthy adult. The piezoelectric effect can work conversely; mechanical stress applied to such material can also induce a voltage. Thus piezoelectric transducers can be used both to generate and receive ultrasonic signals.

A mechanical wave is attenuated as it propagates through tissue due to scattering and absorption. The absorbed mechanical energy is mostly converted to heat. Ultrasound has a relatively low absorption rate in soft tissue; the field can penetrate deep into tissue [20]. However, when the ultrasound waves encounter interfaces in the media, differences in density and sound speed result in reflection, refraction, and diffraction at the interface. These effects can be large when there is a large mismatch in acoustic impedance, severely reducing energy transmission. Bone and air-filled tissues in particular have acoustic impedances substantially different than soft tissue. Accordingly, the use of ultrasound using extracorporeal transducers is generally limited in regions of the body, such as the lungs, digestive tract, and brain, where interfaces occur between soft tissue and gas or bone [21].

The therapeutic use of ultrasound is made possible by its ability to be focused. By spherically curving a piezoelectric transducer, the ultrasound field can be focused in a fairly small region and thus it is possible to locally target a specific the ROI (such as a tumor) while leave the surrounding tissues unharmed. The size of the focal region is determined jointly by the geometry of the piezoelectric material and the ultrasound frequency [21]. For example, a single-element transducer with a diameter of 100 mm, radius of curvature of 80 mm, and resonant frequency of 1.7 MHz can produce a tight ellipsoid focal spot with diameter and length of 1 mm and 4 mm, respectively, at half-maximum pressure amplitude. Tissue volumes are treated by steering the focal point to different points. The distribution of the energy and the resulting heated region can be further controlled with the use of acoustic lenses [22, 23] or phased array transducers [24-27].

Therapeutic applications of FUS can be achieved with thermal and mechanical effects. Mechanically-induced bioeffects are generally produced via interactions between the ultrasound field and microbubbles. These microbubbles can be produced from microscopic gaseous nuclei that are present in tissues. Pre-formed microbubbles (ultrasound contrast agents) can also be introduced into the acoustic field by intravenous injection. The interaction between the sound field and the microbubbles is referred to as cavitation. The bubbles oscillate in the acoustic pressure wave, and during the negative pressure phase will grow via rectified diffusion. At high pressure amplitudes, the bubbles will violently collapse during the positive phase, producing shock waves, high-velocity jets, and tissue damage. Cavitation-induced bioeffects, either by radial oscillation (stable

cavitation) or by violent collapse (inertial cavitation) [28], can be exploited for different ultrasound therapies. These interactions also can be used to enhance ultrasound-induced heating [29].

In an absorbing medium such as tissue, ultrasound energy is absorbed and converted to a temperature rise. Therapeutic uses of thermal effects can be generally divided into two regimes: hyperthermia and ablation. In hyperthermia, temperatures in the range of 43–45°C are applied for a time of several tens of minutes to kill cancer cells directly or to sensitize them to cytotoxic agents and/or radiation [30], while in thermal ablation, temperatures in the range of 50–80°C (or higher) are applied to thermally coagulate the tissue and induce necrosis through processes such as protein denaturation [31], while in thermal ablation, temperatures in the range of 50–80°C (or higher) are applied to thermally coagulate the tissue and induce necrosis through processes such as protein denaturation [31]. If the acoustic and thermal properties of tissue are known, the temperature rise induced can be predicted through relatively straightforward models [32]. However, in practice these parameters are not known with precision and it necessary to monitor the temperature during the procedure to ensure that a sufficient temperature rise is achieved. Perfusion, in particular, can have a large impact on the magnitude and distribution of the heated region. To minimize the effects of perfusion, focused ultrasound ablation is often performed using short (~1-30 second) sonications [33].

Mechanical and thermal bioeffects induced by focused ultrasound at therapeutic frequencies ranging from 0.5 to 10 MHz has prompted investigation into numerous procedures for the treatment of disease, such as tumor and tissue ablation [34],

hemostasis [35], and modification of vascular or tissue permeabilities to locally enhance drug delivery [36].

### *1.2.2 MR-guided FUS thermal ablation*

The promise of FUS as a therapeutic tool and its ability to be used in a number of different organs has led to intense interest in this technology for more than 60 years. In 1942, the therapeutic use of FUS was first suggested by Lynn et al [37]. In the 1940's and 50's extensive experiments were performed. During this time, William and Francis Fry performed groundbreaking work with FUS in the treatment of brain disorders [38, 39]. In the 1960's Lele demonstrated that over a wide range of parameters, thermal effects resulting from ultrasound absorption could explain tissue damage resulting from high intensity FUS [40, 41]. Since these fundamental initial works, FUS has been performed in various organs and diseases [42, 43]. Thousands of patients have been treated with FUS ablation in Europe and Asia under guidance by ultrasound imaging [44].

The acceptance of FUS in clinical practice in the United States, however, has been slow. This is mainly because of the difficulty in planning, monitoring, and assessing the success of the treatment. This difficulty was not adequately addressed until the development of MR-guided focused ultrasound surgery (MRgFUS) in the 1990s. The first device, developed by General Electric, used robotics to steer a single-element transducer in a MR magnet [45, 46]. These experiments demonstrated the feasibility of using MRI for monitoring and guiding FUS surgery and led to the first clinical MRgFUS treatments of breast tumors [47-49]. Since the initial work, MRI-compatible phased array transducers have been developed. These arrays can electronically steer the focal point

during sonication, increasing the size of the focal region and enabling larger tissue volumes to be ablated and reducing the length of time required for the procedure. The successful integration of FUS with MRI guidance, along with this development of phased arrays, has brought FUS to a new era in clinical practice.

Following initial research [45, 50], InSightec (Haifa, Israel) developed the ExAblate 2000 system, which is the first commercially available prototype for MRgFUS therapy delivery device and was approved by the U.S. Food and Drug Administration in 2004 for the treatment of uterine fibroid. This system houses all of the electronics and the phased array transducer in a sealed water bath incorporated into a custom-built scanner table in a General Electric 1.5T MR magnet. The ExAblate 2000 has been tested extensively in clinical trials for the treatment of uterine fibroids. Since then, the device has been employed for the treatment of other lesions such as the palliation of bone metastases, currently in clinical trials. In a recent work, a transcranial MR-guided FUS system ExAblate 4000 was developed for the treatment of brain tumor [51, 52]. This device has been shown to be capable of delivering the acoustic field through the intact skull and thermally ablate tumor in the brain.

As MRgFUS devices and treatments have advanced, it has become clear that more advanced MR imaging techniques for thermometry needed. An ideal guidance requires real-time quantitative monitoring of the temperature distribution in three dimensions. MRI-based temperature measurements have been tested and validated [53-55] and shown accuracy in temperature quantification [56]. With MR thermometry, it is possible to monitor the temperature distribution in the ablated zone in real time, if the

imaging is fast enough, and to determine estimate which tissues have reached a sufficient thermal dose for tissue damage based on the temperature history [57, 58].

Currently, clinical MRgFUS systems only monitor the temperature distribution in only a single or a few imaging planes, which is insufficient to monitor the entire heated region. The primary concern of this thesis is to investigate methods to accelerate the acquisition of MRI for temperature measurements. In the following sections, an overview of MRI (section 1.3) and MR thermometry (section 1.4) are provided.

## 1.3 Magnetic resonance imaging (MRI)

### 1.3.1 Radio frequency (RF) excitation

When a randomly distributed nuclear spins are placed in an external magnetic field  $\mathbf{B}_0$ , a net magnetization vector  $\mathbf{M}_0$  is formed and precesses around the axis of  $\mathbf{B}_0$  (conventionally defined in the  $z$  axis) at the Larmor frequency. At equilibrium this magnetization is aligned along the  $z$  axis (the longitudinal axis) and the component of the magnetization vector in the transverse plane ( $x$ - $y$  plane) is zero.

An excitation magnetic field oscillating at the Larmor frequency, denoted by  $\mathbf{B}_1$ , can be applied to tip the magnetization vector away from the main magnetic field axis ( $z$ ). Once a component of  $\mathbf{M}_0$  lies in the transverse plane, MR signal can be detected as the magnetization rotating at the Larmor frequency induces an alternating current in a receiver coil. There must be at least one excitation pulse in every MR pulse sequence in order to create a signal that can be detected.

The excitation magnetic field is implemented by turning on a modulation envelop (usually a sinc function) for a short period of time (typically 100  $\mu\text{s}$  to 5 ms) with frequency in the radio frequency (RF) range (e.g., 128 MHz which is the Larmor frequency for a 3-Tesla magnet). An on-resonance RF field directed perpendicular to  $\mathbf{B}_0$  is able to tip (or flip) the magnetization toward the transverse plane. Derived from the Bloch equations in the rotating reference frame, the flip angle is:

$$\theta = \gamma \int_{t'=0}^t B_1(t') dt' \quad (1-1)$$

where  $\gamma$  is the gyromagnetic ratio in units of radians per second per Tesla, and  $\mathbf{B}_1(t)$  is the RF modulation envelope. If the  $\mathbf{B}_1$  field is strong enough and applied long enough to tip the net magnetization by  $\pi/2$ , all of the longitudinal magnetization is converted to the transverse magnetization (90° RF pulse).

### 1.3.2 Magnetic gradients

A magnetic imaging gradient is a magnetic field designed to increase in strength along a particular direction. The strength of a gradient refers to the rate at which the gradient changes with distance. These gradients are small perturbations superimposed on  $\mathbf{B}_0$ , with a typical strength producing a total field variation of less than 1%. The maximum gradient strength for a clinical MR scanner is about 40 mT/m. These gradients change linearly in distance, so that the total magnetic field can be made linearly dependent on the location inside the magnet. For instance, in  $x$  direction, when the  $x$  imaging gradient is activated, the magnetic field is:

$$B_x = B_0 + G_x(t)x \quad (1-2)$$

Where  $B_x$  is the magnetic field at location  $x$  and  $G_x$  is the gradient amplitude applied at time  $t$ . Magnetic field gradients are activated (typically as constants) for a short period of time at carefully timed moments during the MR scan and referred to as gradient pulses. The rate of change in magnetic gradients, when the fields are switched on and off, is called slew rate. The maximum slew rate for the GE 3-Tesla magnet used in most of this work is 150 T/m/s.

The purpose of magnetic gradients is to spatially encode information contained in the MR signal along the  $x$ ,  $y$ , and  $z$  directions. These three directions are called “logical

directions”. They are different from “physical directions” where  $z$  is aligned with  $\mathbf{B}_0$ , and  $x$  (and  $y$ ) is normal to  $\mathbf{B}_0$ . Logical directions are somewhat arbitrary and depend on the image prescription. Conventionally, the  $z$  gradient is applied perpendicular to an image plane and is named the ‘slice selection gradient’ while  $x$  and  $y$  gradients are applied parallel to the plane and are named ‘frequency’ and ‘phase’ encoding gradients, respectively. Since data is sampled while the frequency-encoding gradient is turned on, it is also called readout gradient.

### 1.3.3 $k$ -space

The concept of  $k$ -space in MRI is defined as a 2D or 3D Fourier transform of the MR image measured. It is a temporary image space, containing complex values in a matrix, in which data from digitized MR signals are stored during data acquisition. A one-dimensional  $k$ -space is first examined in a one-dimensional spin system. Consider a series of spins arranged in a one-dimensional array at locations  $x_1, x_2, x_3, \dots, x_n$  along the  $x$  axis with spin densities  $\rho_{x_1}, \rho_{x_2}, \rho_{x_3}, \dots, \rho_{x_n}$ . With the gradient  $G_x$  applied (Eq. 1-2), each spin  $j$  has a distinct Larmor frequency:

$$\omega_{x_j}(t) = \gamma(B_0 + G_x(t)x_j) \quad (1-3)$$

where  $\gamma$  is gyromagnetic ratio in radians per Tesla per second. In a reference frame rotating with frequency of  $\omega = \gamma B_0$ , Eq. 1-3 can be simplified to:

$$\omega_{x_j}(t) = \gamma G_x(t)x_j \quad (1-4)$$

The phase accrued by spins  $j$  due to the gradient is:

$$\phi_{x_j}(t) = \int_0^t \omega_{x_j} d\tau = \gamma x_j \int_0^t G_x(\tau) d\tau \quad (1-5)$$

where the time origin is defined at the initial moment of the frequency-encoding gradient.

The MR signal  $S_x$  in the transverse plane can be obtained by summing up all the spin vectors weighted by their spin densities:

$$S_x = \sum_{j=1}^n \rho_{x_j} e^{-i\phi_{x_j}} \approx \int_{-\infty}^{\infty} \rho(x) e^{-i\phi(x,t)} dx \quad (1-6)$$

where  $\rho(x)$  and  $\phi(x,t)$  are the continuous representation of the spin density and the phase dispersion. If we define:

$$k_x(t) \equiv (\gamma / 2\pi) \int_0^t G_x(\tau) d\tau \quad (1-7)$$

Eq. 1-5 becomes:

$$\phi(x,t) = 2\pi x k_x(t) \quad (1-8)$$

The MR signal previously given by Eq. 1-6 can then be rewritten as:

$$S_x(t) = \int_{-\infty}^{\infty} \rho(x) e^{-i2\pi x k_x(t)} dx \quad (1-9)$$

or:

$$S_x(k(t)) = \int_{-\infty}^{\infty} \rho(x) e^{-i2\pi x k_x} dx \quad (1-10)$$

Based on Eq. 1-10,  $S_x(k)$  denotes a  $k$ -space transform of  $\rho(x)$ . It shows that the image  $\rho(x)$  can be reconstructed with a Fourier transform of the receiver signal  $S_x(t)$ , and the receiver signal can be interpreted as a value in the  $k$ -space containing  $S_x(k)$ , which in

MR imaging are sampled along the  $k$ -space trajectory  $k_x(t)$ . Figure 1-1 depicts the practical meaning of the one-dimensional  $k$ -space. Notice that the trajectory depends on  $t$  as a parameter. Based on Eq. 1-7, the amplitude of  $k_x(t)$  represents the  $k$ -space offset, which is proportional to the applied gradient area, and since  $k_x(0)=0$ , the trajectory always starts at the origin. Along the path, the signal can be digitally sampled to provide a set of data points describing the  $S_x(k)$  line.

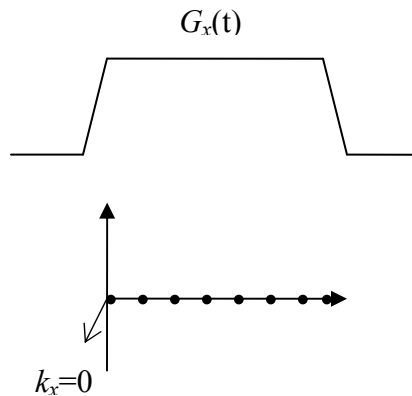


Figure 1-1:  $k$ -space sampling function during a frequency-encoding gradient. The  $k$ -space trajectory starts at the origin. Block dots represents the  $k$ -space sampling data points, which is accomplished during the readout gradient.

Please note that this one-dimensional  $k$ -space is for demonstration. The resultant one dimensional image is actually a spin density image, since  $\rho(x)$  represents the spin density. In reality,  $\rho(x)$  represents signal contrast weighted by different tissue properties, such as T1, T2, or spin density as demonstrated here. In addition, the  $k$ -space is generally two-dimensional or even three-dimensional in clinical practice.

The  $k$ -space can be extended to two dimensions by applying phase-encoding gradients, in addition to frequency-encoding gradients. With similar derivation to the frequency-encoding case, the phase  $\phi$  accumulated after applying a constant phase-encoding gradient from time 0 to time T is:

$$\phi(y,t) = \gamma y \int_0^T G_y(\tau) d\tau = 2\pi k_y y \quad (1-11)$$

A magnetization in the transverse plane can be defined as a complex quantity:

$$M_{\perp} = M_x + iM_y \quad (1-12)$$

The measured MR signal  $S(k_y)$  represented by a one-dimensional  $k$ -space is given by:

$$S(k_y) = \int M_{\perp}(y) e^{-i2\pi y k_y} dy \quad (1-13)$$

or:

$$S(k_y) = \sum_{n=0}^{n=N-1} M_{\perp}(n\Delta y) e^{-i2\pi(n\Delta y)k_y} \quad (1-14)$$

Repeating the phase encoding  $N$  times for  $N$  different values of  $G_y$  produces  $N$  different sets of  $k_y$  values (Figure 1-2). This fills a two-dimensional  $k$ -space and provides sufficient information for a two-dimensional image to be reconstructed.

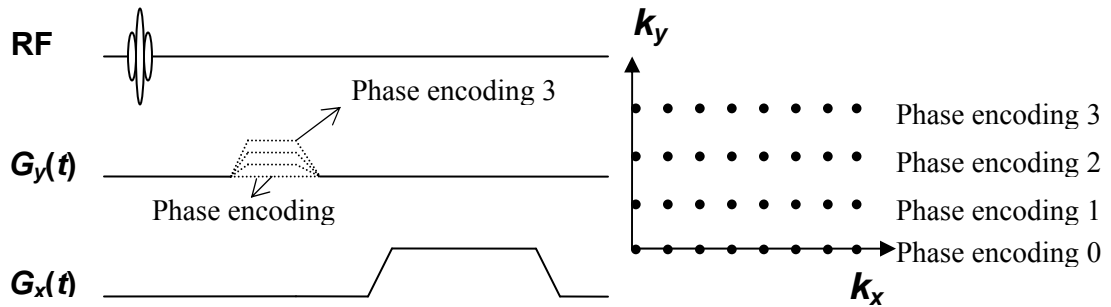


Figure 1-2: A GRE sequence vs. its  $k$ -space path. Each step corresponds to one of the four phase-encoding gradients  $G_y$  (dotted lines). Each phase-encoding step is associated with a separate  $k$ -space line in the two-dimensional  $k$ -space.

The order of sampling in  $k$ -space (i.e., trajectory) is under full experimental control by manipulating the frequency- and phase-encoding gradients. In Figure 1-2, for

example, only the first quadrant is filled in the two-dimensional  $k$ -space ( $k_x$ - $k_y$  plane). By applying a negative gradient pulse in front of the existing frequency-encoding gradient in Figure 1-2 and varying the phase-encoding gradients from a negative value to a positive value in multiple steps, the trajectory could start from the edge of the  $k$ -space, instead of the origin, so that all quadrants of the  $k$ -space data can be obtained.

A variety of  $k$ -space sampling schemes (different trajectories) have been developed and used clinically. Figure 1-3a shows the most common  $k$ -space trajectory, the Cartesian trajectory, where a single  $k$ -space line is acquired at each RF pulse, and data is sampled in Cartesian grid. Figure 1-3b shows the projection acquisition, where the  $k$ -space lines project in the radial direction from the center [59]. The spiral trajectory shown in Figure 1-3c is used for fast MR imaging [60]. The trajectory travels from the center of the  $k$ -space and spirals out. It is often used in cardiac or functional MRI applications. Figure 1-3d shows the echo-planar trajectory, where all  $k$ -space lines are acquired in one or multiple RF excitations [61]. It is much faster than the trajectory shown in Figure 1-3d; however, images obtained using echo-planar trajectory are often subject to artifacts, such as off-resonance effect or Nyquist ghosting [62], and require reconstruction correction.

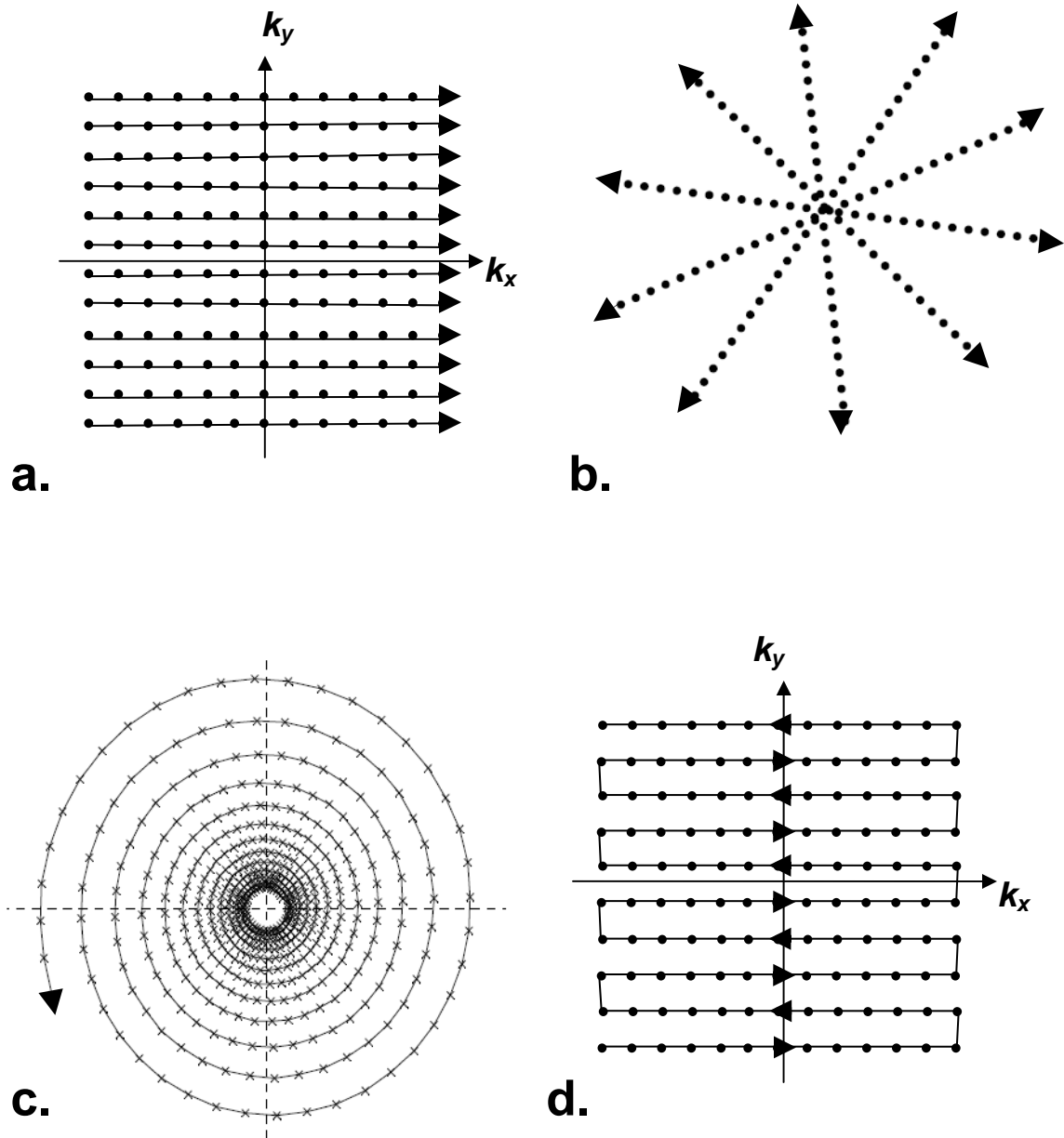


Figure 1-3: A variety of  $k$ -space trajectories. Dots, dashes, or crosses denote the data points sampled during readout gradient. Arrows point to the direction of the  $k$ -space trajectory. a) A Cartesian trajectory where pre-phase gradients move the trajectory to the beginning of each line and then one single  $k$ -space line is sampled after each RF pulse. b) A projection acquisition trajectory where  $k$ -space sampling starts in the radial direction from the center towards the edges. (c) A spiral  $k$ -space trajectory. (d) An echo-planar trajectory. The trajectories in (a) and (b) require excitations equal to the number of lines to fill the  $k$ -space whereas in (c) and (d) all  $k$ -space lines are acquired in one or a few excitations. (Image courtesy of MHA)

### 1.3.4 Pulse sequences

A pulse sequence is a time-series of defined RF and gradient pulses, usually repeated many times during a scan. The time interval between RF pulse and gradients, and the shape and amplitude of these gradients waveforms determine the nature of the MR signal and affect the characteristics of the resultant image.

#### 1.3.4.1 Spin echo sequence

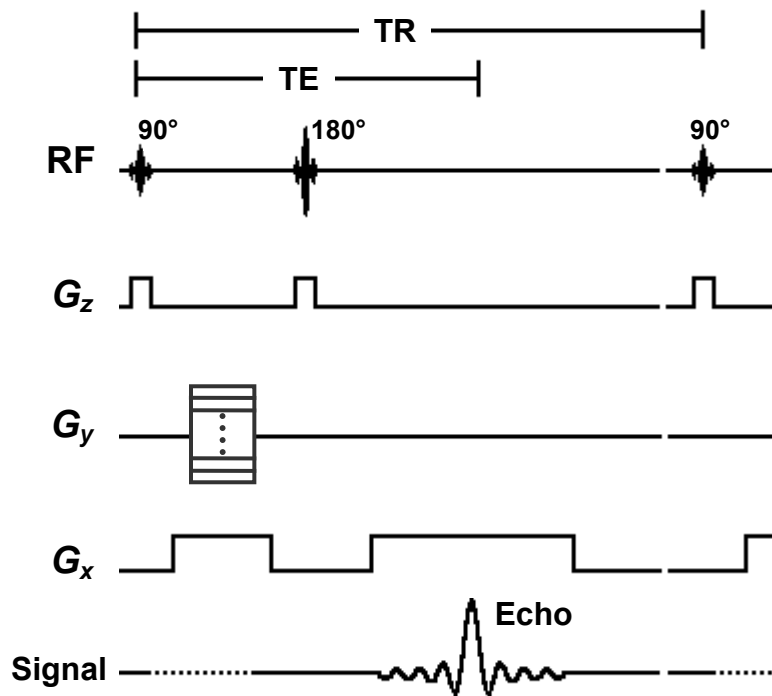


Figure 1-4: The timing diagram of a spin echo sequence. A pulse sequence is composed of a RF pulse and magnetic gradients in three logical directions. TE represents the time between the application of the  $90^\circ$  pulse and the peak of the echo signal, while TR represents the time that exists between successive pulse sequences. In a spin echo sequence, a  $90^\circ$  RF pulse followed by a  $180^\circ$  RF refocusing pulse is employed to produce an echo. This sequence is repeating as many times as the phase-encoding steps. The total imaging time is equal to the product of the TR and the number of the phase-encoding steps.

The spin echo sequence is one of the most commonly used pulse sequence. The timing diagram for a spin echo imaging sequence is shown in Figure 1-4. Please note this diagram has been greatly simplified; amplitude and shape of RF and gradient pulses are not in correct proportion. A sequence timing diagram has entries for the RF pulses and the magnetic gradients in three logical directions. The time interval between two  $90^\circ$  RF pulses is named “repetition time”, or TR, while the interval between  $90^\circ$  pulse (which tips the magnetization vectors into the transverse plane) and the center of the acquired signal (shown as the echo in Figure 1-4) is “echo time”, or TE. A slice selective  $90^\circ$  RF pulse is applied in conjunction with a slice selection gradient. A period of time equal to TE/2 elapses and a  $180^\circ$  slice selective pulse is applied in conjunction with another slice selection gradient. The  $180^\circ$  pulse is used to remove dependence of the signal to spin dephasing due to magnetic field inhomogeneities.

A phase-encoding gradient is applied between the  $90^\circ$  and  $180^\circ$  pulses. The phase-encoding gradient is varied in multiple steps (typically 128 or 256 steps). Its value changes between a positive and a negative value in order to sample  $k$ -space lines from  $-k_y$  to  $+k_y$ . The phase-encoding gradient could be applied after the  $180^\circ$  pulse; however if we want to minimize the TE period, the pulse is applied between the  $90^\circ$  and  $180^\circ$  RF pulse.

The frequency-encoding gradient is applied after the  $180^\circ$  pulse. Such gradient is also known as readout gradient since MR signal is recorded during the time when the gradient is turned on. The collected signal is referred to as the echo. One additional gradient is applied between the  $90^\circ$  and  $180^\circ$  pulses. This gradient is along the same direction as the frequency-encoding gradient. It dephases the spins so that they will

rephase by the center of the echo. Another way of looking at this gradient is that it prepares the signal to be at the edge of  $k$ -space at the start of the acquisition of the  $k$ -space line.

The entire sequence is repeated every TR seconds until all the phase-encoding steps have been recorded. Since in this sequence it takes one TR to record one  $k$ -space line and number of  $k$ -space lines is equal to the number of phase-encoding steps, the total scan time of one image is determined by the product of TR and the number of phase-encoding steps.

#### 1.3.4.2 Gradient echo sequence (GRE)

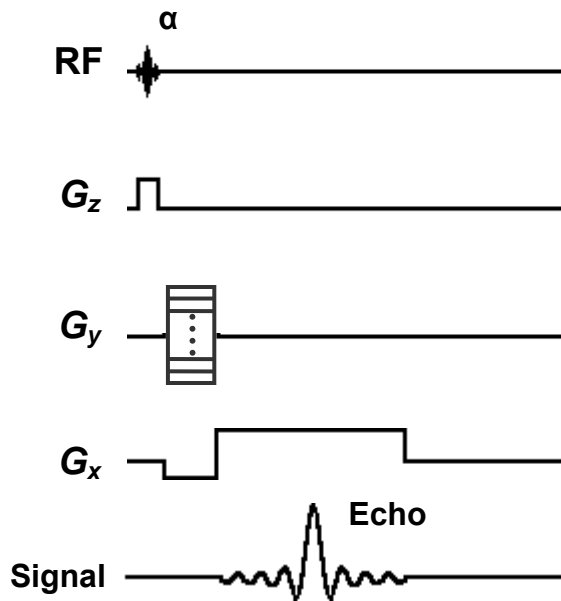


Figure 1-5: The timing diagram of a GRE sequence. A gradient echo is generated by dephasing the spins with a negative gradient before they are sampled with a positive readout gradient.  $\alpha$  denotes the flip angle of the RF pulse in GRE, which is typically between  $10^\circ$  and  $90^\circ$ .

Figure 1-5 shows the timing diagram of the gradient echo sequence. An RF pulse is applied in conjunction with a gradient for slice selection. In GRE, the flip angle of the RF pulse is often set between  $10^\circ$  and  $90^\circ$ . Note that, if the flip angle is less than  $90^\circ$ , then not all the magnetization will be flipped into the transverse plane. While this reduces the overall SNR of the sequence, it enables one to reduce the TR, and the overall scan time of the sequence.

A phase-encoding gradient is applied after the RF pulse. As was the case for the spin echo sequence, the phase-encoding gradient is varied between a positive and a negative value in multiple steps. A prephasing gradient in the readout direction is applied when the phase-encoding gradient is turned on. It prepares the spins so the recorded signal reaches its maximum at the center of the readout period and generates an echo. The prephasing gradient has opposite sign in amplitude and one half of gradient area as opposed to the readout gradient. The echo is formed because the readout gradient refocuses the dephasing which occurred from the prephasing gradient. The reversal of the gradient is responsible for the echo.

A gradient echo sequence is sensitive to variations in the magnetic field. Any magnetic field inhomogeneities that exist within a voxel cause the spins to precess at different frequencies. Between the time of excitation and that for readout (the TE of the sequence) these spins will accumulate different phases, which when summed will result in drop in signal magnitude. The phase of the signal is directly proportional to the strength of the magnetic field at each voxel. As we describe below, this sensitivity of the

gradient echo sequence to the magnetic field enables us to map temperature-induced changes in the proton resonance frequency.

#### *1.3.4.3 Echo planar imaging (EPI)*

Echo planar imaging is a method to accelerate MRI pulse sequences, developed by Mansfield in 1977 [61]. The technique can be used to encode an entire image in a single TR period. Both gradient echo and spin echo sequence can be designed with an EPI acquisition. A timing diagram for the spin echo EPI sequence is shown in Figure 1-6. In contrast to the spin echo and gradient echo sequences described in previous sections, EPI sequences acquire multiple echoes (or  $k$ -space lines) within one TR period.

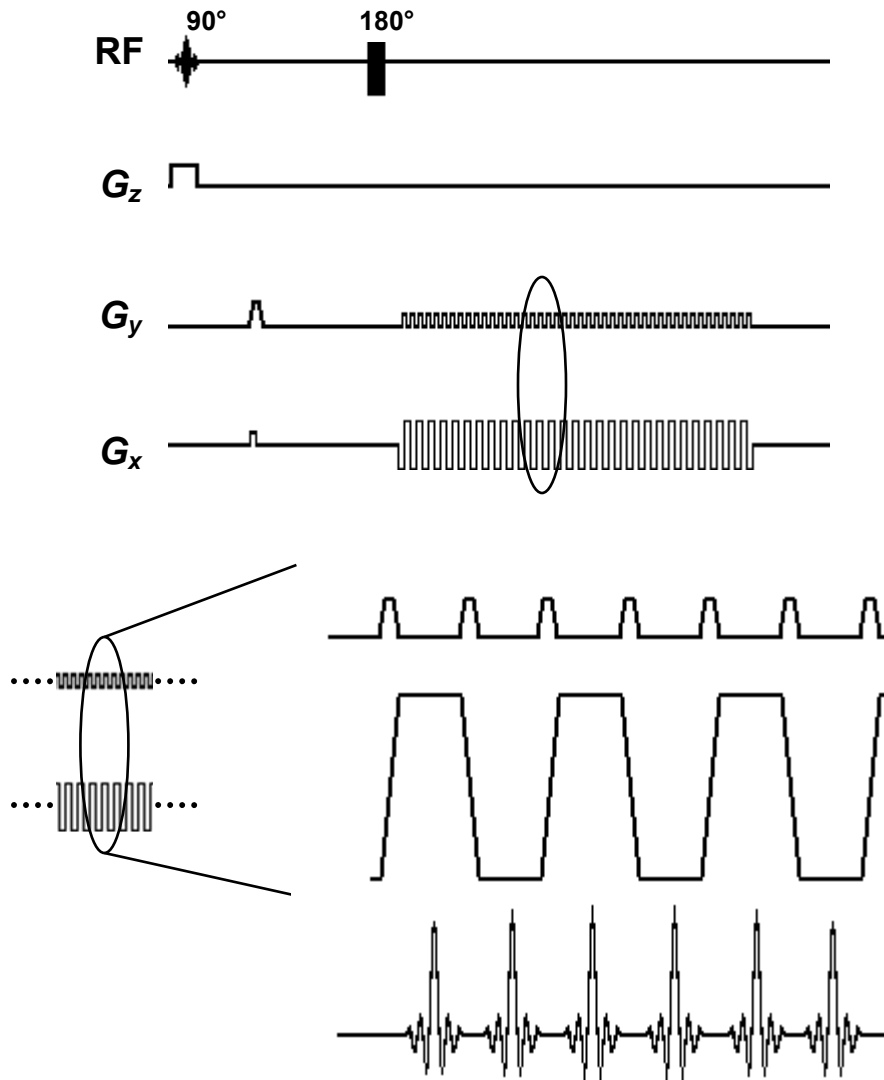


Figure 1-6: The timing diagram of a spin-echo based EPI sequence. A train of frequency- and phase- encoding gradients is used to fill  $k$ -space within one TR. The positive  $y$ -blip gradient moves up the  $k$ -space line one step at a time while the bipolar  $x$  gradient traverses a line in  $k_x$ -space.

An EPI acquisition is implemented with a series of phase- and frequency-encoding gradients applied during the readout period. The positive  $y$ -blip gradient moves sampling of each echo up in  $k$ -space one line at a time while the bipolar  $x$  gradient

traverses the direction of the sampling in  $k$ -space. It is clearer if we zoom into a region of the readout train (Figure 1-6, bottom). It can be seen that during readout a train of phase-encoding gradients, each followed by a bipolar frequency-encoding gradient, is used so that multiple echoes are recorded and the 2D  $k$ -space is sampled. In  $k$ -space, each phase-encoding gradient brings the trajectory up in the  $k_y$  direction, and the following frequency-encoding gradient moves the sampling horizontally along a  $k$ -space line. The polarity of the frequency-encoding gradient determines the direction of the sampling trajectory: it goes from negative to positive  $k_x$  if the gradient is positive in sign and in the opposite direction if the gradient polarity is negative. Overall, the trains of phase- and frequency- encoding gradients trace a zigzag sampling path (as seen in Figure 1-3d). The rate at which  $k$ -space is traversed is so rapid that it is possible, depending on the size of the image matrix, to achieve sub-second resolution.

In the case of a GRE-based EPI sequence, the polarity of the initial frequency- and phase- encoding gradients is reversed and the  $180^\circ$  RF pulse is removed. The data acquisition part of the sequence (i.e., the train of phase- and frequency-encoding gradients) remains the same.

## **1.4 MRI thermometry**

### *1.4.1 Introduction*

Many physical quantities that affect the signals measured in magnetic resonance imaging are temperature-dependent. Accordingly, several MR parameters show temperature dependence. Whether a MR parameter is appropriate for MR temperature measurements depends on multiple factors. The parameter's sensitivity to temperature changes plays an important role, of course, and the linearity of the parameter changes with temperature is also critical. Moreover, it is important that the parameter can be measured independently regardless of other temperature-induced changes in the signal. Plus, the dependence on tissue type and coagulation must be also considered.

The thermal properties of various intrinsic MR parameters have been investigated. Temperature sensitivity of the most MR parameters is reviewed first in section 1.4.2. Later in section 1.4.3, a specific parameter, the proton resonance frequency, is discussed in more detail, since it is employed in the MR thermometry that is most commonly used for clinical applications, and this method is used exclusively throughout this thesis.

### *1.4.2 Temperature sensitive MR parameters*

#### *1.4.2.1 T1 relaxation time*

Reported by Bloembergen et al. [63] in 1948, the longitudinal (i.e., spin-lattice) relaxation time T1 has temperature dependence. T1-based MR temperature measurement was examined in water and ex-vivo blood samples in 1983 [64]. In that study, the possibility of using T1-based thermometry for guidance of hyperthermia was also discussed. A simple model for the T1 temperature dependence was presented:

$$T1 \propto e^{-E_\alpha/kT} \quad (1-15)$$

where  $k$  is Boltzmann's constant,  $E_\alpha$  is the activation energy of the relaxation process, and  $T$  is the absolute temperature. In general, T1 values increase with increasing temperature [64, 65]. However, T1-based thermometry may not be a good candidate for quantitative temperature measurements in thermal therapies. First, the behavior of T1 as a function of temperature changes when thermal coagulation occurs [66]. One study, for example, found that once the temperature in tissue samples exceeded 40 °C, hysteresis occurred [67], making it impossible to relate a particular T1 value to a specific temperature. Furthermore, the temperature dependence of T1 differs significantly between tissues [67], making it challenging to use in practice, particularly when tumors are considered. Note however, that using T1 may be useful in fat. In fat, the signal of a T1-weighted spin echo sequence was found to be linearly dependent on temperature over a wide temperature range [68] and does not have the hysteresis effects with temperature [67].

#### *1.4.2.2 T2 relaxation time*

The transverse (i.e., spin-spin) relaxation time T2 has also shown temperature dependence. An increase in T2 relaxation time with increasing temperature has been observed in aqueous solution [69]. In tissue, however, T2 is reduced by a significant factor compared to pure water and the temperature dependence of T2 can be masked by non-thermal relaxation processes [64]. Furthermore, as in the case with T1, hysteresis occurs, after thermal coagulation. For example, Graham et al. observed hysteresis in the

T2-weighted images in rabbit muscle when the temperature was changed back and forth from 25°C up to 70°C [66].

Although temperature mapping via changes in T2 may not be desirable, T2-weighted imaging is otherwise useful in monitoring thermal therapies because in some cases it enables accurate visualization of irreversible thermally induced tissue changes. For example, in the brain it was shown that T2-weighted images of the thermal lesions correlated best than other sequences with histopathology findings after laser thermal ablation [70].

#### 1.4.2.3 Proton Density

The proton density linearly depends on the equilibrium magnetization of the protons available for excitation. The magnetization is determined by the Boltzmann distribution [71]:

$$PD(T) \propto M_0 = \frac{N\gamma^2\hbar^2 I(I+1)B_0}{3\mu_0 kT} = \chi_0 B_0 \quad (1-16)$$

where PD(T) is the proton density,  $M_0$  is the magnetization,  $N$  is the number of spins per volume,  $\gamma$  is the gyromagnetic ratio,  $\hbar$  is Planck's constant,  $I = 1/2$  is the quantum number of the spin system (i.e., protons),  $B_0$  is the magnetic field,  $\mu_0$  is the permeability,  $k$  is Boltzmann's constant,  $T$  is the absolute temperature of the imaging subject, and  $\chi_0$  is the susceptibility. The relationship of  $\chi_0$  and temperature is given by Curie's law:

$$\chi_0 \propto \frac{1}{T} \quad (1-17)$$

When temperature changes, the ratio of the parallel and anti-parallel spin populations alters and so does the susceptibility  $\chi_0$ . From Eq. 1-17, an increase in temperature causes a decrease in  $\chi_0$ , resulting in a decrease in magnetization, based on Eq. 1-16. Therefore, it is possible to estimate temperature changes with proton-density weighted images. The temperature sensitivity of  $M_0$  is  $0.30 \pm 0.01\%/^{\circ}\text{C}$  between  $37^{\circ}\text{C}$  and  $80^{\circ}\text{C}$  [72]. This sensitivity is small, and proton-density-based thermometry is unpractical because it requires long imaging time to achieve sufficient SNR to get a reasonably low temperature noise.

#### 1.4.2.4 Diffusion-Brownian molecular motion

The temperature dependence of the diffusion coefficient, which describes the thermal Brownian motion of an ensemble of molecules, is given by [73]:

$$D \propto e^{-E_a(D)/kT} \quad (1-18)$$

where  $E_a(D)$  is the activation energy of molecular diffusion of water, which is assumed to be independent of temperature. An increase in temperature gives rise to an increase in diffusion coefficient. The temperature sensitivity can be calculated by taking first derivative of Eq. 1-18 with respect to T, giving rise to a theoretical value of  $2\%/^{\circ}\text{C}$ .

Diffusion-based MR thermometry was first performed by le Bihan in 1989 [74]. Its temperature sensitivity was reported in an in-vivo study, at approximately  $2\%/^{\circ}\text{C}$  [75]. Although the sensitivity is good, the acquisition time is relatively long and the in-vivo implementation suffers from an extremely high sensitivity to motion, due to the nature of diffusion weighted imaging sequence. Moreover, the temperature dependence does not change linearly with temperature when tissue conditions change, such as protein

coagulation. Diffusion-weighted MR thermometry has thus not been widely used for temperature mapping.

### *1.4.3 The temperature sensitivity of the water proton resonance frequency (PRF)*

The proton resonance frequency in water is temperature-sensitive due to temperature dependence of the local magnetic field. The magnetic field seen by the individual protons is different from the constant external magnetic field because of the diamagnetic screening of the electrons and the screening of the surrounding molecules in the sample. The electron screening in water molecules is temperature-dependent, and therefore the PRF can be exploited to monitor temperature changes in MRI.

#### *1.4.3.1 Magnetic field in matter*

The magnetic field in an object can be calculated by Maxwell's equations if the geometry, the orientation with respect to the external magnetic field, and the magnetic susceptibility of the object are given. Suppose there is no current inside the object, the magnetic field strength inside the object can be expressed in terms of a scalar potential:

$$\mathbf{H} = -\nabla\Phi_M \quad (1-19)$$

where  $\mathbf{B} = \mu\mathbf{H}$ .  $\mathbf{B}$  is the magnetic field inside the object and  $\mu$  is the magnetic permeability.

If a sphere of homogeneous material with magnetic susceptibility  $\chi_i$  is placed in a uniform magnetic field  $\mathbf{B}_{\text{ext}} = B_{\text{ext}}\mathbf{z}$ , the scalar potential can be solved explicitly from Gauss' law  $\nabla \cdot \mathbf{B} = 0$ :

$$\Phi_M = \frac{-3(1 + \chi_e)H_0 r \cos \theta}{(3 + \chi_i + 2\chi_e)} \quad (1-20)$$

Where  $\chi_e$  is the susceptibility of the material enclosing the object, and  $H_0 = B_{ext}/\mu_i$ , where  $\mu_i$  is the magnetic permeability of the object. Substituting Eq. 1-20 into Eq. 1-19, we can obtain the macroscopic field inside the object:

$$\mathbf{B}_{mac} = \frac{-3(1 + \chi_e)\mu_0 H_0 r \cos \theta}{(3 + \chi_i + 2\chi_e)} \hat{z} \cong (1 - \frac{2}{3}(\chi_e - \chi_i))B_{ext} \hat{z} \quad (1-21)$$

where the second part is limited to terms of first order of  $\chi_e$  and  $\chi_i$ . The derivation of Eq. 1-21 can be found in standard textbooks on electrodynamics [76].

The proton resonance frequency of a nucleus in a water molecule is determined by the local magnetic field,  $\mathbf{B}_{nuc}$ , it experiences. To express  $\mathbf{B}_{nuc}$ , a screening constant  $\sigma$  is defined to express the screening effect of the molecules. From Eq. 1-21 and the principle of superposition,  $\mathbf{B}_{nuc}$  can be written as:

$$\mathbf{B}_{nuc} \cong (1 - \frac{2}{3}\chi_i - \sigma) \mathbf{B}_{mac} \quad (1-22)$$

#### 1.4.3.2 Temperature dependence of the local magnetic field

The susceptibility  $\chi_i$  [77] and the screening constant  $\sigma$  [78] depends on the temperature distribution  $T(\mathbf{r})$ . For an object with a certain susceptibility distribution  $\chi_i(\mathbf{r}, T(\mathbf{r}))$  and a certain electron screening constant  $\sigma(\mathbf{r}, T(\mathbf{r}))$  which is placed in a uniform external magnetic field, the local magnetic field  $\mathbf{B}_{nuc}$  is:

$$\mathbf{B}_{nuc}(\mathbf{r}, T(\mathbf{r})) \cong (1 - \frac{2}{3}\chi_i(\mathbf{r}, T(\mathbf{r})) - \sigma(\mathbf{r}, T(\mathbf{r}))) \mathbf{B}_{mac}(\chi_i(\mathbf{r}, T(\mathbf{r}))) \quad (1-23)$$

The macroscopic magnetic field can be approximated, when  $\chi_i \ll 1$  such as in human tissue, by  $\mathbf{B}_{\text{mac}} \sim \mathbf{B}_{\text{ext}} + O(\chi_i \mathbf{B}_{\text{ext}})$ , where  $O(\chi_i \mathbf{B}_{\text{ext}})$  are terms of the higher order of  $\chi_i$  [79]. Such approximation leads to:

$$\mathbf{B}_{\text{nuc}}(\mathbf{r}, T(\mathbf{r})) \sim \mathbf{B}_{\text{mac}}(\chi_i(\mathbf{r}, T(\mathbf{r}))) - (2/3 \chi_i(\mathbf{r}, T(\mathbf{r})) + \sigma(\mathbf{r}, T(\mathbf{r}))) B_{\text{ext}} \mathbf{z} \quad (1-24)$$

In water, the protons are screened from the macroscopic field,  $\mathbf{B}_{\text{mac}}$ , by the electrons in the hydrogen atoms. A proton in a hydrogen atom is screened more efficiently by the electron cloud than the proton in a water molecule, which is hydrogen bonded to another molecule. This is because the hydrogen bonds between neighboring molecules distort the electronic configuration, and reduce the screening. As temperature increases, the hydrogen bonds bend, stretch, and break, i.e., on average the water molecules spend less time in a hydrogen-bonded state [78]. Accordingly, the electron screening is enhanced with increased temperature, resulting in a lower local magnetic field, and a lower PRF.

The electron-screening constant of pure water varies approximately linearly with temperature over a wide range of interest to thermal therapies such as FUS, from  $-15^\circ\text{C}$  to  $100^\circ\text{C}$  [78]. Reported by Hindman in 1966, the temperature dependence of PRF in pure water is  $-0.0108 \pm 0.0001 \text{ ppm}/^\circ\text{C}$  [78]. It has been shown that the temperature dependence of the water PRF in ex-vivo tissue samples has nearly the same value as the pure water, is tissue-type independent, and is not affected even when tissue had been coagulated [80]. In an in-vivo study where rabbit thigh was heated with FUS, the temperature dependence also exhibited nearly no dependence of thermal history [81]. However, this tissue type independence is only true for aqueous tissues. In fat, where

hydrogen bonds are not present, the screening constant appear only a small dependence on temperature [4].

The magnetic susceptibility is also temperature dependent. It can be approximated as linear over the temperature range of interest. The susceptibility change with temperature in pure water is 0.003 ppm/°C [77] and 0.0016 ppm/°C [82] for muscle tissue from 30°C to 45°C. It is also known that the susceptibility is tissue-type dependent [82]. Note the temperature dependence of the susceptibility in pure water and muscle tissue is much smaller than that of the screening constant, and therefore the changes in local magnetic field due to the changes in susceptibility are ignored in most implementation of PRF thermometry in aqueous tissue.  $\mathbf{B}_{\text{mac}}$  itself in Eq. 1-24 also depends on temperature, since it is a function of the susceptibility, which is temperature dependent. Changes in susceptibility alter the macro magnetic field, which affects the PRF, and therefore the temperature measurements. Neglecting the temperature-induced susceptibility changes leads to temperature error in PRF-based thermometry [83].

#### *1.4.3.3 Temperature mapping using PRF shift*

There are two ways to measure PRF shift (and therefore temperature change): One is to measure the change in frequency from spectroscopic imaging [2], another is to measure the change in phase from phase mapping [84]. In spectroscopic thermometry, the frequency shifts are calculated from MR spectra by measuring the shifts in water peak. It makes absolute temperature measurement possible if there is a reference peak that does not change with temperature, such as fat [4]. However, spectroscopic imaging sequences usually suffer from low spatial and temporal resolution. Advanced technique, such as

echo planar spectroscopic imaging [85] and line scan echo planar spectroscopic imaging [86] has been proposed to significantly speed up for spectroscopic MR thermometry, but the spatial resolution is still low.

In phase-mapping thermometry, PRF shifts are rapidly estimated from the phase maps generated during standard gradient echo images. This method allows temperature measurements at sub-second with high spatial resolution [8-10]. Echo shifted gradient echo images [10, 87], which uses acquisitions with  $TE > TR$ , has also been used to improve the temperature sensitivity (which change linearly with TE) while using a short TR interval. To remove the contribution from the static magnetic field and field inhomogeneities, a baseline image is required before heating so it can be subtracted from the images after heating. The subtraction increases the temperature error by  $\sqrt{2}$  and makes the phase-mapping method vulnerable to motion and field drifts. Only temperature changes can be imaged when phase-difference imaging is used.

The temperature changes can be estimated quantitatively from the phase difference between two time frames of MR images. From Eq. 1-24, the phase difference  $\Delta\phi$  between the baseline MR image and the MR image after heating, acquired at temperature  $T_{ref}$  and  $T$ , respectively, is:

$$\begin{aligned}
 \phi - \phi_{ref} &= \gamma TE (B_{nuc}(r, T(r)) - B_{nuc}(r, T_{ref}(r))) \\
 &= \gamma TE (\Delta B_{mac} - \Delta\sigma B_{ext} - 2/3 \Delta\chi_i B_{ext})
 \end{aligned} \tag{1-25}$$

where  $\gamma$  is the gyromagnetic ratio of the proton, TE is the echo time, and  $\Delta\sigma$  and  $\Delta\chi_i$  are the temperature-induced changes in the electron screening constant and magnetic

susceptibility, respectively. Neglecting any temperature dependence of the magnetic susceptibility, the temperature change,  $\Delta T$ , can be computed from the phase difference,  $\Delta\phi$ , using the following equation:

$$\Delta T \cong \frac{\Delta f}{B_{ext} \gamma \alpha(T)} = \frac{\Delta\phi}{2\pi TE \cdot B_{ext} \gamma \alpha(T)} \quad (1-26)$$

where the  $\alpha(T)$  is the proportional constant, called thermal coefficient, with  $\alpha(T) = d\sigma / dT = -0.01 \text{ ppm}/^\circ\text{C}$ . The procedure for using the temperature-dependent PRF shift for MR thermometry is to acquire one or more images before the heating, and to calculate the phase changes with respect to this baseline image, and then to compute the temperature changes from Eq. 1-26.

#### 1.4.3.4 Source of error

The presence of fat corrupts the temperature measurements using PRF shift. It poses an important problem for the method since many biological tissues contain both water and fat. As described in previous section, the PRF of fat is almost completely independent of temperature. The MR signal is the vector sum of two different chemical species: one changes with temperature, another does not. The phase of the vector sum, therefore, does not change linearly with temperature and measurements using Eq. 1-26 leads to errors. To overcome this problem, fat suppression techniques should be used in tissues, such as breast, where there is significant lipid content [4, 10]. The effect of lipids in thermometry is discussed in more detail in Appendix A.

Any magnetic field changes unrelated to changes in the electron screening constant of water are sources of error, such as the temperature-induced magnetic

susceptibility changes or electric conductivity [88] changes. The susceptibility changes are typically ignored in aqueous tissues (as described above) and the effect from electric conductivity is expected to be small for small heat source, such as produced by a FUS beam. While these errors are typically ignored, one must be aware that they are present and introduce some uncertainty in the measurements.

Due to the image subtractions in the phase-mapping method, temperature errors would also occur when there is motion, blood flow, and/or external magnetic field drifts in the imaging subject. Any motion of the imaging subject will alter the magnetic field distribution and introduce PRF shifts that are not induced by temperature, and therefore cause temperature error when two unregistered phase images are subtracted. A number of approaches have been proposed to reduce the effects of motion. First, one can acquire multiple baseline images to capture the entire motion trajectory, such as which may occur during respiration [89]. Navigator echoes have also been proposed to correct the motion artifact for translational motion [11]. One can also produce simulated baseline images by using the surrounding (non-heated) tissue [90]. In this technique, commonly referred to as “referenceless thermometry”, one fits the phase distribution (excluding the heated zone) to a surface. This surface is then extrapolated into the heated region, creating an artificial baseline that is subtracted off. Finally, all of these techniques can be combined together [91]. Utilizing these correction schemes have enabled possibility of using MR temperature imaging in moving organs such as the liver or even the heart.

When moving organs are considered, one needs to have a rapid imaging sequence. Acceleration of image acquisition could reduce the artifacts induced by intrascan motion

(movement of an object during the scan). Motion outside the imaging FOV, such as breathing and cardiac motion, may also affect the magnetic field in the imaging region. Drift in the external magnetic field is very likely to happen during long heating sessions. It can be corrected by subtracting any magnetic field changes that occur outside the heating zone, either with external phantoms [82] or at locations in tissue where it is known that there are no temperature changes. Most of the errors caused by subtraction of two unregistered images can be reduced by measuring PRF shifts spectroscopically. Using chemical specie that is temperature-insensitive as an internal reference, we can measure the water peak shifts without subtraction from baseline image, and therefore avoid such temperature errors.

In spite of these sources of error, the PRF-based method is the most promising for MR thermometry. It offers the highest precision among endogenous MR parameters to measure small temperature changes [92], it is independent of tissue type and thermal history, and it fits well with a variety of advanced imaging sequences for rapid measurements. It is now used clinically for both FUS and laser thermal ablation.

## 1.5 Scope of this dissertation

Prior research and clinical studies have demonstrated that focused ultrasound thermal treatments can be significantly enhanced through MR image guidance. With high spatial resolution, excellent tissue contrast and temperature sensitivity, MRI has offers the possibility to precisely monitor almost all aspects of a thermal therapy procedure. The temporal resolution of MRI, however, has constrained the therapy from being applied to some organs, such as the heart. The purpose of this thesis was to investigate the temporal aspect of MRI, and particularly quantitative MR thermometry, for use in guiding focused ultrasound thermal therapy.

In the first project of the thesis, a hybrid imaging technique which fused three existing fast imaging methods was investigated as to its ability to accelerate the MR thermometry method compared to that used clinically in FUS thermal therapy. In the first set of experiments, the hybrid methodology was tested in a doped water phantom and implemented for making temperature measurements during FUS heating experiments both in vitro and ex vivo. The limit of the hybrid technique in terms of the obtainable acceleration factor was determined. With the maximum acceleration, this hybrid accelerated thermometry method was compared with a non-accelerated standard clinical thermometry method in a series of FUS experiments. Statistical comparison between the new sequence and the standard one confirmed that measurements made with this new accelerated technique is equivalent to the gold-standard thermometry, but with a higher temporal resolution. In the second set of experiments, this technique was modified to give a 3D imaging sequence and applied for 3D temperature monitoring in FUS heating

experiments. The ability of this technique to perform in 3D gives a framework, with which we can reshape a 2D imaging plane into a rectangular 3D slab (e.g., reduce the size in phase-encoding direction and increase the size in slice direction), depending upon the shape of an ROI, while achieving high temporal/spatial resolutions and maintaining acceptable temperature resolution. We expect this imaging to be useful in cases such as prostate ablation, where the heating distribution needs to be measured in 3D with high spatial resolution, but where motion is not an issue. In the third set of experiments, three systems were successfully integrated for real-time scanning, image reconstruction, and display, and performed with the hybrid technique in a FUS heating experiment. These experiments demonstrated the capability of the accelerated MR thermometry for real-time temperature monitoring in a 3D volume.

The acceleration of the hybrid technique depends upon the size of the 2D plane being reduced along phase-encoding direction. The smaller the size, the faster the acquisition. In the extreme case a 2D plane can be reduced to a 1D column. This was investigated in the second project. A previously developed novel linescan spectroscopic imaging sequence which excited a single line was evaluated for use in ultrafast 1D MR thermometry. With this linescan technique, one is able to acquire multiple echoes (without phase-encoding) within one TR. In the first set of experiments, FUS heating experiments were performed in a tissue-mimicking phantom. In calibration experiments, temperature measurements obtained from each echo were calibrated with measurements obtained from the gold-standard thermometry sequence. This study confirmed that the 1D approach was able to acquire multiple measurements accurately at the temporal

resolution of one TR. The limit of the temporal resolution was then tested in rapid heating experiments. The conditions whereby the temporal resolution equal to the time between echoes could be achieved were examined. In a second set of experiments, in-vivo experiments were performed without heating. In these rabbit brain experiments, the temperature noise for each echo was estimated. These results are valuable for establishing a protocol for measuring brain tissue heating. Finally, in an experiment with a volunteer, we tested whether we could spectroscopically measure the water frequency in the beating heart in order to demonstrate the possibility of monitoring temperature changes in a very mobile organ.

In the final part of this thesis, we addressed two important issues that came to light in pursuing the work of the second project: 1) Could the hybrid method be made robust with respect to the cancellation of the contributions from fat? 2) Could the hybrid method be incorporated into a fast imaging sequence such as EPI to further accelerate MR thermometry? First, the 2DRF excitation pulse, one of the three fast imaging components combined in the hybrid method, was modified and tested to ensure that the lipid signals were fully suppressed. Armed with this specific 2DRF pulse, the hybrid method was applied in a cheese phantom heating experiment to test its ability to give accurate temperature measurements. Second, the hybrid method was incorporated into a 3D EPI sequence. We are interested in mapping temperature changes during FUS ablation in the brain using transcranial sonications. In that application, we need to monitor both the heating at the focal point, and that resulting from skull heating. The resulting sequence was tested in FUS heating experiments of a tissue-mimicking phantom

and in an ex-vivo human skull. This EPI-based hybrid method was shown to be capable of rapidly quantifying temperature changes in 3D.

## 2 Experimental methods

### 2.1 Ultrasound

The ultrasound fields were generated by spherically curved, piezoelectric transducers. For some experiments, a single-element transducer was used with a diameter of 10 cm, radius of curvature of 10 cm, and resonance frequency of 1.5 MHz. For others, phased array transducers were used with diameter of 10 cm, radius of curvature of 8 cm, and resonance frequency of 1.1/1.6 MHz. When the single crystal transducer was used, the transducer was driven by a function generator (Model 396, Fluke, Everett, WA) and RF amplifier (model 240L, E and I, Rochester, NY). During the sonications, the RF power (forward and reflected) was monitored using a power meter (model 438A, Hewlett Packard, Palo Alto, CA) and dual directional coupler (model C1373, Werlatone, Brewster, NY). The electrical impedance of the transducer was matched to the output impedance of the amplifier by means of an inductor-capacitor circuit contained within an external matching box. The function generator, amplifier, power meter, and matching circuit were part of the MR-compatible FUS system described later in Section 2.2.

The full-width, half-maximum beam length and width of the focal region produced by these transducers were provided in the later sections when they were used for different experiments. Acoustic power levels used in this work were selected to produce a desired temperature rise for each particular experiment. Based on prior experience, these exposure levels were below the threshold for inertial cavitation.

In many scenarios, increasing the size of focal zone is desired to accelerate FUS treatments [24-27]. This increase is achieved by either producing multiple focal regions

simultaneously [24] or by steering the focal region to different points during the sonication [27]. In these cases, it may be possible to achieve sufficient monitoring of the heated region with a lower spatial resolution in the temperature imaging. In experiments that tested imaging with relatively low spatial resolution, we used a phased array transducer to increase the focal volume. This was necessary to avoid so-called “partial volume” or “voxel averaging” effects that lead to a temperature underestimate when the size of focal heating is smaller than the MR imaging voxel size [6].

We used a relatively simple “sector vortex” phased array transducer [24], which consists of a transducer cut into a small number of pie-shaped elements [93]. Figure 2-1 shows an eight-element sector-vortex transducer with a 10-cm diameter and an 8-cm radius of curvature that was used in some of the experiments. The multi-element transducer can operate at different “modes”, e.g. mode  $m$ . The number  $m$  ranges from 0 to  $N/2$ , where  $N$  is the number of elements in the transducer. The phase of the  $i^{\text{th}}$  element is given by:

$$\theta_i = m \times i \times 2\pi / N \quad (2-1)$$

When  $m = 0$ , phase of all elements is the same, meaning all elements sonicate at the same time. This mode produces a field identical to a single-element transducer. At higher modes, this transducer creates a focal pattern consisting of peaks arranged in a ring. The size of the ring depends on the mode number. After sonicating for a few seconds, the temperature at the center of the ring and the space between the discrete peaks are filled in by thermal conduction, producing a relatively uniform temperature distribution and therefore reduces the effects of voxel averaging. Figure 2-2 shows the

ultrasound beam plots of different mode numbers for an eight-element sector-vortex transducer at 1.1 MHz. A different phased array transducer with sixteen elements was used for some experiments (diameter: 10 cm, radius of curvature: 8 cm, resonance frequency: 1.6 MHz). Both array transducers were driven by a custom-build multi-channel amplifier system with power control and phase control for each element [94].

Another phased array transducer with sixteen elements was used for some experiments (diameter: 10 cm, radius of curvature: 8 cm, resonance frequency: 1.6 MHz). Both array transducers were driven by a custom-build multi-channel amplifier system with power control and phase control for each element [94].

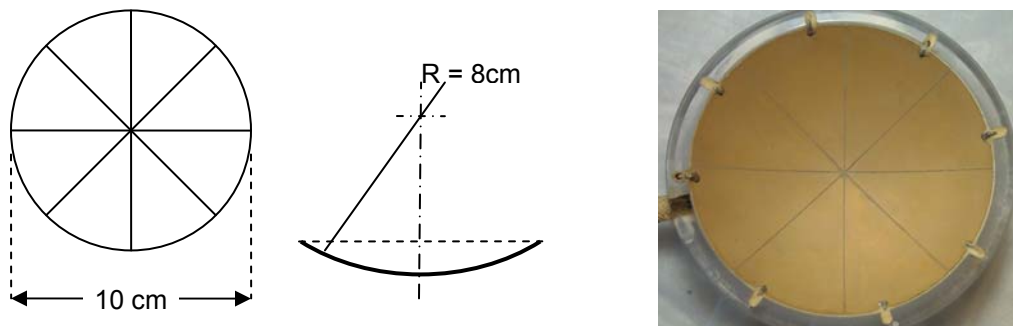


Figure 2-1: An eight-element sector-vortex array transducer. The power and phase of each element of the transducer was controlled separately by a multi-channel amplifier system.

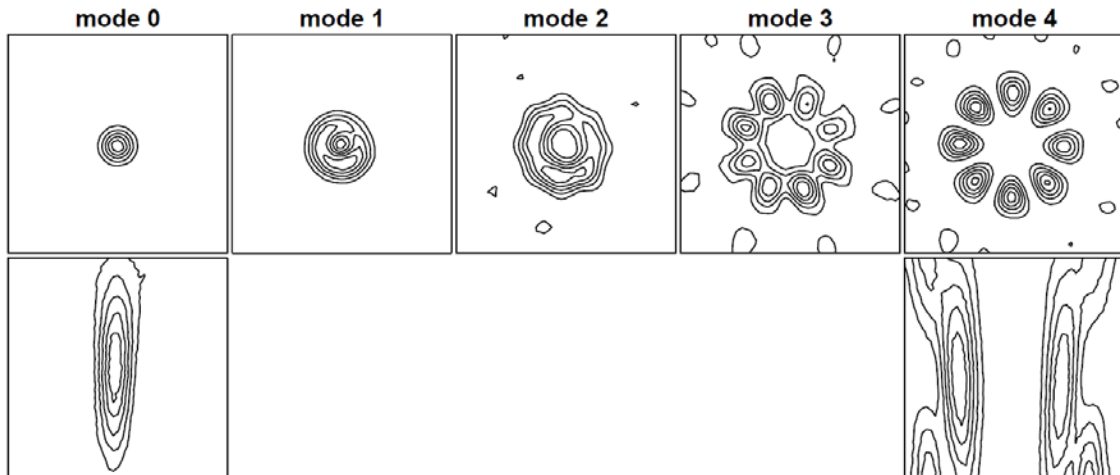


Figure 2-2: Ultrasound beam plots of a sector vortex (1.1 MHz) transducer in modes 0-4. The plots were created by scanning a needle hydrophone (diameter = 0.075 mm, Precision Acoustic, Dorset, England) in a raster pattern perpendicular (top) and parallel (bottom) to the direction of the ultrasound beam. In modes 1-4 the ultrasound intensity is zero along the axis of the ultrasound beam because of the phase symmetry. A relatively uniform spatial temperature profile was created in tissue over time due to thermal conduction. (Image courtesy of Nathan J. McDannold.)

## 2.2 MRI

The experiments were performed on either a 1.5-T or 3-T GE Signa clinical MRI systems (General Electric Healthcare, Milwaukee, WI). The 1.5-T MRI equips with echo-speed gradients (maximum gradient strength of 33 mT/m, maximum slew rate of 120 T/m/s) while the 3-T MRI equips with twin-speed gradients (maximum gradient strength 40 of mT/m, maximum slew rate of 150 T/m/s). Images were acquired using either a surface coil (7.6-cm diameter, GE Healthcare), an eight-channel head coil (GE Healthcare), or an eight-channel cardiac coil. The research MRI pulse sequences were written in the EPIC programming language. The linescan sequence used in Section 4.2.1 was provided by Dr. Koichi Oshio from Keio University, Japan.

## 2.3 Experimental set-up

### 2.3.1 MR-compatible FUS positioning system

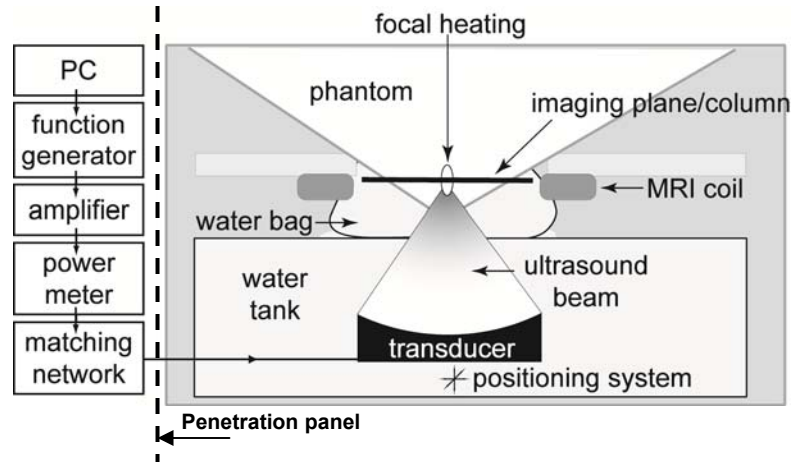


Figure 2-3: Scheme for the MR-compatible FUS positioning system. *Left:* The ultrasound driving equipment was outside the magnet room *Right:* The transducer was immersed in a bath of degassed, deionized water and mounted in a three-axis manual positioning system. The phantom was fixed in place on a tray above the water tank. A thin, plastic bag filled with degassed water ensured an acoustic beam path into the phantom. A receive-only MRI surface coil (7.6-cm diameter, GE Healthcare) was placed around the phantom approximately at the level of the focus. In the rapid heating experiments in this dissertation, the imaging plane/column passed the focus and was placed perpendicular to the direction of the ultrasound beam.

Figure 2-3 shows a diagram of the set-up used in experiments where the transducer was mounted in an MR-compatible FUS positioning system. The transducer was mounted in a custom-made holder that was coupled to three-axis positioning system that was constructed of aluminum and brass (Velmex, Bloomfield, NY) and was mounted at the end of the patient MRI table. The transducer holder and positioning system were connected together via an aluminum bar. This arrangement allows one to manually control the position of the transducer in three translational degrees of freedom while the transducer and sample were at the isocenter of the MRI. The transducer was submerged in a tank of degassed, deionized water. The target (gel, tissue sample etc.) was placed in a

hole in a plastic tray positioned above the transducer. The hole was the opening of a bag of degassed water. The water bag rested on a PVC membrane above the transducer. A layer of degassed water was poured between the membrane and the plastic bag to provide proper ultrasound coupling. A surface coil was attached beneath the plastic tray below the target to receive MR signal. The positioning system was build into a cradle that fit the scanner bore. Outside the magnet room, a personal computer network controlled the transducer's power, frequency, pulsing duration, and duty cycle. The cables to the driving system passed through the filters in the penetration panel of the MRI room.

### 2.3.2 MR-compatible FUS set-up for use in MRI array receivers

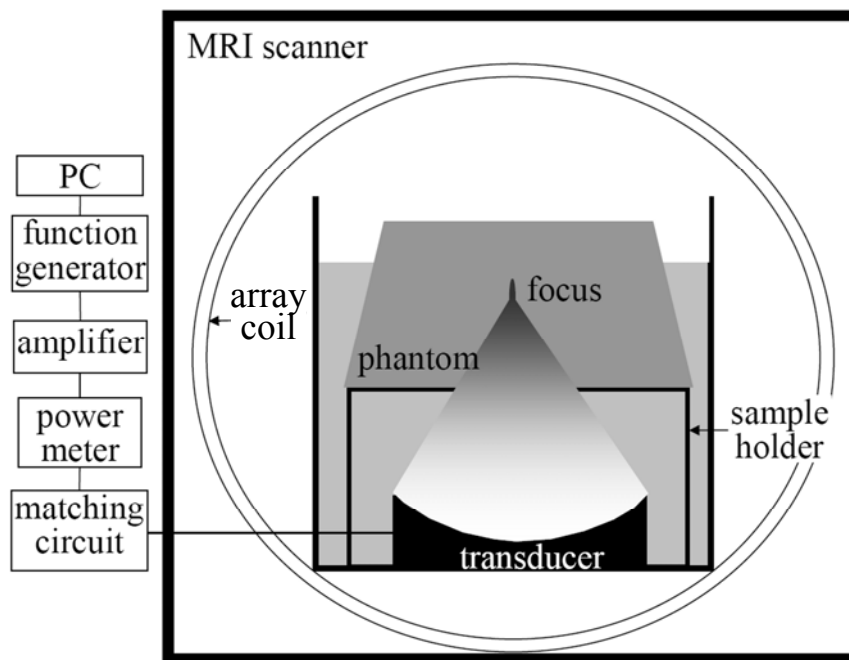


Figure 2-4: Axial view of the FUS set-up within MRI bore. when the MRI phased array coil was used. The transducer was immersed in a bath of degassed, de-ionized water. The phantom was placed on top of the holder in an eight-channel head array (GE, Milwaukee, WI). The focused ultrasound beam propagated through the water and phantom and focused on a spot just below the water level. Temperature mapping images were acquired in the transverse plane of the beam containing the focus.

For some of the sequences tested, multiple MRI receive channels (more details in section 2.4.3) were utilized and a phased array MR receiver coil was required. The array coil used throughout the dissertation was not compatible with the FUS positioning system described in previous section, so a customized MR-compatible FUS system was constructed in house. The system is shown in Figure 2-4. An acrylic tank was built to fit into a standard GE eight-channel head coil. The transducer was mounted on the bottom of the acrylic tank, which was filled with degassed, deionized water. Tissue samples or phantoms were placed on a plastic holder above the transducer. The height of the holder could be adjusted so that the ultrasound beam could focus inside the phantoms at different depths.

In contrast to the design of the positioning system described in the previous section where transducer could move in three degrees of freedom, the transducer in the FUS system for use with MRI phased array coil was fixed at the bottom of the water tank. When sonicating at different locations was necessary, the target sample was repositioned. While this was not a particularly precise procedure, it was sufficient for these experiments. When a single target was sonicated multiple times, the time between each sonication was long enough (generally a few minutes) for temperature in the focal region to return to its baseline value.

## 2.4 Advanced MRI techniques

### 2.4.1 Volume-selective two-dimensional RF (2DRF) excitation

Normally, a slice-selective RF excitation pulse is combined with a linear gradient to excite all of the spins within a slab, and everything within the sensitive region of the MRI coil will contribute to the acquired image. Unless small coils are used, the areas that contribute to the image acquisition can be larger than the region of interest, which in the case temperature imaging, is constrained to the heated region (and in the case of FUS, perhaps the ultrasound beam path). To avoid aliasing, a large field of view is necessary, resulting in either a low spatial resolution or the need to perform additional acquisitions. One way to constrain the RF excitation profile to only a limited region of interest is to use volume-selective RF excitation [18].

A volume-selective RF excitation performs a spatial selection along the slice direction in addition to selecting a limited region in the frequency- and/or phase-encoding directions. In this dissertation, a two-dimensional volume-selective RF (2DRF) pulse was employed, where spatial selection was performed along the slice and phase-encoding directions. The method used is similar to that described previously. It is done by a series of RF pulses modulated with either a Gaussian or a sinc envelop along with magnetic gradients in both slice- and the phase-encoding directions.

An example of a 2DRF pulse is show in Figure 2-5. A small-tip-angle model was used for the 2DRF pulse design [19]. By applying the RF field  $B_1(t)$ , which is composed of a series of subpulses weighted with the  $k$ -space weighting function  $W(\vec{k})$ , the

excitation profile  $M(\vec{r})$  produced in conjunction with a magnetic field gradient  $\vec{G}(t)$  can be expressed as:

$$M(\vec{r}) = i\gamma M_0 \int W(\vec{k}) S(\vec{k}) \exp(i\vec{r} \cdot \vec{k}) d\vec{k} \quad (2-2)$$

where  $\gamma$  and  $M_0$  represent the gyromagnetic ratio and the original longitudinal magnetization, respectively.  $S(\vec{k})$  is the sampling function in excitation  $k$ -space, and  $\vec{k}(t) = -\gamma \int_t^T \vec{G}(\tau) d\tau$ . The weighting function  $W(\vec{k})$  is defined as the ratio of the RF field  $B_1(t)$  to the product of the gyromagnetic ratio  $\gamma$  and gradient field  $\vec{G}(t)$ :

$$W(\vec{k}(t)) = \frac{B_1(t)}{\gamma |\vec{G}(t)|}. \quad (2-3)$$

From Eq. 2-2, the excitation profile  $M(\vec{r})$  can be viewed as the Fourier transform of the product of  $k$ -space weighting function  $W(\vec{k})$  and  $k$ -space sampling function  $S(\vec{k})$ , which is a weighted trajectory in excitation  $k$ -space. As shown in Figure 2-5a, a Cartesian trajectory was used in excitation  $k$ -space for 2DRF excitation pulses. The corresponding gradient waveforms and spatially selective RF pulse are shown in Figure 2-5b. The slice ( $G_z$ ) and phase ( $G_y$ ) gradients are employed to produce the sampling function  $S(\vec{k})$ , and the RF pulse envelope produces the spatial frequency weighting function  $W(\vec{k})$ . For the pulse shown in Figure 2-5b, each subpulse has a Gaussian-shaped envelope. To reduce the overall pulse duration, the subpulses are played out during both the plateaus and ramp sections of the  $G_z$  waveform, and during both the positive and negative parts of the waveform. The excitation profile produced by such RF pulses is shown in Figure 3-2.

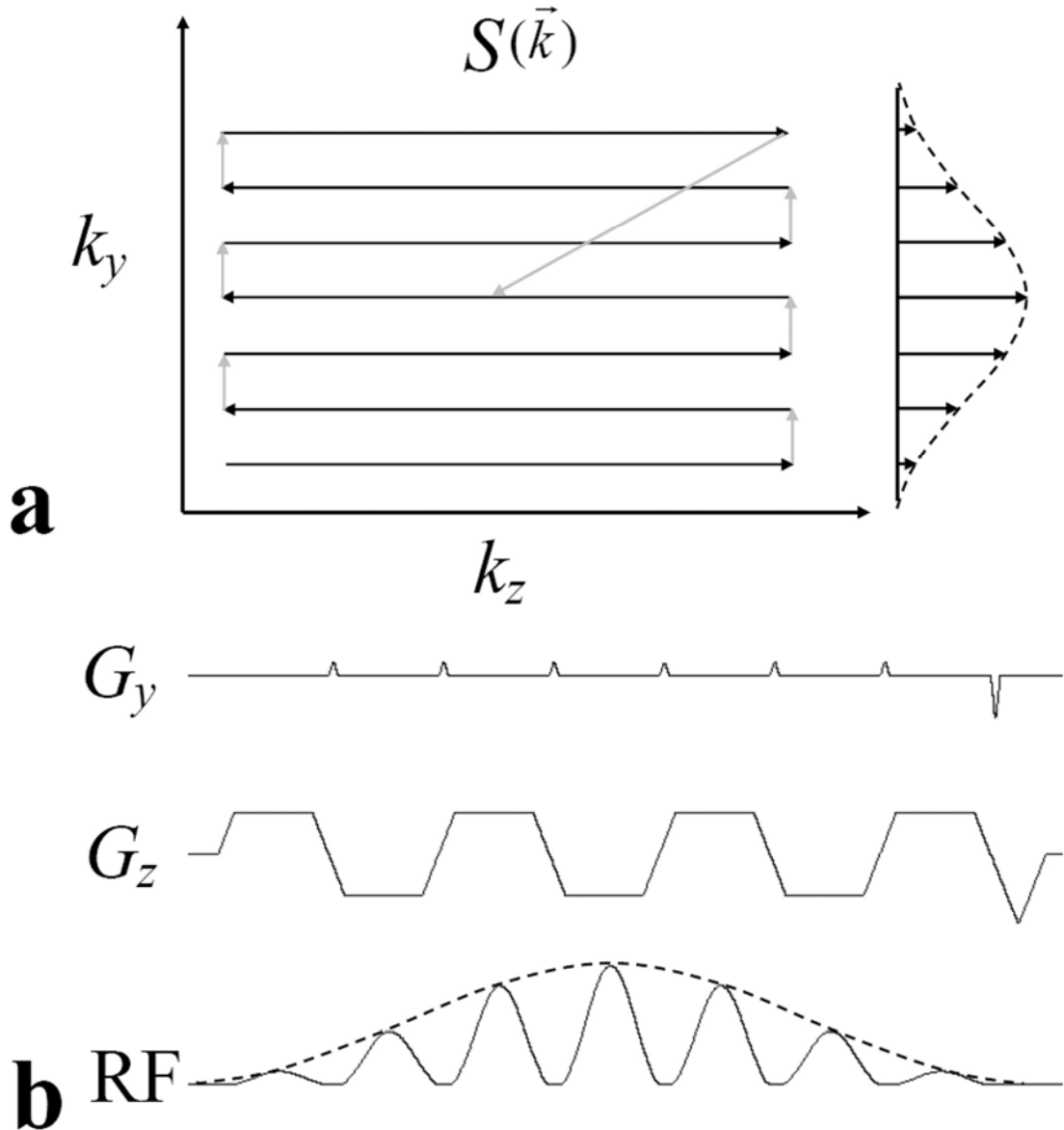


Figure 2-5: The 2DRF pulse vs. its excitation  $k$ -space trajectory. a) The Gaussian-modulated, Cartesian excitation  $k$ -space trajectory of 2DRF pulse that was used in these experiments. The modulation envelope, the distance between lines ( $\Delta k_y$ ), the number of  $k_y$  lines, and the phase values of each line are user-defined parameters. b) The gradient waveforms and RF pulse waveforms for excitation  $k$ -space trajectory shown in a. The area of the phase blip gradient ( $G_y$ ) is used to control  $\Delta k_y$ , and is determined by the distance between lines along the  $k_y$  direction. Rephasing gradients at the end of the  $G_y$  and  $G_z$  rewinds the sampling trajectory to the center of  $k$ -space. Subpulses are played out during both positive and negative  $G_z$  and also during both the plateau and ramp parts of  $G_z$  to reduce the total pulse duration.

### 2.4.2 Unaliasing by Fourier-encoding the overlaps using the temporal dimension (UNFOLD)

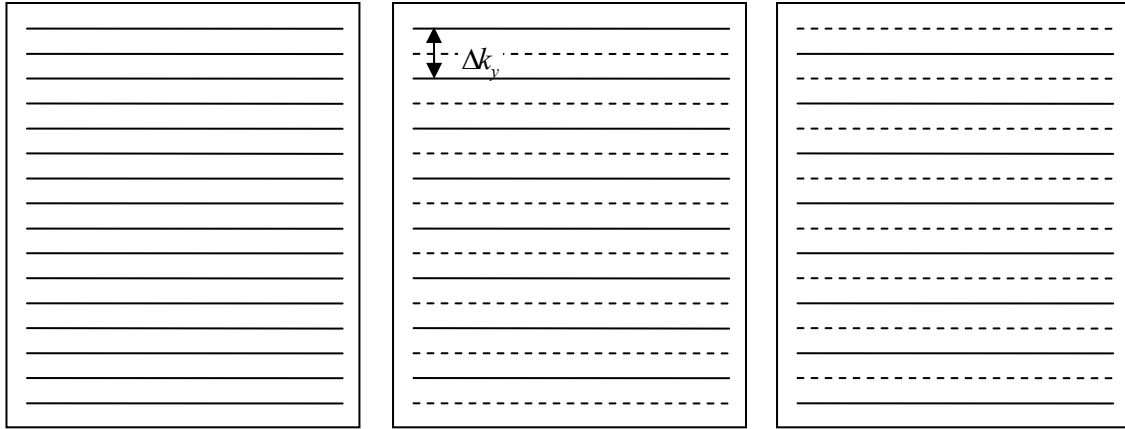
UNFOLD [95] is a temporal strategy designed to reduce scan time for dynamic studies where a continuous set of images are acquired in time. To speed up the acquisition process, UNFOLD uses an FOV smaller than the imaged anatomy, causing the acquired images to be corrupted with aliasing artifacts. By manipulating the evolution of the aliased signals from time-frame to-time frame, UNFOLD can effectively tag the aliased signals so they can be easily identified and filtered out as part of the reconstruction. When the dynamic set of images is acquired, the sampling function in acquisition  $k$ -space is shifted by a fraction  $f$  of a line, and the shift varies from one time frame to the next. (Note that this shifting of the sampling function occurs during the acquisition, not during the excitation.) The effect of the shift is to apply a modulation ( $T_l$ ) through time to any aliased signal:

$$T_l(t) = \exp(i2\pi l \cdot f(t)), \quad (2-4)$$

Where  $t$  is the time frame number and  $l$  is the order of aliasing for a given layer of overlap (e.g.,  $l = 0$  for nonaliased material,  $l = 1$  (or  $-1$ ) for the first layer of overlap in the positive (or negative) direction along the phase-encoding axis, etc.). Preferably,  $f(t)$  is chosen to be a linear function of time, so the modulation is a linear phase ramp through time, which produces a simple shift in the temporal frequency domain [96]. In practice, only the fractional part of  $f(t)$  is used, because shifts by an integer number of lines make no difference on the modulation (Eq. 2-4).

The effect of UNFOLD can be readily explained in the temporal frequency domain [96]. The value of a given image voxel may vary from one time frame to the next in a dynamic set of images, and the FFT of this function with respect to time gives a temporal frequency spectrum for the voxel. The “true” or non-aliased signal tends to appear centered around the DC frequency in this temporal frequency spectrum, and UNFOLD can move aliased signal away from DC due to the applied modulation, to regions in the spectrum that tend to be left mostly unused by the non-aliased signal. After the aliased signal is filtered away, the non-aliased signal is recovered with an inverse FFT.

In this dissertation, UNFOLD displaced aliased signals in the temporal frequency domain as far as possible from the true signal, all the way to the Nyquist frequency. This was done by shifting the  $k$ -space sampling function by a half of a line, resulting in  $f(t) = t/2$ . We used  $|l|=1$ , so Eq. 2-4 became  $T_{\pm}(t) = \exp(i\pi t)$ , with  $t$  being an integer. The  $k$ -space acquisition scheme we employed is depicted in Figure 2-6. The effect of this modulation in phase images of even (*left*) and odd (*right*) time frames in a water phantom is shown in Figure 2-7. The aliased signals are forced to reverse their phase from time-point to time-point (i.e., to flicker in time at the Nyquist frequency). Assuming the image does not change between acquisitions, two peaks are produced in the temporal frequency domain for each voxel: one for the desired signal centered around DC, and another consisting of the aliased signal at the Nyquist frequency. A filter with a full width at half maximum (FWHM) of about 90% of the full temporal frequency bandwidth and centered at the DC frequency was used to remove the aliased signals.



Phase  
↑  
frequency →

Figure 2-6: Sampling scheme for UNFOLD in acquisition  $k$ -space. *Left*: Fully sampled  $k$ -space. *Middle*:  $k$ -space for UNFOLD in odd time frames with an acceleration factor of 2. Dashed lines represent  $k$ -space views that are not acquired. *Right*:  $k$ -space for UNFOLD in even time frames with a half of line ( $\Delta k_y/2$ ) shifted, where  $\Delta k_y$  is the phase-encoding step size.

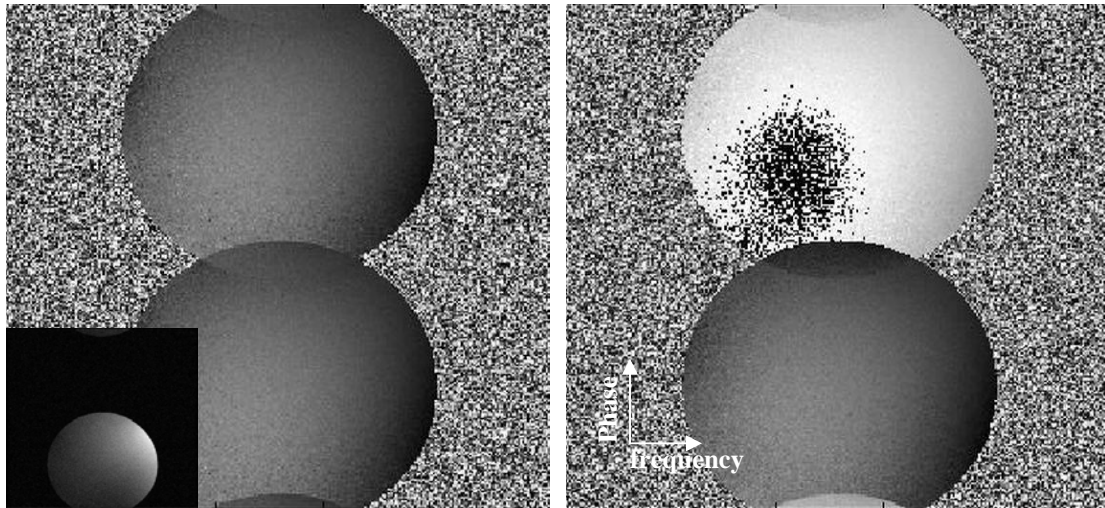


Figure 2-7: Demonstration of UNFOLD modulation in a homogeneous doped water phantom using the GE head coil. *Inset*: magnitude image of a full  $k$ -space sampling before UNFOLD acquisition. *Left/Right*: an even/odd time-frame phase image of an under-sampling  $k$ -space in UNFOLD acquisition. The sampling function was shifted by a half of a  $k$ -space line from one time frame to the next, resulting in reversing phase in the aliased signals.

### 2.4.3 Multiple receiver coil technology (parallel imaging)

Parallel imaging makes use of the sensitivity profile of the different elements in a phased array coil to speed up imaging acquisition and correct the artifacts caused by under-sampling  $k$ -space [97]. Under-sampling reduces the acquisition time, resulting in aliasing in the phase-encode direction(s). Through the use of the information contained in the sensitivity profiles of each element in phased array – which can be measured beforehand – one can “de-alias” the image data and eliminate the wraparound caused by the under-sampling. As shown in Figure 2-8, parallel imaging relies on the fact that the imaged object is “seen” simultaneously by a number of different coils placed at different locations around the imaged anatomy. While numerous different versions of parallel imaging have been developed [97-99], the Cartesian version of SENSE [100] remains commonly used due to its simplicity and relatively short reconstruction time, and was used exclusively in experiments described in this dissertation. Greater acceleration can be achieved with more coil elements.

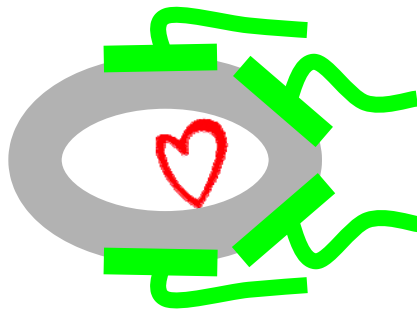


Figure 2-8: Example of an array coil configuration. Parallel imaging relies on the fact that the object can be seen simultaneous

Parallel imaging methods require prior knowledge about the sensitivity profile of each receiver coil. In Cartesian SENSE, this profile is acquired shortly before the actual parallel imaging acquisition and consists of low-resolution maps showing where in space

each coil is sensitive to the MR signal. This information depends on the particular geometry of the coil and where it is located with respect to the patient. Figure 2-9c shows sensitivity maps for four coil elements involved in acquiring the cardiac image of a volunteer's shown in Figure 2-9a. Notice that coil number 1 is very sensitive (high value in the sensitivity map) for tissues located near the chest (on the left in this example), and rather insensitive (low value) to tissues near the back. This is because coil number 1 was physically located over the chest. On the other hand, coil number 4 was placed under the volunteer and was sensitive in regions near the back.

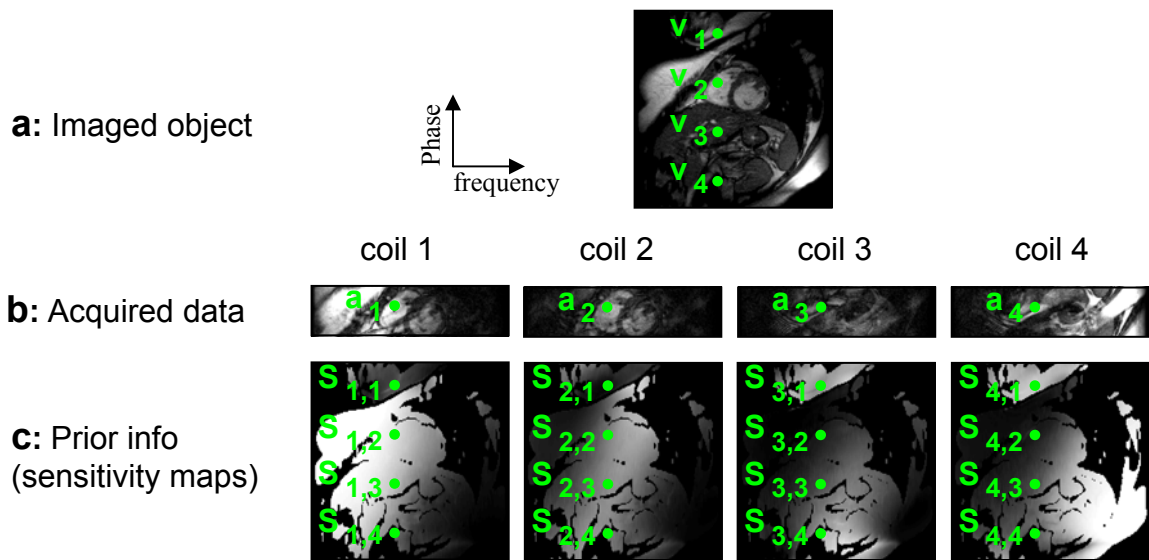


Figure 2-9: Schematic representation of the SENSE reconstruction with four receiver coils. a) Fully reconstructed image of the heart of a volunteer. b) Acquired undersampled images in a parallel imaging acquisition with a reduction factor of 4. The images are aliased due to the accelerated acquisition in parallel imaging. c) Sensitivity maps for individual coils. Parallel imaging requires prior knowledge about the sensitivity of the receiver coils for the image reconstruction. With knowledge of the coil sensitivity at each point ( $S_{nm}$ ), one can determine the de-aliased image values ( $v_n$ ) from the aliased measurement ( $a_n$ ) (Image courtesy of Bruno Madore.)

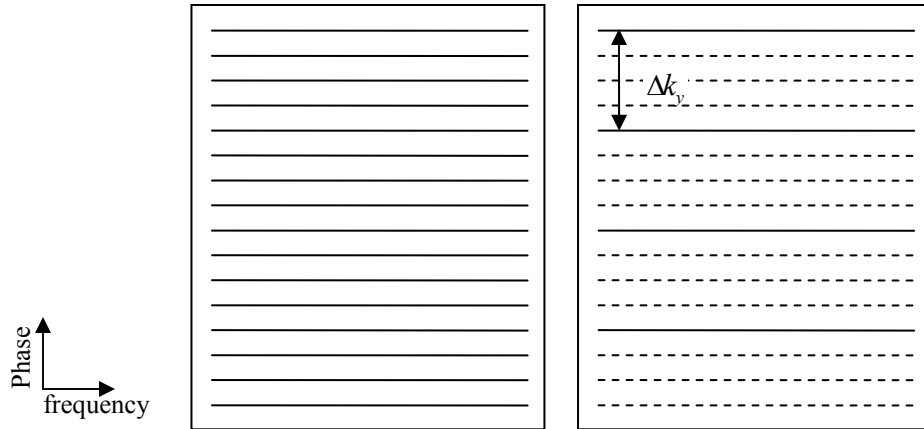


Figure 2-10: Sampling scheme for parallel imaging. *Left:* Fully sampled  $k$ -space. *Right:*  $k$ -space for parallel imaging with an acceleration factor of 4. As compared to the fully sampled data,  $k$ -space was sampled every other four lines in parallel imaging. Dashed lines represent  $k$ -space views that are not acquired.

To accelerate imaging acquisition, the FOV along phase-encoding direction was reduced by a factor of 4, resulting in the aliased images in Figure 2-9b. The corresponding  $k$ -space acquisition scheme is depicted in Figure 2-10. Figure 2-9b was constructed from the combined images from all of the coils. In the image for coil number 1, tissues in close proximity to the coil produce the largest signals, and this is reflected in the in the sensitivity map. As a consequence, when the individual coil images are combined to produce the image shown in Figure 2-9a, the voxels located near coil number 1 are given more weight than those located far away from the coil. On the other hand, the voxels located near coil number 1 are given less weight in the image for coil number 4. The weighting of the different voxels in the image from certain coil is determined by the coil's sensitivity map.

Now consider a voxel in the aliased image from coil number 1 (voxel  $a_1$  in Figure 2-9b). Because of the aliasing, which can be clearly seen in Figure 2-9b, the signal  $a_1$  is

the sum of the signals  $v_1$ ,  $v_2$ ,  $v_3$ , and  $v_4$ . These signals are weighted by the sensitivity of the first coil at these points in the tissue ( $S_{1,1}$ ,  $S_{1,2}$ ,  $S_{1,3}$ , and  $S_{1,4}$ ). Consequently, the signal intensity at  $a_1$  is given by:

$$a_1 = v_1 \times S_{1,1} + v_2 \times S_{1,2} + v_3 \times S_{1,3} + v_4 \times S_{1,4} , \quad (2-5)$$

Similarly, for other coils:

$$a_2 = v_1 \times S_{2,1} + v_2 \times S_{2,2} + v_3 \times S_{2,3} + v_4 \times S_{2,4} , \quad (2-6)$$

$$a_3 = v_1 \times S_{3,1} + v_2 \times S_{3,2} + v_3 \times S_{3,3} + v_4 \times S_{3,4} , \quad (2-7)$$

$$a_4 = v_1 \times S_{4,1} + v_2 \times S_{4,2} + v_3 \times S_{4,3} + v_4 \times S_{4,4} , \quad (2-8)$$

These equations can be rewritten as:

$$\mathbf{a} = \mathbf{S} \mathbf{v} , \quad (2-9)$$

where:

$$\mathbf{a} = \begin{bmatrix} a_1 \\ a_2 \\ a_3 \\ a_4 \end{bmatrix} \quad (2-10)$$

$$\mathbf{v} = \begin{bmatrix} v_1 \\ v_2 \\ v_3 \\ v_4 \end{bmatrix} \quad (2-11)$$

and

$$\mathbf{S} = \begin{bmatrix} S_{1,1} & S_{1,2} & S_{1,3} & S_{1,4} \\ S_{2,1} & S_{2,2} & S_{2,3} & S_{2,4} \\ S_{3,1} & S_{3,2} & S_{3,3} & S_{3,4} \\ S_{4,1} & S_{4,2} & S_{4,3} & S_{4,4} \end{bmatrix} \quad (2-12)$$

All of the values in matrix  $\mathbf{S}$  are known from the information obtained in the sensitivity maps shown in Figure 2-9c. The values in  $\mathbf{a}$  are what is actually measured during the parallel imaging acquisition Figure 2-9b. The values in  $\mathbf{v}$  are obtained by a matrix inversion:

$$\mathbf{v} = \mathbf{S}^{-1}\mathbf{a} \quad (2-13)$$

Repeating the above process for all voxels in Figure 2-9b, we can get the signal intensities for all of the voxels, and therefore reconstruct the image shown in Figure 2-9a. This process is more time-consuming than a normal image reconstruction, but with current processor speeds it can be achieved in near real-time.

### **3 Combining volume-selective RF pulse with parallel imaging and UNFOLD for accelerated MR thermometry imaging**

#### **3.1 Introduction**

Please refer to Section 1.1 for the motivation of this project and literature review of accelerated MR thermometry.

The purpose of this study is to develop a framework for MR thermometry to jointly optimize spatial, temporal, and temperature resolutions, as well as 3D spatial coverage. To speed-up the imaging process, three existing fast-imaging strategies were combined in a synergistic manner: two-dimensional spatially-selective RF excitation [18, 19], unaliasing by Fourier encoding of the overlaps using the temporal dimension (UNFOLD) [95], and parallel imaging [97]. The improvements in temporal resolution enabled by these fast-imaging methods can, in turn, be traded-off when so desired for improvements in spatial resolution, temperature resolution and/or spatial coverage.

In previous work, combinations of UNFOLD with either 2DRF excitation [101] or SENSE parallel imaging [100] and the combination of 2DRF excitations with parallel imaging [102] have been shown to perform substantially better than any of the individual techniques alone. With 2DRF-UNFOLD, the 2DRF excitation suppressed signals from outside the desired ROI thus allowing the use of smaller FOV settings, and any remaining artifacts from the vanishing tails of the excitation profiles were removed by UNFOLD. In the UNFOLD-SENSE method, UNFOLD provided significant suppression of the artifacts and amplified noise sometimes produced by parallel imaging. In 2DRF- parallel imaging,

the minimum duration of 2DRF pulses was significantly reduced by employing an under-sampled rectilinear excitation trajectory, and then using parallel imaging to unwrap signals from the resulting replicated excitation regions.

A 2DRF reduced-FOV approach seems particularly well suited for temperature monitoring during thermal ablation, as the large FOV required to avoid aliasing is often substantially larger than the heated volume. Furthermore, pulse sequences with relatively large TE settings as typically employed in GRE thermometry often include idle periods, allowing regular RF pulses to be replaced by (longer) 2DRF ones. Parallel imaging and UNFOLD are used here to avoid artifacts that might result from imperfect 2DRF profiles, and enable the use of shorter 2DRF pulse durations. All three methods were fused in such a way as to combine their strengths and mitigate their weaknesses. These strategies were implemented on a GRE imaging sequence. The resulting hybrid pulse sequence was tested in experiments in a tissue-mimicking phantom and in ex-vivo tissue using FUS heating. Acceleration factors up to 24 were obtained for temperature mapping.

## 3.2 Theory

### 3.2.1 Reduced FOV imaging using 2DRF excitation

In MRI, when only a small portion of the FOV is of interest and the SNR is not the main limiting factor, it would make sense to reduce the FOV along the phase-encoding direction to reduce acquisition time by acquiring fewer  $k$ -space lines. Doing so, however, leads to aliasing artifacts from the signal outside the desired FOV. A relatively straightforward method to avoid artifacts is to use a 2DRF pulse to limit the excitation in the phase-encoding direction to only the desired region.

In principle, to completely avoid any aliasing artifacts, an RF pulse is required to create one (and only one) excitation lobe within the FOV. This usually results in a long RF pulse, which is undesirable not only because it increases the minimum TR and may prolong scan time, but also because it makes the RF pulse more sensitive to susceptibility effects. If shorter RF pulses were used for 2DRF excitation, the corresponding excitation profile would either become wider, or the excitation lobe would repeat itself within the FOV. Figure 3-1 explores this tradeoff and depicts different schemes for 2DRF excitation along with corresponding excitation profiles. The length of a 2DRF pulse is determined by the number of subpulses it contains, and in Figure 3-1 each subpulse is represented by an arrow. As compared to the 2DRF pulse in Figure 3-1a, the number of subpulses can be reduced by using a sharper Gaussian modulation (Figure 3-1b) or by decreasing the sampling density in excitation  $k$ -space (Figure 3-1c). In Figure 3-1a, a narrow single-lobed excitation profile is obtained at the cost of a relatively long pulse featuring 13 subpulses. An RF pulse nearly twice as short (7 subpulses) can be obtained using a

sharper Gaussian modulation (Figure 3-1b) or a larger  $\Delta k_y$  (Figure 3-1c), although both cases would lead to significant aliasing artifacts in an image acquired with the indicated reduced FOV. The present work involves using a very short 2DRF pulse, as shown in Figure 3-1d, and suppressing any aliasing artifact through a combination of UNFOLD and parallel imaging algorithms.

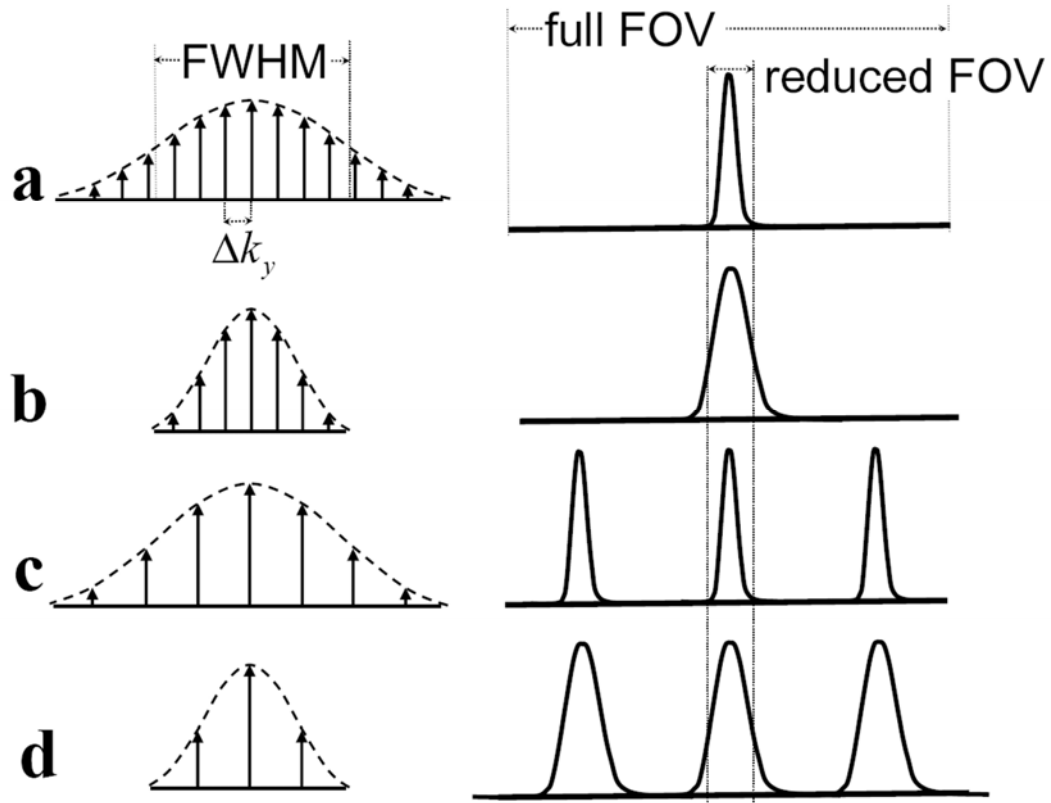


Figure 3-1: 2DRF excitation profiles depend on 2DRF-pulse parameters. The figures on the left represent 2DRF pulses with different timing parameters, and the figures on the right represent the corresponding excitation profiles. Arrows under the dashed lines represent the amplitudes of subpulses, and dashed lines represent the Gaussian modulation envelop of the 2DRF pulses. a) A 2DRF pulse is composed of 13 subpulses, where the excitation  $k$ -space increment in phase-encoding direction is  $\Delta k_y$ , and the Full-Width Half-Maximum of its modulation is FWHM. This long RF pulse excites one narrow lobe within the FOV with width proportional to  $1/\text{FWHM}$ . b) Compared to that in (a), the RF pulse is shortened by using a sharper Gaussian modulation (cutting FWHM in half) while keeping the sampling density in excitation  $k$ -space unchanged (same  $\Delta k_y$ ). The excitation profile for this pulse is twice wider than that in (a), and wraparound aliasing will result if the FOV is reduced as shown. c) Using the same Gaussian modulation width as in (a) but decreasing the sampling density in excitation  $k$ -space (increasing  $\Delta k_y$ ), extra side lobes appear within the FOV. d) Changes are made to both the Gaussian modulation and the sampling density, leading to very short pulses (only 3 subpulses here compared to 13 in (a)), at the cost of a wider excitation lobe and sidelobes, resulting in severe aliasing artifact when reduced FOV images are acquired.

### 3.2.2 *Artifact removal using UNFOLD and parallel imaging*

Figure 3-2 provides an example of the proposed approach, and of the various steps involved. A 2DRF pulse is employed to excite a reduced FOV, and SENSE as well as UNFOLD are used to correct deficiencies in the excitation profile. The very imperfect profile from a short 2DRF pulse is shown in Figure 3-1a, where three smooth lobes appear within the FOV, rather than a single sharp one. These three lobes consist of the main excitation lobe in the center with side lobes an equal distance away on each side. The distance between the main lobe and side lobes can be adjusted to a multiple of the reduced-FOV size, so that all lobes overlap onto each other without spatial shifts in the acquired rFOV images (Figure 3-2c). Parallel imaging is well suited for removing the signal from regions labeled ‘C’ in Figure 3-2a, as there is a large spatial separation between them and the main lobe. It is not as useful, however, for separating the signal from the ‘B’ (and ‘D’) regions from that of the ‘A’ (and ‘C’) regions because they are physically close and are likely to feature similar coil sensitivity. Unlike parallel imaging, UNFOLD is well suited to separate signals from regions that are in close physical proximity. The signal from the transition zones (B and D regions) can be removed using UNFOLD [101], as seen in Figure 3-2d, and the main bulk of the signal from excitation side lobes (C regions) can be removed using parallel imaging, leaving only the non-aliased signal from region A, as seen in Figure 3-2e.

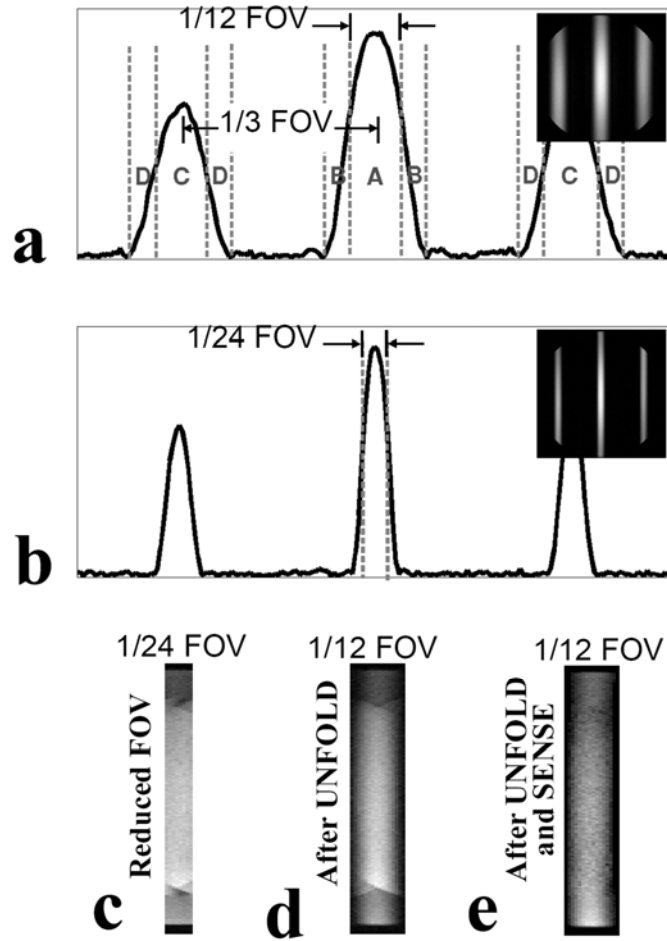


Figure 3-2: The hybrid 2DRF excitations and SENSE plus UNFOLD filtering were tested on a GE 3T scanner by imaging a homogeneous doped water phantom. The number and width of the excitation lobes are adjusted by manipulating the 2DRF subpulse modulation and excitation  $k$ -space sampling density. a) Excitation profiles obtained with a short 2DRF pulse (3.6 ms) composed of 7 subpulses. The lobe width including transition regions is  $1/6$  of the full FOV and the distance between central and side lobes ( $1/3$  FOV) are multiple of the desired reduced FOV ( $1/12$  FOV). b) Excitation profile obtained with 17 subpulses (duration 8.8 ms). c) With 17 subpulses, the FOV was reduced to  $1/24$  of the full FOV, giving 24-fold improvement in temporal resolution. d) Using the short RF pulse with only 7 subpulses whose profile is shown in (a), UNFOLD was used to remove the aliasing onto the central lobe from regions B, D e) The main bulk of the signals from the side lobes (regions C) was then removed using parallel imaging, essentially leaving only the central lobe (region A).

### **3.3 Materials and methods**

#### *3.3.1 Imaging pulse sequences*

All studies were performed on a 3T GE Signa scanner (General Electric Medical System, Milwaukee, WI, USA) with twin-speed gradients (maximum gradient strength 40 mT/m, maximum slew rate of 150 T/m/s). A GE product 2D SPGR gradient-echo sequence was used to measure the PRF shift using phase-mapping, and was modified to incorporate the acceleration method outlined herein. The 2DRF modification was accomplished using functions from a freely available 2DRF pulse library developed within our group (National Center for Image Guided Therapy, or NCIGT, <http://www.ncigt.org>). Functions in the library enable the implementation of echo-planar 2DRF excitation pulses with options that include the number of subpulses, the subpulse durations, the modulation envelope (sinc or Gaussian), and the number of cycles within the envelope. The excitation profile can also be controlled through adjustments in blip gradient strength and phase for each subpulse, through user-defined parameters. The UNFOLD modification involved shifting the acquisition  $k$ -space lines by  $\Delta k_y / 2$  from one time frame of the dynamic image series to the next, where  $\Delta k_y$  represents the increment between trajectories in acquisition  $k$ -space.

#### *3.3.2 FUS experimental setup*

Please refer to Section 2.2.2 for the experimental set-up. The ultrasonic fields were generated by the single-element transducer described in Section 2.1. For all experiments, 30-s continuous wave sonications were delivered. The acoustic power ranged from 10-20 W with the aim of achieving a peak temperature change of less than

15°C, so that consecutive experiments could be performed at the same location without causing thermal damage to the tissue samples. Tissue samples or phantoms were placed on a plastic holder above the transducer and were thick enough to reach the focal depth. The gel phantom used here had rotational symmetry, and its axis was aligned with the main magnetic field to minimize susceptibility effects.

### *3.3.3 2D thermometry in gel phantom*

All heating experiments were performed in a tissue-mimicking phantom (ATS Laboratories, Bridgeport, CT, see reference [103] for properties) heated with FUS. As part of the scan prescription, the focal spot was located by imaging temperature changes during short-duration sonications. Excitation profiles from our 2DRF pulse were measured (e.g., see Figure 3-2b) based on full-FOV SPGR images (FOV: 16×16 cm, TR/TE: 40/20 ms, matrix size: 192×192, flip angle: 30°, slice thickness: 5 mm, bandwidth: ±15.6 kHz, high order shim applied). The 2DRF pulse used here consisted of 17 subpulses modulated with a Gaussian envelope, with total duration of 8.8 ms. The location and size of the central excitation lobe was adjusted so as to cover the FUS focal spot (by adjusting the blip gradient size and the phase of the subpulses). Sonication parameters such as RF power, pulsing period, duty cycle, and duration were set at the FUS workstation, outside the scanner room.

During the heating experiment, our modified SPGR sequence was used for temperature mapping purposes. Dynamic images were acquired continuously for 90 s, using the same imaging parameters as described above except for the FOV size, which was reduced by a factor of 24 in the phase-encoding direction (matrix size: 192×8). An

acoustic power of 12 W was delivered throughout a 30-s period, after which transmission was stopped and the phantom was allowed to cool. Images before heating were used as baselines in post-processing. Image reconstruction, phase-difference calculations and data analysis were all performed in the MATLAB programming language (MathWorks, Natick, MA).

Temperature measurements obtained using our accelerated approach were compared with results obtained using the same SPGR sequence with regular RF pulse and full FOV (called ‘full SPGR’ below). Comparisons involved different heating experiments performed with identical sonication parameters. Consecutive sonication experiments were separated by ten-minute cooling periods to allow the temperature to return near baseline. Overall, 5 different heating locations and a total of 14 sonication experiments in the gel phantom were imaged using 2D thermometry.

#### *3.3.4 2D thermometry in bovine muscle*

Additional tests were performed in ex vivo bovine muscle. Fresh, never-frozen bovine muscle from a grocery store was used. Each specimen was degassed in a saline solution under vacuum (650 mmHg) for at least one hour before use. Areas free of large vessels and fat were selected for sonication to avoid distortion of the ultrasound beam and imaging artifacts. The same prescription steps as described above were performed, and the same imaging parameter and 2DRF pulse parameters were used. Results were again compared to those obtained from a ‘full SPGR’ sequence.

### 3.3.5 3D thermometry in gel phantom

A GE product 3D SPGR sequence was modified to incorporate our proposed hybrid acceleration method. As compared to the 2D experiments described above, a very different excitation profile along  $z$  was obtained in the present 3D implementation (slab excitation rather than slice excitation) but, on the other hand, the excitation profile along the phase-encoding direction  $y$  remained essentially unchanged. Accelerated 3D acquisitions were performed in a gel phantom, which was heated for 30 s with FUS at an acoustic power of 20 W. The 3D rFOV images were acquired during heating and cooling (FOV:  $0.7 \times 16.0 \times 12.0$  cm, TR/TE: 40/20 ms, matrix size:  $192 \times 8 \times 24$ , flip angle:  $30^\circ$ , slice thickness: 5 mm, bandwidth:  $\pm 15.6$  kHz). The first 8 s of scanning, before sonication started, were used to establish a pre-heating baseline. All measurements were compared to those obtained using the GE product 2D SPGR sequence. The slice position for the 2D sequence was set to coincide with the center of the imaged volume for the 3D sequence.

### 3.3.6 Real-time processing and display

An implementation of the proposed approach with real-time reconstruction and display was tested during FUS heating of the gel phantom. The real-time implementation required the integration of three separate systems: the MRI scanner, our Dynamic Adaptive Real-Time Software System (DARTS), and 3D-Slicer. Both DARTS and 3D-Slicer are publicly available software packages available through the NCIGT. DARTS involves low-level software written in the C language, which enables real-time acquisition and reconstruction of MRI images. Written in C++, 3D-Slicer is primarily a display and post-processing software package. An external workstation loaded with both

DARTS and Slicer was connected to the MR scanner via an Ethernet cable. Reconstruction modules were added to DARTS, to handle UNFOLD and SENSE reconstructions.

Prior to the heating experiment, a 3D FGRE image dataset was acquired for the volumetric display in Slicer. The 2DRF pulse consisted of 5 subpulses, for a total duration of 2.6 ms. As usual the main excitation lobe was centered on the FUS focal point. The 2D implementation of our proposed thermometry approach was used, over a 20-min period, to follow the temperature changes that occurred as sonication (16 W, 30 s duration) was turned on and off (FOV: 2.3×18.0 cm, TR/TE: 40/17 ms, matrix size: 128×16, flip angle: 30°, slice thickness: 8 mm, bandwidth: ±5 kHz, imaging plane: axial). Acquired data were fed into DARTS for reconstruction with UNFOLD and SENSE algorithms, and the resulting images were then passed on to Slicer for display.

### *3.3.7 Image reconstruction*

The data acquired with our modified pulse sequences were reconstructed using SENSE and UNFOLD algorithms, and the resulting images were processed to generate dynamic temperature maps. A 24-fold acceleration was obtained by using a 2DRF pulse that essentially excites only about a fraction 6/24 of the FOV along the phase-encoding direction (see Figure 3-2b), along with UNFOLD (2-fold acceleration) and parallel imaging (3-fold acceleration). In the actual reconstruction programs, the 24-fold acceleration was obtained through a 2-fold UNFOLD acceleration and a nominal 12-fold SENSE acceleration, but since no more than 3 of the 12 layers separated by SENSE are ever non-zero, the actual SENSE acceleration is 3.0 (not 12.0). The UNFOLD

implementation differed slightly between the non real-time and real-time experiments. For non real-time experiments, all images in the time series were employed during the UNFOLD processing (i.e., non-causal implementation), whereas for real-time experiments, only the most recent 12 time frames were employed (i.e., causal implementation). For the ‘full SPGR’ data, a non-accelerated SENSE algorithm (acceleration factor = 1) was used to combine images from different coil elements in an SNR-optimum fashion [104].

The phase difference between a (coil-combined) image  $Z_t$  acquired at time  $t$  and a pre-heating baseline  $Z_0$  was calculated by:

$$-\pi \leq \Delta\Phi = \text{phase}(Z_t / Z_0) = \text{phase}(Z_t Z_0^*) \leq \pi \quad (3-1)$$

where \* denotes complex conjugation. Maps of temperature change were generated, using TE values along with the known temperature dependence of the PRF (-0.01 ppm/°C, or -1.28 Hz/°C at 3T) [78]. For display purposes, an ROI of 3x5 voxels (2.5x4.2 mm in size) centered within the FUS focal spot (full-width-half-maximum 5x10 mm in size) was selected when plotting temperature curves for 2D imaging experiments, while a single voxel ROI was selected for 3D experiments. Temperature-to-noise ratio analysis was performed by acquiring data without actual heating. To cancel the effects of any slow phase drift, consecutive temperature time frames were subtracted two-by-two. The temperature noise was then taken as the standard deviation along the time axis over all pixels in the same ROI as described above.

### 3.3.8 Statistical analysis

Temperature data from fourteen 2D imaging experiments performed in our gel phantom were employed toward evaluating the precision and accuracy of our proposed approach. Linear regression analysis (calculation of slope,  $y$  intercept, and correlation coefficient) was used to compare temperature changes obtained from the present accelerated hybrid method and those obtained from a ‘full SPGR’ reference. As a 24-fold higher temporal resolution was reached using our accelerated hybrid method, only the time points that corresponded most closely with the time locations sampled in the ‘full SPGR’ reference were actually involved in the comparison. Since there were 12 time points per experiment in the reference datasets, the total number of time points available for analysis was 168 (i.e., 14 experiments  $\times$  12 time points/experiment = 168 time points). The Bland-Altman technique was used to evaluate the agreement, and the limits of agreements were defined as the mean difference  $\pm 1.96$  standard deviations [105]. Furthermore, using a Student  $t$ -test, the hypothesis that no significant difference exists between results from our method and the ‘full SPGR’ reference was tested, and the correlation coefficient was calculated. We repeated these tests after temporally averaging the results from our hybrid method (24-fold, sliding window), so its temporal resolution would be lowered to the same level as that of the ‘full SPGR’ reference. Doing so allowed an SNR-equivalent comparison of our approach and the reference. As compared to the first set of tests described above, in which time points were simply picked rather than averaged, one would expect the deviation in Bland-Altman plots to become smaller and the mean difference to remain unchanged.

## 3.4 Results

### 3.4.1 2D thermometry

Examples of MR temperature measurements, with our proposed accelerated hybrid approach and with a ‘full SPGR’ reference, are shown in Figure 3-3 for both gel and bovine muscle experiments. Temperature changes in a 3x5 ROI at the focus of heating are displayed using ‘x’ markers for our proposed method and ‘o’ markers for the reference. It can be seen from Figure 3-3 that both measurements appear to agree, although results from our method clearly have much higher temporal resolution and, as a direct consequence, greater noise levels. Both methods used the same settings for TR/TE (40/20 ms), and the temporal resolution for ‘full SPGR’ was  $192 \times TR = 7.68$  s while for our proposed approach it was 0.32 s instead (i.e., 24-fold improvement). In theory, a noise penalty by a factor of  $\sqrt{24} = 4.9$ , might be expected, which is roughly consistent with the noise levels that were measured (in gel:  $\pm 0.7^\circ\text{C}$  for the accelerated method and  $\pm 0.1^\circ\text{C}$  for the reference, in bovine muscle:  $\pm 0.8^\circ\text{C}$  for the accelerated method and  $\pm 0.2^\circ\text{C}$  for the reference).

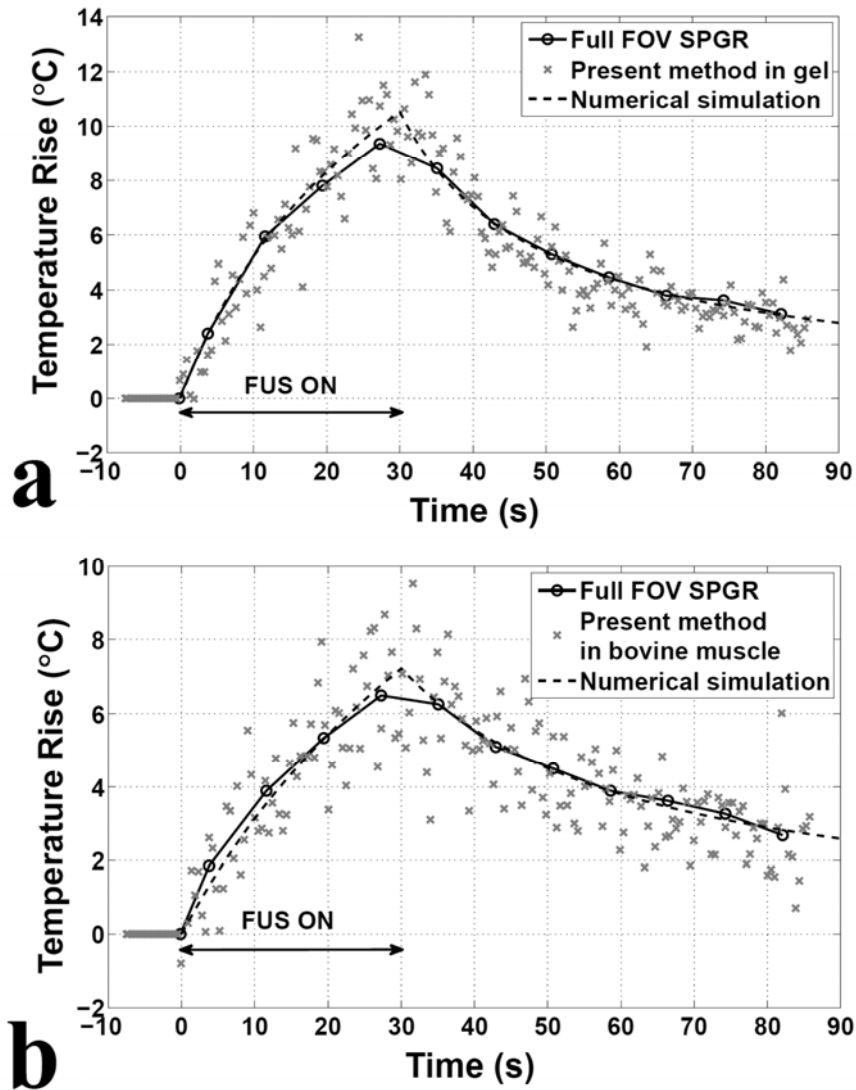


Figure 3-3: MR temperature measurements and numerical simulations from the ROI at the focus of heating during and after FUS treatment of a gel phantom (a) and bovine muscle (b). The graph shows the temperature changes for the modified sequence using a 2DRF pulse consisting of 17 subpulses in reduced FOV imaging (cross markers) compared to the results using a 2DRF pulse consisting of 1 subpulse in full FOV imaging (circle markers). For comparison, the same TE/TR (20/40ms) and matrix size (192 by 192) were used for both sequences. The temporal resolution of the full FOV imaging is 7.68 s, compared to 0.32 s for the modified sequence, giving a 24-fold improvement. The modified sequence with SENSE-UNFOLD reconstruction substantially improved temporal resolution while arguably preserving tolerable temperature uncertainties (0.7 °C in gel phantom and 0.8°C in bovine muscle).

Temperature maps overlaid on full FOV magnitude images are shown in Figure 3-4, to help compare the present approach with ‘full SPGR’. The time frame with maximum heating is shown, in an experiment performed with ex-vivo bovine muscle. Temporal averaging was performed in the accelerated approach to make the SNR comparable to that of ‘full SPGR’. Student *t*-test was performed in the area within the contour on a voxel-to-voxel basis. Result showed a fail of rejection to the null hypothesis; statistically, there was no significant difference between these two focal regions. Areas of the heating envelopes were also compared. The area within the low level of the contour (2.6°C) for the ‘full SPGR’ image was 153 mm<sup>2</sup> while the area for the accelerated image was 120 mm<sup>2</sup>. For the high level of the contour (5.2°C), it was 25 mm<sup>2</sup> for the ‘full SPGR’ and 22 mm<sup>2</sup> for the accelerated data. Result showed similar areas for the high-level of heating envelopes. Differences between the two examples in voxels with low-level heating are expected from noise considerations.

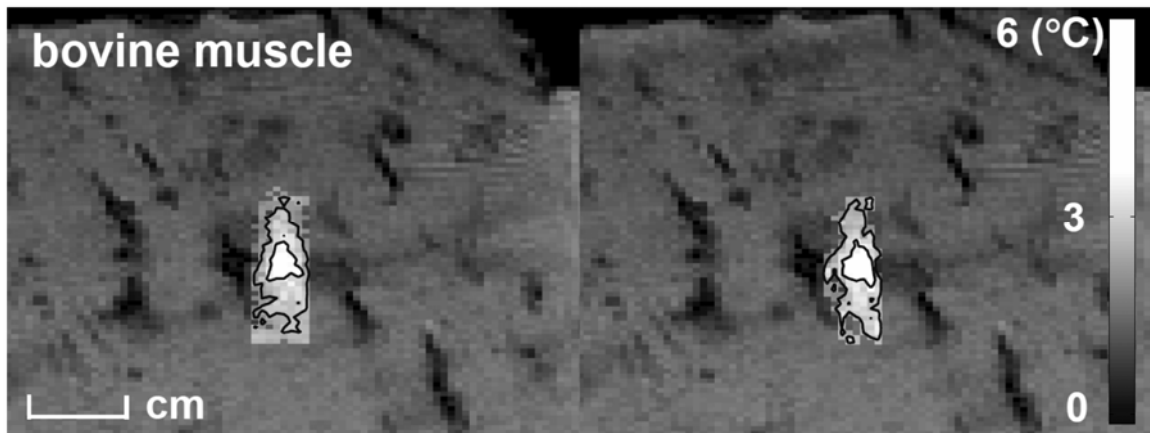


Figure 3-4: Temperature maps of the time frames with the maximum heating obtained from the present approach (right) and a SPGR sequence (left) in an ex-vivo experiment. The map obtained from the present approach was averaged over 24 time frames. A 2°C threshold was applied on both maps. Iso-temperature contours are shown for two different levels, at 2.6°C and at 5.2°C. Results from both methods present similar heating profiles.

While Figure 3-3 features results from only one of the fourteen experiments that were performed in the gel phantom using our modified 2D imaging sequence, in contrast, Figure 3-5 is meant to aggregate and analyze data from all fourteen experiments. As explained above, the analysis was performed twice: once on data where one time point every 24 was picked from the high-temporal resolution datasets (Figure 3-5a,c) and once on data where temporal averaging was used to reduce temporal resolution by 24-fold, down to the level of the reference dataset (Figure 3-5b,d). Good correlation was found through linear regression ( $R = 0.91$  in Figure 3-5a,  $R = 0.98$  in Figure 3-5b) and the mean difference was small ( $0.1^{\circ}\text{C}$  in both Figure 3-5c and d). While the standard deviation of the difference was larger in Figure 3-5c ( $1.4^{\circ}\text{C}$ ) due to relatively high noise levels in the accelerated results, a smaller deviation was observed as expected in Figure 3-5d ( $0.6^{\circ}\text{C}$ ) when using averaged data. The  $1.4/0.6 = 2.33$ -fold reduction in standard deviation was similar to its theoretically expected value of 2.47-fold, as obtained through noise propagation considerations, as listed in Table 3-1 (line 9 divided by line 10,  $\sqrt{55/48}/\sqrt{9/48} = 2.47$ ).

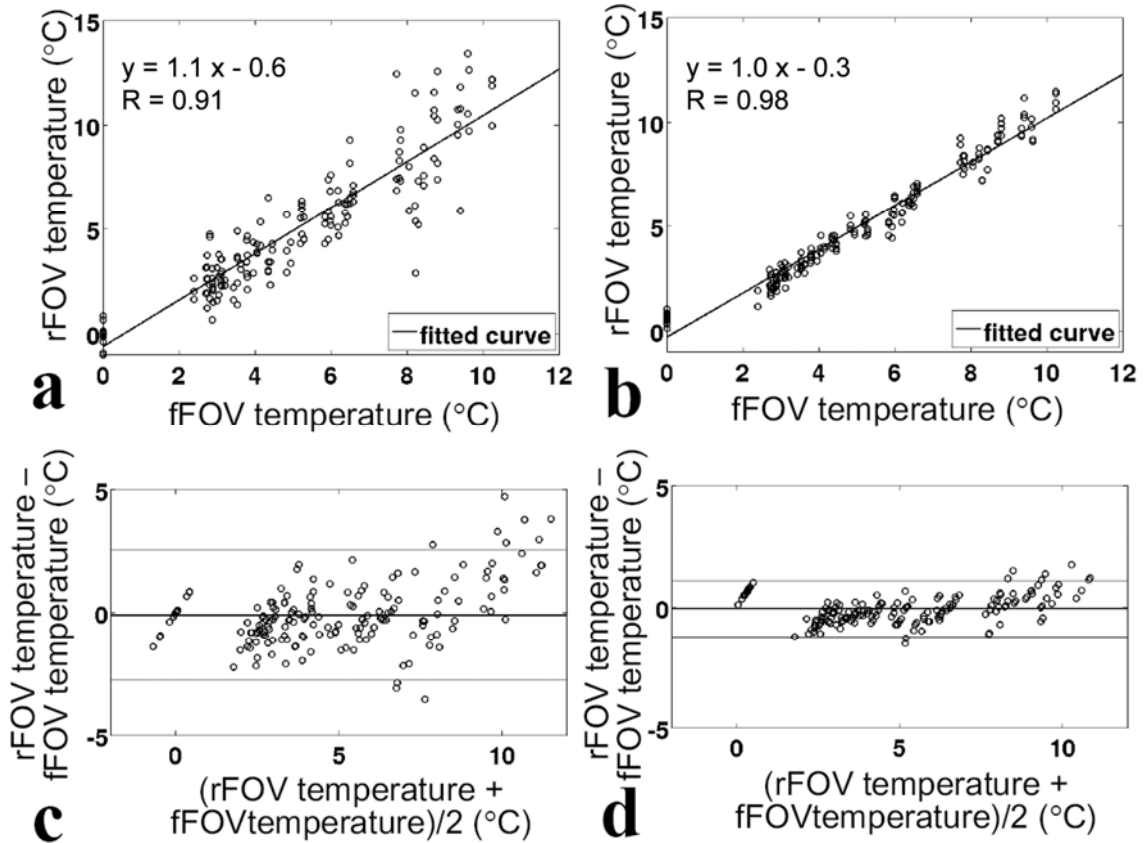


Figure 3-5: Scatterplots (*top*) and Bland-Altman plots (*bottom*) comparing of temperature measurements obtained using the present accelerated method with those obtained using full FOV SPGR sequence for 168 measurements acquired during 14 sonications. a), c), comparison using individual measurements from accelerated sequence. b), d), comparison using time-averaging over 24 frames in the rFOV measurements. The mean difference between measurements for the time-averaging scenario remained at 0.1°C, while standard deviation was reduced from 1.4°C to 0.6°C. In a and b, solid lines represents linear regression. In c and d, central lines represent average of difference, upper and lower lines represent  $\pm 1.96$  standard deviations (95% confidence intervals).

Dataset	Variance	Relative Standard Deviation
1. Dataset for rFOV (24-fold acceleration)	$\sigma^2$	1
2. Dataset for averaged rFOV (average over 24 frames)	$\sigma^2/24$	0.20
3. Baseline for rFOV (average over 16 preheating dataset)	$\sigma^2/16$	0.25
4. Temperature mapping for rFOV (difference b/w 1 and 3)	$\sigma^2+\sigma^2/16$	1.03
5. Temperature mapping for averaged rFOV (difference b/w 2 and 3)	$\sigma^2/24+\sigma^2/16$	0.32
6. Dataset for fFOV (no acceleration)	$\sigma^2/24$	0.20
7. Baseline for fFOV (1 preheating image)	$\sigma^2/24$	0.20
8. Temperature mapping for fFOV (phase difference b/w 6 and 7)	$\sigma^2/24+\sigma^2/24$	0.29
9. rFOV temperature – fFOV temperature (difference b/w 4 and 8)	$\sigma^2+\sigma^2/16+\sigma^2/24+\sigma^2/24$	1.07
10. averaged rFOV temperature – fFOV temperature (difference b/w 5 and 8)	$\sigma^2/24+\sigma^2/16+\sigma^2/24+\sigma^2/24$	0.43

Table 3-1: Noise propagation considerations for Bland-Altman plots.

Based on data from Figure 3-5d, for 95% of the measurements (159 of 168), temperature values from our proposed approach and the reference agreed within  $\pm 1.2^\circ\text{C}$ . Furthermore, a Student *t*-test performed on both time-averaged and non-time-averaged data showed that measurements from the proposed approach and from the reference did not significantly differ.

As can be observed in Figure 3-5d, the difference between accelerated and non-accelerated datasets tended to have a bias toward positive values for higher temperatures, i.e., near the peak temperature. We suspect this might be caused by the lower temporal resolution of the reference ‘Full SPGR’ data, too low to accurately catch the peak temperature. Accordingly, the reference datasets would provide peak temperature-

estimates that are systematically too low, due to temporal averaging effects. Simulations were performed to verify this point. Data from the reference sequence were fitted using two distinct heating models: one based on simple rising and then decaying exponentials, and one more complex based on Pennes' bioheat transfer equation (fitted thermal properties were  $k=0.1\times 10^{-7}\text{m}^2/\text{s}$  and  $c_v=3.8\times 10^6\text{ J/m}^3/^\circ\text{C}$ , where  $k$  is the thermal diffusivity and  $c_v$  is the heat capacity per unit volume). Fitting based on Pennes' model is shown using dashed-lines in Figure 3-3. Using averaging windows that correspond to both the reference and accelerated temporal resolutions, we found a peak-temperature difference of about 0.3 °C (exponential model) or 0.8 °C (Pennes' model). While we cannot be sure that the bias as observed in Figure 3-5d is entirely caused by the effect described here, we note that the bias has the correct polarity (the accelerated values are higher), and roughly the correct size, suggesting the bias near peak temperatures might indeed be caused by differences in temporal resolution and corresponding averaging effects.

### 3.4.2 3D thermometry

While the present acceleration method can be employed to increase temporal resolution (e.g., Figure 3-3), doing so comes at a price in temperature-to-noise ratio (TNR). On the other hand, the proposed method can alternately be used to improve 3D spatial coverage instead, at no cost in terms of SNR. In Figure 3-6, reduced in-plane FOV 3D temperature measurements (solid lines) are compared to results using a 'full SPGR' 2D sequence (dashed line). With the proposed rFOV 3D sequence, in-plane coverage is reduced by a factor of 24 and through-plane coverage is increased by the same amount.

Accordingly, the ROI (focus) was imaged in 3D. Note that temporal resolution and TNR are the same as with the ‘full SPGR’ 2D sequence, but that spatial coverage has the shape of an elongated box rather than a slice. Temperature measurements in the central slices of the acquired 3D volume (slices #11 and #12 out of 24) were similar to those obtained using the single-slice reference sequence, while other slices in the 3D volume featured much smaller temperature changes (Figure 3-6).

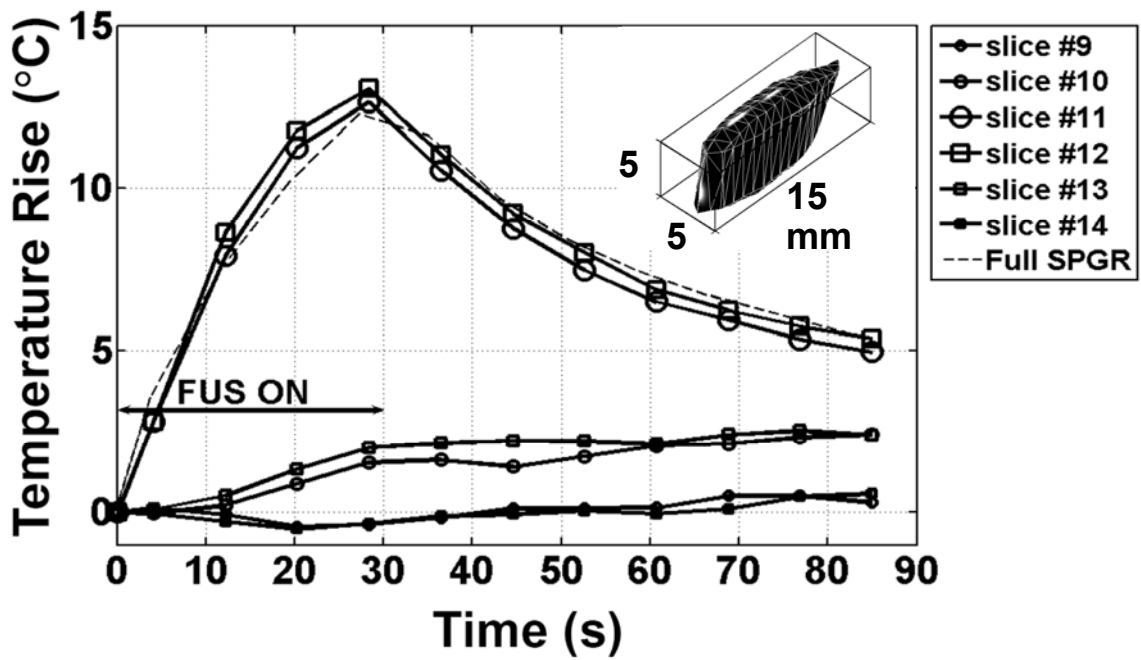


Figure 3-6: Temperature changes of the hottest voxel of 6 middle slices in 3D gel experiments were plotted in solid lines. The dashed line shows temperature measurements for the full-FOV SPGR sequence. The full SPGR sequence gave the similar result to slices #11 and 12 of the accelerated 3D sequence since they were around the same slice location. Inset: inset showing a three-dimensional isosurface where the temperature rise was greater or equal to 9°C. These temperatures were reached in slices #11 and 12.

### *3.4.3 Real-time processing and display*

The term ‘real time’ is used here to convey the fact that acquired data were displayed, with reasonably small latency, as the multi-frame scan progressed. It should be noted however that a fully real-time implementation would further include real-time control of sequence parameters and of the FUS beam in terms of steering and output power, which was not the case here.

Figure 3-7 shows a screen snapshot of the Slicer display 30 s into a phantom heating experiment during which temperature maps were continuously acquired, processed, and displayed. The top panel displays the 3D object, overlaid with a temperature-sensitive image in the axial plane. Three orthogonal tomographic planes from the 3D images are displayed in the bottom panel. The bottom middle and bottom right images are sagittal and coronal baseline images from the gel phantom, respectively. The bottom left image is in the axial orientation, the transducer can be seen in the upper portion, and temperature changes are displayed as a color overlay. Images were acquired at a rate of about 1 fps, and the corresponding temperature maps were reconstructed and displayed with a latency of less than one frame.

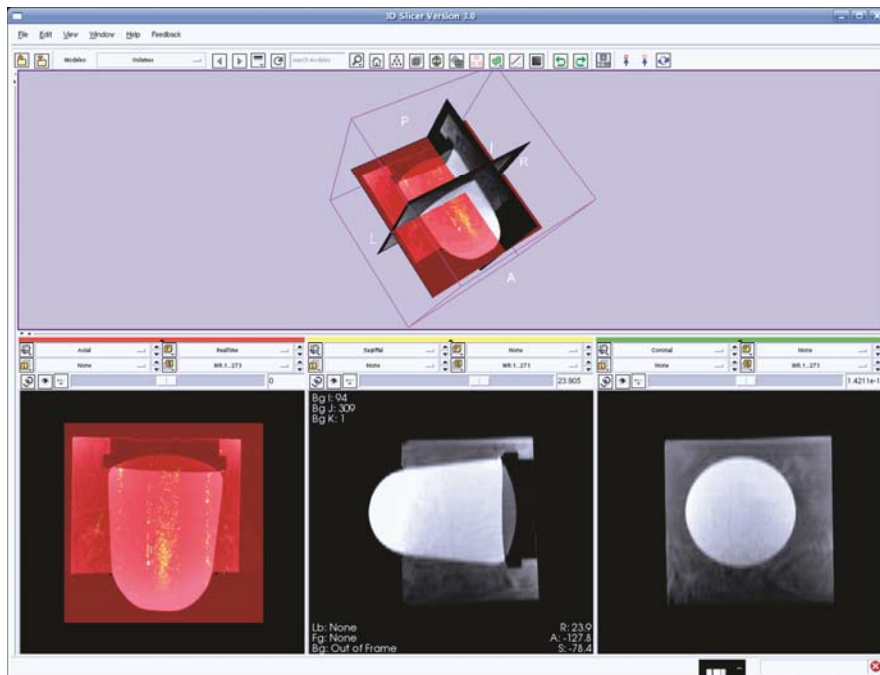


Figure 3-7: Screen snapshot from 3D-Slicer, the display software package. The bottom-left image displays a snapshot during the real-time imaging, processing, and display. The temperature map was updated in real-time, and heating effects can be seen in the bottom-left image as a yellow overlay onto a baseline axial image. The transducer can be seen at the top of the gel in the bottom-left image.

### 3.5 Discussion and conclusions

The present work was aimed at accelerated imaging, and more specifically at accelerated MR thermometry imaging. Using the proposed approach, we demonstrated that acquisitions could be substantially accelerated in FUS temperature mapping experiments, with acceleration factors as high as 24-fold. To account for the effect of the UNFOLD temporal filter (FWHM = 90% of the bandwidth), it is often useful to define an “effective acceleration” factor, equal here to  $0.9 \times 24 = 21.6$ -fold. This 21.6-fold acceleration can then be spent in a number of different ways. The method was used here either to improve temporal resolution (at an SNR cost), or to enable 3D coverage (at essentially no SNR cost). In one particular experiment a product SPGR sequence provided a temporal resolution of only 7.68 s/frame, while our accelerated version of this same sequence achieved 0.32 s/frame in both gel and ex-vivo experiments. Improvements in temporal resolution do, however, come at a price in terms of SNR. Alternately, we also implemented our approach onto a 3D sequence, and showed how acceleration could be used here to enable 3D coverage, with essentially no reduction in SNR. Results were obtained with the same temporal resolution and noise properties as in the 2D non-accelerated case, but with 24-slice 3D coverage. In this example, full-FOV coverage in the  $y$  phase-encoding direction was sacrificed to generate through-slab coverage in the  $z$  direction, leading to an elongated box-like coverage arguably better suited to monitor heating from an FUS beam than a more usual 2D-slice coverage. When used in this fashion, the technique essentially provides flexibility toward tailoring the imaged volume to the heated zone. In cases where peripheral heating may be expected, for example when

the ribs or skull are on the path of the FUS beam, especially careful thought should be given to the shape and orientation of the desired FOV.

Statistical analyses find no significant difference between the accelerated sequence and the gold-standard SPGR sequence; this new accelerated method is as accurate as the conventional sequence. As in any other sequences, the acceleration comes with the cost of SNR reduction, giving rise to an increase in temperature noise. The hybrid method, however, offers a unique feature that other fast imaging sequences could not provide: a trade-off between acceleration and spatial coverage along phase-encoding direction. The ability of the hybrid method to be able to implement with a 3D sequence enhanced this feature, since now we have two spatial directions to tradeoff acceleration, and helps to develop a framework. This framework is used to choose acquisition parameters in a specific situation for optimal compromise between SNR, spatial/temporal resolutions, and spatial coverage in  $y$  (phase-encoding) and  $z$  (slice-encoding) directions. For example, in a situation where a thermometry needs to be fast but can only afford  $8\times$  acceleration for the cost of SNR with a given voxel size, the hybrid method can be used to reduce the spatial coverage in  $y$  direction by 4 and increase the spatial coverage in  $z$  direction by 2, or reduce the spatial coverage in  $y$  direction by 2 and increase the spatial coverage in  $z$  direction by 4, depending upon the shape and size of the ROI. A simple relation holds:

$$R_y = R_z \times R_t \tag{3-2}$$

where  $R_y$  and  $R_z$  denotes the spatial reduction factor along phase- and slice-encoding direction, respectively, and  $R_t$  denotes reduction factor in total scan time, and  $R_y \leq 24$

(because the maximum acceleration of the hybrid method with respect to the SPGR is 24). The framework facilitates the choice of acquisition parameters to achieve the optimal compromise for a specific situation, especially when SNR is limited.

While the present method was implemented on a regular gradient-echo sequence, with a single  $k$ -space line acquired per TR period, it could be combined instead with fast pulse sequences such as echo-planar [8] or spiral [9] imaging, for example. The present method is based on RF pulse (2DRF) design, receiver coils (SENSE), and a temporal strategy (UNFOLD); as such, it is not limited to the gradient-echo sequence used here. For example, Stafford *et al.* [9] reported a temporal resolution 0.58 s/image with a spiral sequence, and the proposed approach could be used to further improve temporal resolution (as far as SNR permits). Similarly, in a recent study by Holbrook *et al.* [17] EPI has been used to achieve 3.43 frames per second, with temperature noise below 0.5°C. When combined with EPI, the present approach could enable a reduction in the number of shots and/or a reduction in the echo-train-length, for reduced distortion. As compared to the present implementation based on a regular gradient-echo sequence, an EPI implementation would not feature any SNR or TNR advantage, but rather a spatial-coverage advantage. SNR is proportional to  $V \times \sqrt{T}$ , where  $V$  is the voxel volume and  $T$  the total sampling time, given by  $T = N_{tr} \times N_e \times \tau$ , where  $N_{tr}$  is the number of TR periods required to build an image,  $N_e$  is the number of echoes per TR period, and  $\tau$  is the readout period. With SPGR,  $N_e = 1$ , and our method speeds up the acquisition process by reducing  $N_{tr}$ . With interleaved EPI,  $N_e > 1$ ,  $\tau$  is reduced by a factor  $N_e$ , and the factor  $N_e \times \tau$  is thus left mostly unchanged. Just like with our method, interleaved EPI reduces scan

time by reducing  $N_{tr}$ , with essentially the same effect on SNR, for equivalent acceleration. We have measured the TNR for accelerated SPGR and interleaved EPI in a gel phantom, confirming that with equivalent voxel size, bandwidth, TR and temporal resolution, the TNR of the present method was comparable to that from gradient-echo EPI. Table 3-2 shows different acquisition scenarios along with expected and measured TNR values.

	<b>Matrix Size</b>	<b>Temporal Resolution</b>	<b>Acceleration Factor</b>	<b>Expected TNR</b>	<b>Measured TNR</b>
<b>a) Full-FOV SPGR (2D)</b>	<b>192x192x1 1 average</b>	<b>7.68 s</b>	<b>1</b>	<b>1</b>	<b>1<sup>*</sup></b>
<b>b) Proposed rFOV method (2D)</b>	<b>192x8x1 1 average</b>	<b>0.32 s</b>	<b>24</b>	<b>0.20</b>	<b>0.18</b>
<b>c) Proposed rFOV method (3D)</b>	<b>192x8x24 1 average</b>	<b>7.68 s</b>	<b>1</b>	<b>1</b>	<b>0.86</b>
<b>d) Full-FOV EPI (ETL=4)</b>	<b>192x192x1 4 averages</b>	<b>7.68 s</b>	<b>1</b>	<b>1</b>	<b>0.95</b>

\*Temperature noise of Full-FOV SPGR in a gel was 0.1°C.

Table 3-2: TNR estimation for scenarios involving different sequences and parameters.

For each line in Table 3-2, datasets were acquired both with a full-FOV SPGR sequence and with the sequence listed in the leftmost column, in a gel phantom. Temperature maps were generated and temperature noise was evaluated. The rightmost column gives the measured TNR, normalized by that measured in the corresponding full-FOV SPGR dataset. In line with the explanation above, the advantage of interleaved EPI compared to our proposed approach is not SNR or TNR, but spatial coverage. Our method provides a limited FOV, while EPI could provide a full FOV. On the other hand, interleaved EPI is not without weakness. For example, interleaved EPI often suffers from distortions, signal voids, and ghosting. Our accelerated SPGR method can be seen as an alternative to interleaved EPI, where some spatial coverage is sacrificed in order to avoid

EPI-related problems, at no cost in TNR. The implementation of the present approach with EPI sequences is expected to achieve high temporal resolution and is performed in Appendix A.

Even though the proposed accelerated method requires longer (2D) RF pulses than the (1D) pulses typically employed, it should be noted that TR and thus imaging time were not affected. Since TE in PRF temperature imaging is usually relatively long (equal to  $T_2^*$  of the tissue for higher TNRs [106]), it is possible to play out a somewhat longer RF pulse without having to increase TR. However, with TE defined as the time between the middle of the RF pulse and the echo, longer RF pulses may lead to shorter TE values and slightly reduced TNR values. Furthermore, when using long RF pulses (about 10 ms here) susceptibility-related effects can be a concern. These problems can, however, be mitigated to a large degree through the use of high order shimming.

It should also be noted that for accurate temperature measurements in vivo, the 2DRF excitations used here should further allow fat suppression. We recently implemented pulses that exploit the chemical-shift sensitivity of 2DRF pulses to obtain spatially-varying water-fat excitation patterns and fat-suppressed regions, toward reduced-FOV accelerated imaging [107, 108]. In a cheese phantom (about 20% of fat), accurate temperature measurements were obtained through to successful suppression of fat signals. A method by K Sung, et al, was also proposed to remove fat signal in conjunction with 2DRF excitations [109]. The robustness of the hybrid technique with respect to the cancelation of fat signal is investigated in Appendix B.

To conclude, an accelerated imaging method was presented that combines 2DRF excitations, UNFOLD, and parallel imaging. The method was targeted toward fast MR thermometry imaging, and acceleration factors up to 24-fold were obtained to increase temporal resolution and/or through-plane spatial coverage. We demonstrated a real-time implementation with low acquisition-reconstruction-display latency. The method showed good temperature accuracy, is reasonably easy to implement (using our 2DRF library) and to prescribe (2DRF parameters were adjusted from the console). The proposed approach can allow faster imaging for better motion tracking, and/or flexible 3D coverage to more closely adapt the image FOV to the shape of the heated region.

## **4 Ultrafast 1D MR thermometry using phase or frequency mapping**

### **4.1 Introduction**

The purpose of the present study is to test a one-dimensional method for rapidly monitoring temperature changes. The ultimate goal is to monitor heating induced by short ultrasound pulses in moving organs, such as the heart. To this end, a line scan echo planar spectroscopic imaging sequence [110] (LSEPSI) was tested for thermometry via frequency and phase mapping.

In previous work, LSEPSI was demonstrated for temperature monitoring in the breast in volunteers [86]. In that study, 64 adjacent columns were sequentially sampled throughout both breasts to acquire spectra for a 2D chemical shift image from 4096 voxels in a scan time of 6.4 s. Although this is considered fast for 2D spectroscopic imaging, it is not sufficient for imaging the heart, where sub-second imaging may be required.

In the present work, the 2D spatial coverage was sacrificed to allow ultra-rapid, serial, 1D acquisitions. We tested whether data from each echo time in the gradient-echo train could be used individually to detect phase changes, allowing multiple temperature measurements in a single column acquisition. SNR properties were tested in vivo in a rabbit model, and feasibility in the context of cardiac imaging was tested in a healthy volunteer.

## 4.2 Materials and methods

### 4.2.1 Line scan echo planar spectroscopic imaging (LSEPSI) sequence

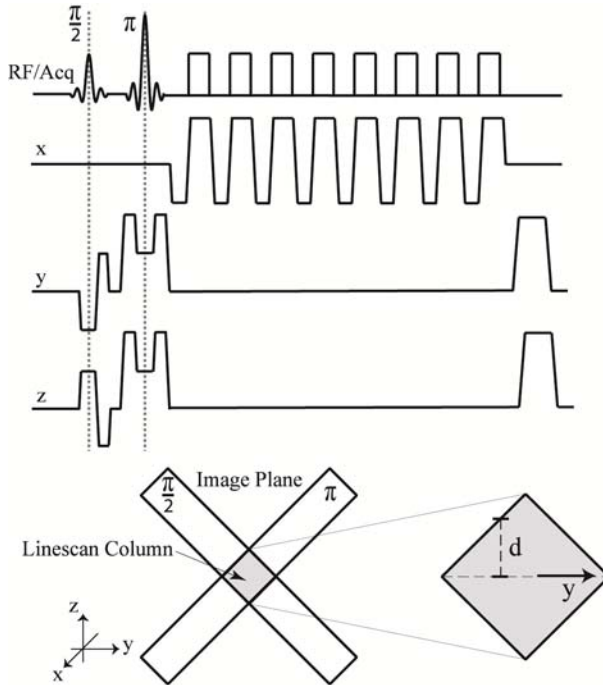


Figure 4-1: Diagram of an LSEPSI pulse sequence used to generate 1D temperature maps.  $90^\circ$  and  $180^\circ$  pulses were used to elicit a spin echo from a single column. Multiple gradient echoes were then generated using an echo planar readout. These echoes could be used separately for individual temperature measurements, or after FFT, to produce spectra to directly measure the water PRF. Bottom: The cross section of the imaged column has a diamond shape, and the indicated distance  $d$ , varying with  $y$ , was used as a weighting factor when comparing temperature measurements in ROIs from LSEPSI and SPGR data sets.

The LSEPSI sequence shown in Figure 4-1 and described in [86, 110, 111] was implemented on GE scanners (Milwaukee, WI) (3.0-T for rapid measurement experiments and 1.5-T for others). With this sequence, a selective  $90^\circ$  pulse and a selective  $180^\circ$  pulse were applied to intersecting slices, so that only the column located at the intersection of the two planes generates a spin echo signal. The second half of the spin-echo formed at  $TE = 10$  ms was sampled repeatedly, using an asymmetric (i.e., fly-back) echo-planar readout waveform. The inter-echo spacing in the echo-planar waveform was in the range from 2.1 to 3.7 ms, with different values used for different experiments. Additional image parameters of the LSEPSI sequence included the column sample rate (i.e., TR), field of view, slice thickness, number of frequency-encoding steps per gradient echo, and receiver bandwidth are listed in Table 4-1, for the various

experiments performed here. The spoiler gradients following the echo-planar readout train were modified from TR to TR, based on a 6 step phase cycling scheme (x, y, z, -x, -y, -z) to eliminate ghosting artifacts from indirect echoes [110].

	TR (ms)	slice thickness (mm)	ETL*	echo spacing **(ms)	FOV (cm)	matrix size	BW (kHz)
Sequence calibration	<b>2000</b>	<b>3</b>	<b>32</b>	<b>3.7</b>	<b>10</b>	<b>128×1</b>	<b>48</b>
Rapid monitoring	<b>53</b>	<b>4</b>	<b>8</b>	<b>3.3</b>	<b>16</b>	<b>128×1</b>	<b>48</b>
Rabbit Brain imaging	<b>15000/206</b>	<b>4</b>	<b>128/48</b>	<b>3.7</b>	<b>10</b>	<b>128×1</b>	<b>48</b>
Volunteer imaging	<b>200</b>	<b>5</b>	<b>32</b>	<b>2.1</b>	<b>32</b>	<b>128×1</b>	<b>64</b>

\*echo-train length

\*\*rounded to tenths

Table 4-1: LSEPSI sequence parameters used in the experiments.

The first half of the spin-echo was not sampled due to the design of the sequence, where the time between the 90° and 180° pulse was made as short as possible. As a result, there was essentially no time to sample data since the duration between the refocusing pulse and the spin echo was only enough to play the right element of the crusher pairs and the prephasing gradient lobe. In addition, the spin echo itself was not a good time to sample temperature information as all phase changes (including temperature-induced phase changes) were refocused, we effectively could only sample from the spin echo onward, i.e., the second half of the spin echo.

The effective echo time ( $TE_{\text{eff}}$ ) for the  $i^{\text{th}}$  gradient echo in the echo train is defined as the interval between the moment the spin-echo is formed and the center of the  $i^{\text{th}}$  gradient echo, where  $I$  ranges from 1 to the echo-train length. For example, the  $TE_{\text{eff}}$  of the very first echo ( $I = 1$ ) is 0, and the  $TE_{\text{eff}}$  of the  $i^{\text{th}}$  echo is  $(i-1) \times$  echo spacing. For

simplicity, the  $TE_{\text{eff}}$  of the LSEPSI sequence is represented by “TE” throughout this paper.

#### *4.2.2 Heating experiments*

All heating experiments were performed in a homogeneous gel phantom (ATS Laboratories, Bridgeport, CT, see reference [103] for its ultrasound properties). The experimental setup was described in Section 2.2.1. The phantom was placed in the sonication path of the transducer. Ultrasound propagated through the water and focused inside the phantom. A receive-only surface coil (GE Healthcare, Milwaukee, WI) with a diameter of 7.6 cm was positioned around the phantom at the level of the heating focus.

##### *4.2.2.1 Calibration experiments*

An array transducer described in Section 2.1 was used to generate an ultrasound field. It was operated in “mode 4” to create a wider focal zone (12×12mm) and reduced the effects of voxel averaging.

To ensure that the LSEPSI sequence correctly measured temperature changes, comparisons were made with a standard thermometry sequence. Dynamic 1D imaging using the LSEPSI sequence was performed over a 40-s period using a TR of 2-s, so that 20 echo trains (each consisting of 32 gradient echoes) were obtained. Heat was generated by a 20-s sonication with an acoustic power of 11 W. After a cooling period that allowed the temperature to return near baseline, another sonication with the same ultrasound parameters was delivered at the same location. A GE product 2D spoiled gradient-echo (SPGR) sequence was used to map the temperature changes [84] (FOV: 10×10 cm, TR/TE: 40/20 ms, matrix size: 256×128, flip angle: 30°, slice thickness: 3 mm, BW:

$\pm 3.57$  kHz , time frames: 10). For both sonications, a baseline image was acquired before the ultrasound was turned on. The calibration experiment was repeated at five different locations in the same phantom.

Because data were sampled at different spatial and temporal locations with the LSEPSI and the SPGR sequences, careful consideration was required when performing comparisons. Figure 4-2 shows how these two sequences were prescribed and how the ROI of the linescan was selected. Both the LSEPSI column and the SPGR image plane were perpendicular to the direction of the FUS beam, and the frequency encoding of both sequences were oriented in the same direction. In addition, the 1D column was prescribed to be enclosed by the 2D plane. The  $5 \times 1$  LSEPSI ROI was selected at the center of the column where the FUS beam passed through.

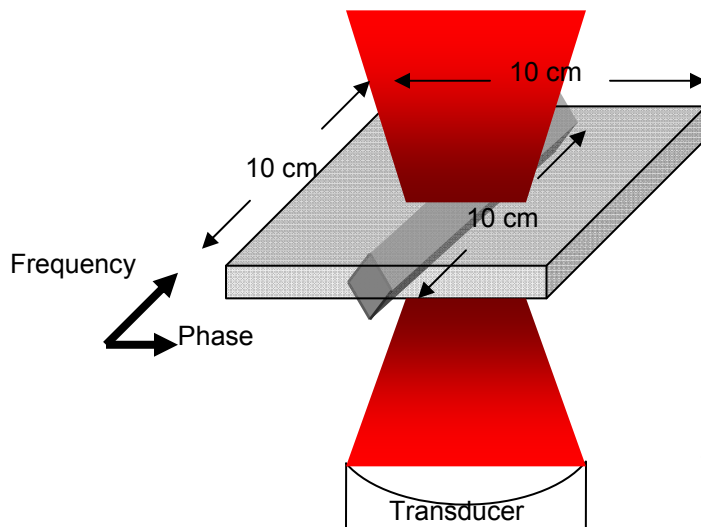


Figure 4-2: Imaging prescription for both SPGR and LSEPSI sequences. The in-plane resolution of the SPGR is  $256 \times 128$  while the in-column resolution of the LSEPSI is  $128 \times 1$ . A  $5 \times 1$  ROI was defined at the center of the 1D column along the frequency-encoding direction.

To compare LSEPSI measurements with SPGR, we needed to carefully map the LSEPSI diamond onto the SPGR imaging plane in the slice-phase plane. Figure 4-3 shows the cross section along the phase-encoding direction. In the phase-encoding direction, since the SPGR's spatial resolution was 0.78 mm, the LSEPSI diamond covered about 5 SPGR voxels from the left corner to the right corner. Each of the voxels corresponded to a distance  $d$ , which was used as a weighting factor when a weighted average was performed over the temperature measurements in those voxels. In the frequency-encoding direction, since the LSEPSI's spatial resolution (0.78mm) was twice as large as the SPGR's, 1 LSEPSI voxel contained 2 SPGR voxels. Overall, there were 10 SPGR voxels in 1 LSEPSI voxel and 50 SPGR voxels in the 5×1 LSEPSI's ROI. The weighted average over all 50 SPGR voxels was used to calibrate temperature measurement in LSEPSI's ROI.

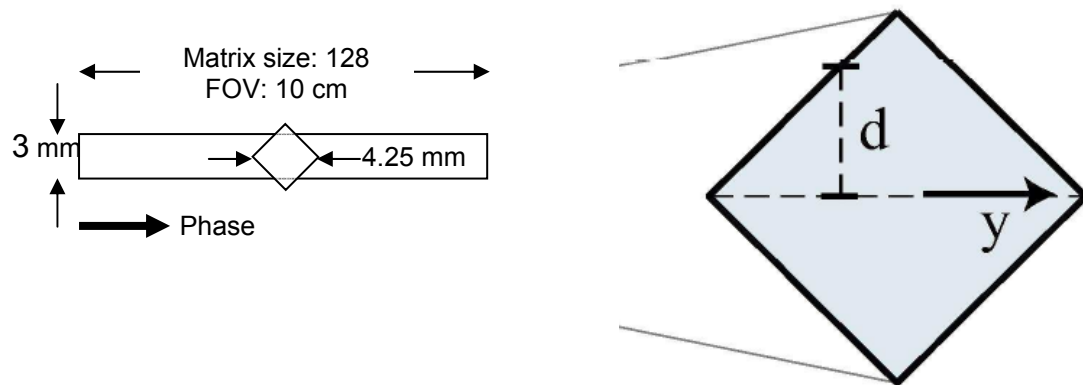


Figure 4-3: The cross section of the scan column superimposed on a 2D image, along the phase-encoding direction of Figure 4-2. The ROI of the LSEPSI was in the shape of a diamond. All SPGR voxels that mapped onto the diamond-shape ROI were scaled by a distance  $d$ . The phase change of the LSEPSI column in the ROI was then compared to the weighted average of the temperature changes within those mapping SPGR voxels.

Phase changes of all 32 echoes obtained from all 5 sonicated locations were then calibrated as a function of the temperature rises estimated from the SPGR temperature mapping. Least-square fitting was used to derive the temperature sensitivity of the LSEPSI sequence in radians/°C, as well as in ppm/°C as a function of the LSEPSI echo time.

#### 4.2.2.2 Rapid measurement experiments

A single-element transducer (refer to Section 2.1) was used to heat up the phantom. The temperature changes in the focus were sampled with the LSEPSI sequence at a column sample rate of 19 Hz (i.e., TR of 53 ms). Data were acquired continuously for 53 s while sonication with 32W acoustic power was delivered for 20 s. Images acquired 13 s before heating were used as baselines. The column was placed parallel to the ultrasound beam and through the focus. A 5×1 ROI in the focus was selected for temperature estimation. Temperature rises were estimated using 7 out of all 8 echoes, those with a TE greater than or equal to 3.3 ms. The temperature noise level was estimated using the standard deviation of the temperature changes over the time frames before FUS heating, in the same ROI.

#### 4.2.2.3 LSEPSI temperature estimation

Complex data were acquired to produce phase-difference maps. The phase difference between an image  $Z_t^i$  acquired from the  $i^{th}$  echo at time  $t$  and a pre-heating baseline  $Z_0^i$  was calculated by:

$$-\pi \leq \Delta\phi_t^i = \text{phase}(Z_t^i / Z_0^i) = \text{phase}(Z_t^i Z_0^{i*}) \leq \pi \quad (4-1)$$

where \* denotes complex conjugation. Temperature changes from one column acquisition to the next (i.e., from one TR to the next) were estimated by exploiting the temperature dependence of the PRF, which changes at a rate of  $-0.01$  ppm/ $^{\circ}\text{C}$ , or  $-0.64$  Hz/ $^{\circ}\text{C}$  at 1.5T, in water [84]. Changes in the PRF were estimated by dividing the phase difference by  $2\pi\text{TE}^i$  where  $\text{TE}^i$  was the  $i^{\text{th}}$  effective echo time.

Not all echoes were appropriate for temperature estimations, due to  $\text{SNR}_{\Delta\phi}$  considerations, which can be estimated as follows:

$$\text{SNR}_{\Delta\phi} = |\Delta\phi(\Delta T)| / \sigma_{\Delta\phi} \quad (4-2)$$

where  $\Delta\phi(\Delta T)$  is an echo's phase difference between the column at the current time and the column of baseline, and  $\sigma_{\Delta\phi}$  is the standard deviation of the phase-difference image, which can be approximated as [112]:

$$\sigma_{\Delta\phi} = 1 / \text{SNR} \quad \text{if } \text{SNR} \gg 1 \quad (4-3)$$

where  $\text{SNR} = A / \sigma$ , A is the magnitude signal, and  $\sigma$  is the Gaussian noise in a real or imaginary image. Eq. 4-2 then becomes:

$$\text{SNR}_{\Delta\phi} = |\Delta\phi(\Delta T)| \cdot \text{SNR} \quad (4-4)$$

As TE increases, SNR decreases exponentially with  $\text{T2}^*$ , yet  $\Delta\phi(\Delta T)$  increases linearly with TE. The TE dependence of  $\text{SNR}_{\Delta\phi}$  can be written as follows:

$$\text{SNR}_{\Delta\phi} \propto \text{TE} e^{-\text{TE} / \text{T2}^*} \quad (4-5)$$

Therefore, poor  $SNR_{\Delta\phi}$  is expected in early echoes due to their short TE values and possibly in some later echoes, depending upon the  $T2^*$ . Optimal  $SNR_{\Delta\phi}$  is expected at  $TE = T2^*$  [106]. Note that this analysis is true only for  $A \gg \sigma$ . However, for  $A/\sigma \geq 3$ , a fairly low SNR, it is still considered to be approximately true [112]. Image reconstruction, phase-difference calculations and data analysis were all performed in MATLAB (MathWorks, Natick, MA).

### **4.2.3 In vivo experiments**

#### **4.2.3.1 Rabbit brain imaging**

Our institution's animal committee approved the experiments. Based on Eq. 4-5, some early and later echoes might not be utilized for temperature measurements. To experimentally evaluate the  $SNR_{\Delta\phi}$  performance as a function of TE in vivo, non-heating experiments were performed in the brain of a male New Zealand white rabbit. The rabbit was placed supine in the MR-compatible FUS positioning system. A 7.5 cm diameter receive-only surface coil (GE Healthcare) was placed below the rabbit head at the level of the imaging column. LSEPSI imaging with  $TR = 15$  s was performed in a location in the thalamus. A total of 128 echoes ranging from 0 ms to 469.4 ms (echo spacing of 3.7 ms) were acquired during each TR period. Two acquisitions of a column, obtained in consecutive TR periods, were used to produce phase-change and temperature-change maps. To test the T1 saturation effect, a dynamic dataset of  $TR = 206$  ms was acquired in the same location with a total of 48 echoes ranging from 0 ms to 173.7 ms. After steady state was reached, two acquisitions were obtained sequentially to produce phase-change

and temperature-change maps. See Table 4-1 for other imaging parameters. Noise (standard deviation) in the phase-change map, as well as in the temperature-change map, for an ROI of  $4 \times 1$  voxels in size, was plotted as a function of the echo times.

#### 4.2.3.2 *Volunteer imaging*

Our institutional review board approved the imaging protocol and the volunteer provided written informed consent. To test whether spectroscopic temperature imaging in the heart was feasible with the proposed method, a 52 year-old male was imaged with a column sample rate of 5 Hz. A 2D chest image was first acquired during a breath hold by sweeping the columns stepwise across an image plane [110] (64 adjacent columns,  $32 \times 32$  cm FOV, 12.8 s scan time). The column through the heart muscle was selected for frequency mapping. A time series of 1D images were then acquired for a 40.0 s period. The images were acquired using a receive-only surface coil (GE Healthcare) with a diameter of 18.0 cm with a breath hold but without cardiac gating (echo spacing = 2.1 ms, spectral bandwidth =  $(2.1 \text{ ms})^{-1} = 476 \text{ Hz}$ , other imaging parameters in Table 4-1).  $SNR_{\Delta\phi}$  performance in the ROI of myocardium was evaluated in a manner similar to the rabbit brain experiments. Two consecutive time frames in the dynamic 1D dataset were taken to analyze the noise levels in the phase-change and temperature-change maps.

## 4.3 Results

### 4.3.1 Phase mapping

#### 4.3.1.1 Calibration experiments

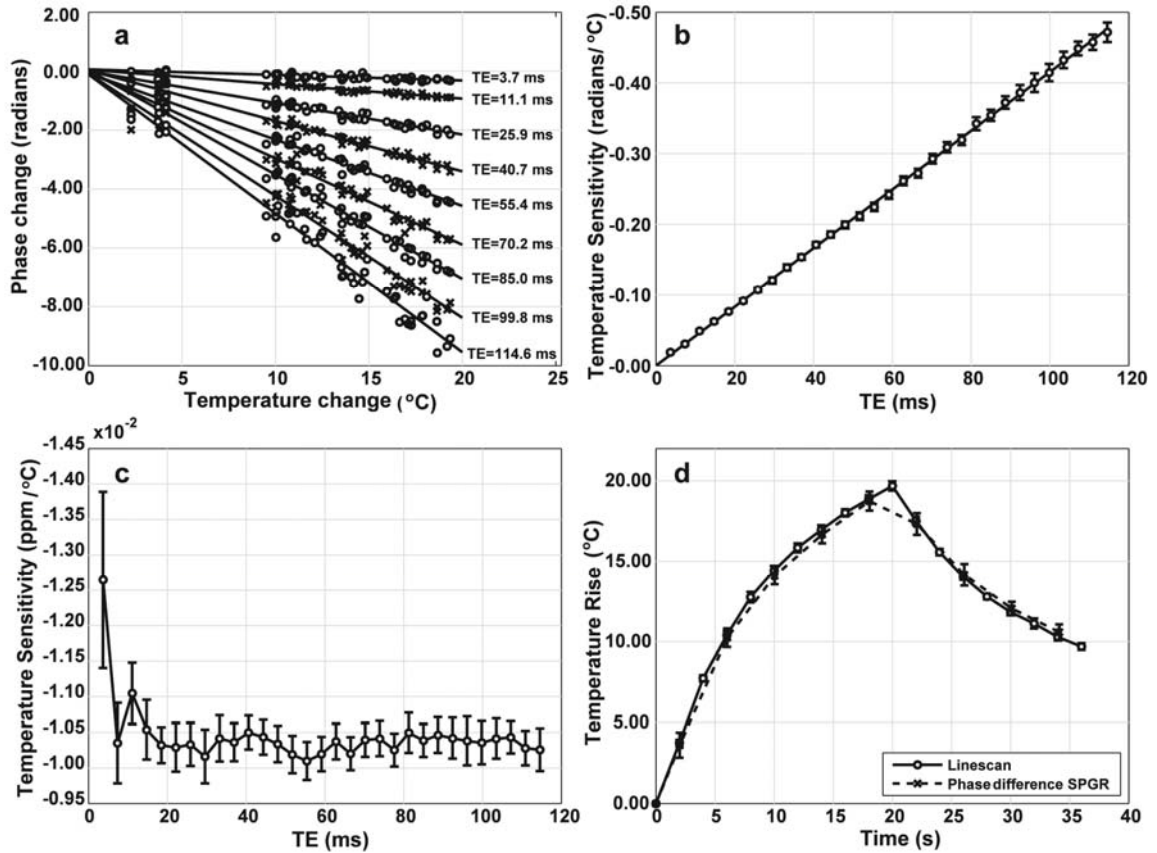


Figure 4-4: Results of LSEPSI calibration experiments. a) Plot of the phase change measured at the focus using the LSEPSI method as a function of the temperature rise measured using the standard method. Data for nine of the 32 echoes obtained in each TR are shown. Solid lines are linear regressions. b,c) Plot of the temperature sensitivity of the sequence as a function of the echo time for the 32 echoes obtained with each acquisition of the LSEPSI. b) sensitivity in radians/°C; c) sensitivity in ppm/°C. d) Comparison of the average temperature/time profile using the 1D LSEPSI approach with a standard sequence used for MRI-based thermometry (phase-difference SPGR imaging).

The temperature calibration results in the gel phantom are shown in Figure 4-4.

The correlation between the LSEPSI-measured phase changes for different echo times and the temperature as measured with the SPGR sequence are shown in Figure 4-4a. Data

from the first echo time ( $TE = 0$ ) were excluded since there is no expected phase change. For clarity, in Figure 4-4a, data for only nine out of the 31 echoes are shown. Good correlation was found through linear regression ( $R = 0.98 \pm 0.03$ ) for all echoes. Figure 4-4b shows the temperature sensitivity (radians/ $^{\circ}\text{C}$ ) obtained through the linear regression described above, as a function of TE. In other words, the slope of each line in Figure 4-4a gives rise to one point in Figure 4-4b (31 points for 31 echoes, 9 of which are actually displayed in Figure 4-4a). The standard errors estimated from the fits in Figure 4-4a are shown in Figure 4-4b as the error bars. The solid line represents a linear fit of the temperature sensitivity as a function of TE (slope:  $4.2 \times 10^{-3} \pm 1.4 \times 10^{-5}$  radians/ $^{\circ}\text{C}/\text{ms}$ , intercept:  $3.5 \times 10^{-5} \pm 9.4 \times 10^{-4}$  radians/ $^{\circ}\text{C}$ ). This result shows that the temperature-induced phase changes scale linearly as expected with the TE setting, and that the sensitivity extrapolates to zero with a zero TE. The temperature sensitivity in ppm/ $^{\circ}\text{C}$  as a function of TE is plotted in Figure 4-4c. Most of the values were consistent between -0.0100 and -0.0105 ppm/ $^{\circ}\text{C}$ , except the TE values ranging from 3.7 ms to 14.8 ms. This discrepancy is not surprising due to the low expected  $SNR_{\Delta\phi}$  (Eq. 4-5) obtained for a short TE value. The average value was  $-0.0103 \pm 0.0004$  ppm/ $^{\circ}\text{C}$ , in good agreement with the generally-accepted -0.01 ppm/ $^{\circ}\text{C}$  value for pure water [78]. In Figure 4-4d, temperature-change measurements at the focus are compared for our proposed method ('o' markers in the solid line) and for the reference SPGR sequence ('x' markers in the dashed line). Temperature curves from all 5 sonicated locations were averaged. For the LSEPSI results (solid line), data from all echoes were averaged with a weighted combination, where weights were derived based on the expected  $SNR_{\Delta\phi}$  in Eq. 4-5 ( $T2^*$  value of the gel

phantom = 111 ms). Good agreement was observed between the LSEPSI and reference sequence.

#### 4.3.1.2 Rapid measurement experiments

Focal heating along the ultrasound beam was quantified using phase mapping at a column sample rate of 19 Hz (i.e., TR = 53 ms). A weighted combination of echoes  $\geq 3.3$  ms, based on the expected  $SNR_{\Delta\phi}$  of each echo, was used to illustrate inter-TR temperature mapping. Figure 4-5b shows the time series of the one-dimensional temperature mapping during FUS heating and cooling periods. The vertical dimension represents the along-column spatial dimension and the horizontal dimension represents time. It suffers from high temperature noise due to the high temporal resolution. Figure 4-5a shows a time series of magnitude images from 5 to 10s, where signal voids around the center, caused by a small hole in the gel phantom, might account for the horizontal artifacts in Figure 4-5b. The maximum heating was observed at 33 s, which is when the transducer was turned off. Figure 4-5c shows the temperature rise over time from the ROI at the focus. Seven out of eight echoes were utilized for temperature measurements, which are displayed in different colors in Figure 4-5c. In total, 6993 measurements were achieved in 53 s (7 echoes per TR period  $\times$  999 TR periods = 6993 echoes). The noise levels were 2.4 and 1.5°C for the first two echoes (TE values of 3.3 and 6.5 ms), and  $0.8\pm 0.1^\circ\text{C}$  for the rest of the echoes (TE values of 9.8 ms or greater).

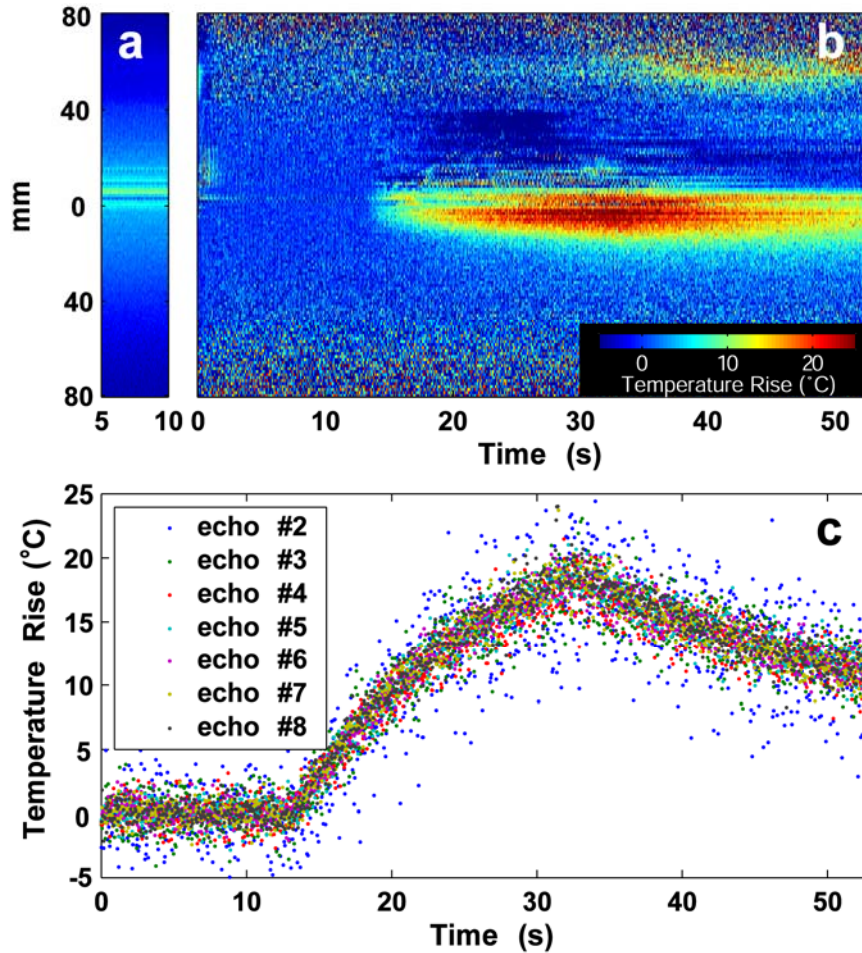


Figure 4-5: The time evolution of the 1D LSEPSI images and the temperature changes in the focus. a) A time series of 1D magnitude images in baseline (5 to 10s). Signal voids near the center of the columns might account for the horizontal artifacts in temperature mapping. b) Images showing 1D temperature measurements during a 20s sonication in a phantom. This "M-mode" MRI shows the temperature evolution as a function of time. c) Plot of temperature rise vs. time at the focus during the sonication. By using 7 out of 8 acquired echoes in TR of 53 ms,  $7 \times 999 = 6993$  temperature measurements could be made over a 53 s period (1000 time frames), with a noise level below  $1^\circ\text{C}$  for echoes greater than 9.8 ms. Measurements from different echoes were distinguished by colors.

#### 4.3.1.3 Rabbit brain imaging

Data of  $TR = 15$  s were analyzed in Figure 4-6a,b. Figure 4-6a plots the noise level in the temperature maps of a non-heated ROI in the rabbit brain, as a function of the TE value. Figure 4-6a is used to determine the lowest value of TE that should be utilized for the temperature measurement. For 127 echo times ranging from 3.7 ms to 469.4 ms, the temperature noise level settled down to a level of about  $0.5^{\circ}\text{C}$  for TE values greater than about 50 ms. Figure 4-6b plots the noise level in the phase-change maps and is used to determine the highest value of TE. The phase noise is theoretically a good surrogate for the reciprocal of the SNR, as long as the mean signal in the magnitude images divided by the noise level in the real and imaginary images gives a number larger than 3 [112]. For echo times larger than 200 ms, phase noise rose above 0.3 radians, and SNR dropped below 3. This suggests that TEs larger than 200 ms should be discarded for the temperature measurement. From the analysis of Figure 4-6a,b, TEs between 50 and 200 ms could be utilized for thermometry and noise of  $0.5^{\circ}\text{C}$  is expected.

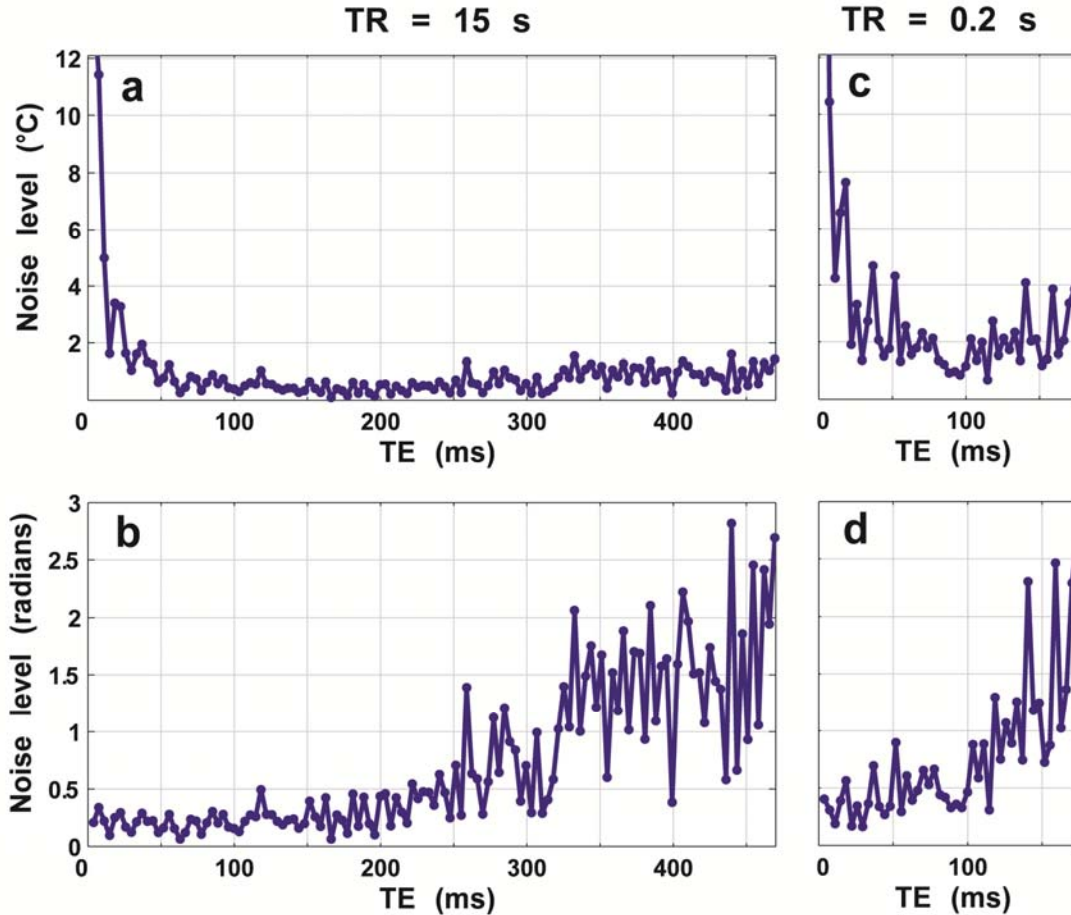


Figure 4-6: Noise levels in °C and radians for two TR datasets. a,c) Standard deviations in the temperature maps of a non-heated ROI in the rabbit brain as a function of the echo time for TR = 15 and 0.2 s. After about 50 ms, both noise levels settle down to steady values b,d) Noise levels in the phase-difference images, in radians, for TR = 15 and 0.2 s. The noise represents the reciprocal of the signal-to-noise ratio (SNR) as long as the SNR remains larger

The same analysis was performed using data of TR = 206 ms in Figure 4-6c,d. TEs between 50 ms and 100 ms could be utilized for the temperature measurement and a noise level of 2°C is expected. Please note that the temperature noises in Figure 4-6a,c (for TR=15 s and 206 ms, respectively) decay at about the same rate; both curves reach a steady value around 50 ms. This is reasonable because T2\* was the same on both measurements. It is also reasonable that the temperature noise in Figure 4-6c for the data

with  $TR = 206$  ms is higher than the data with 15 s in Figure 4-6d, due to signal saturation. The comparison between datasets with long and short TR suggests that the lower limit of TE is independent of TR, and further suggests temperature noise and the lower limit of TE are determined by SNR.

### *4.3.2 Frequency mapping*

#### *4.3.2.1 Volunteer imaging*

An axial chest image using 2D LSEPSI imaging is inset in Figure 4-7a. Each vertical line in the image was obtained sequentially, in an interleaved pattern. The periodic artifact from column to column and the artifact at the bottom of the heart were caused by cardiac motion. Figure 4-7a shows a spectrum from one voxel located in the heart muscle in the inset image, where a water spectral peak can be observed. Note that it was possible to measure the PRF in a beating heart muscle, during breath hold. One line location over the heart was selected, and imaged 200 times over a 40 s period (i.e.,  $TR = 200$  ms), with 32 gradient-echoes acquired during every TR period. Figure 4-7b shows the signal intensity from the first echo in the echo train, for a voxel located in the heart muscle. Figure 4-7c gives the FFT of the signal in Figure 4-7b.

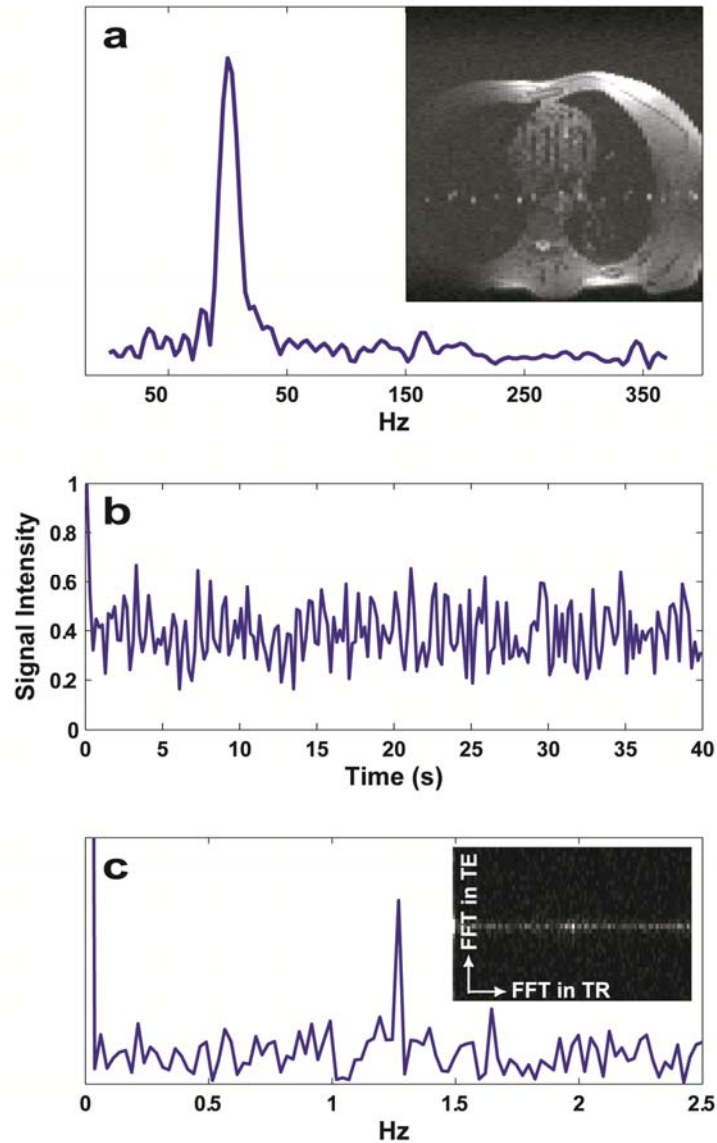


Figure 4-7: Spectroscopic analysis along TE and TR dimensions from cardiac images. a) Single-line data from the heart muscle of a volunteer showing the water spectral peak. The spectrum was generated through a (zero-filled) FFT of 32 echoes acquired during a single TR interval. The same column was acquired repeatedly at a sample rate of 5 Hz (i.e., TR = 200 ms) over a 40 s period. Inset: Breath-hold 2D LSEPSI image of a volunteer showing the heart (18-cm receive-only surface coil, no cardiac gating). b) Magnitude signal from one given echo in the gradient-echo train, sampled  $5 \times 40 = 200$  times over a 40 s period, from a location in the heart muscle of a volunteer. Periodic fluctuations were observed. c) FFT of this data yields a heart rate of 1.3 Hz. Inset: A 2D spectrum from a dataset of  $32 \text{ echoes} \times 200 \text{ column acquisitions}$ , i.e., 2D FFT along TE and TR dimensions. The center peak represents both water frequency and heart pulsation rate.

It is interesting to notice that an FFT over all 32 gradient-echoes in a given TR (Figure 4-7a) gives very different information than an FFT over all 200 TR periods for a given echo (Figure 4-7c). Indeed, the acquired series of 1D images feature two very different temporal dimensions: one as a function of TE, and one as a function of TR. The high sampling rate obtained with a 2.1 ms echo spacing makes it possible to get spectral results that allow the PRF location to be measured (FFT along TE for a given TR, Figure 4-7a). In contrast, an FFT along TR for a fixed TE value (Figure 4-7c) yields a spectrum that captures the heart pulsation frequency, 1.3 Hz here. A 2D FFT over the dataset of 32 echoes  $\times$  200 time frames is shown in inset of Figure 4-7c, where vertical dimension represents the spectrum along TE periods while horizontal dimension represents the spectrum along TR periods. The center peak indicates that both heart pulsation rate and water PRF were retrieved.

The noise levels of both phase and temperature maps from two column acquisitions over the ROI of myocardium were analyzed. With a total of 32 echoes in 200 ms TR, the 15<sup>th</sup> to the 32<sup>nd</sup> echoes ranging from 30 to 66 ms could be used for measuring temperature, where the temperature noise of  $1.4 \pm 0.6^\circ\text{C}$  is expected.

## 4.4 Discussion and conclusions

It has been shown that ultrafast MR temperature measurement using the LSEPSI sequence is feasible. Each echo in the acquisition can be used as separate temperature measurements via phase mapping, although earlier and later echoes might not be useful for temperature-mapping purposes, due to high temperature noise. Phase changes of each echo in the echo train were calibrated so they could be converted into temperature changes. In one of the phantom experiments, 7 echoes out of the acquired 8 echoes were used with a sample rate of 19 Hz; i.e., 7 measurements were achieved every 53 ms. The signal from each one of these 7 echoes could be converted into a temperature curve with 53 ms resolution, and combining information from all 7 curves gives temperature-change results with uneven temporal resolution (resolution = echo spacing  $\approx$  3 ms during the echo train, with gaps about 30 ms wide in between echo trains). The acquired cardiac data showed that spectral information could be obtained from the gradient echo train, allowing the PRF to be measured every TR.

In an alternative processing, one might be able to reconstruct all echoes in one step, rather than using different baseline data for each. However, the relationship between temperature change and phase would no longer be linear. For example, if one assumes that the temperature change  $\Delta T$  over the very short echo train period is linear, the phase change  $\Delta\phi$  could then be estimated as a parabolic function of TE according to:

$$\Delta\phi = \alpha \cdot \gamma \cdot B_0 \cdot 2\pi \cdot \int_0^{TE} \Delta T dt, \text{ where } \Delta T = at + b \text{ (} a, b \text{ are both constants)} \quad (4-6)$$

where  $\alpha$  is the apparent PRF-thermal coefficient (units of ppm/°C),  $\gamma$  is the gyromagnetic ratio for the  $^1\text{H}$  nucleus,  $B_0$  is the main magnetic field strength, and TE is the effective echo time. Temporal resolution can then be further improved to the level of echo spacing (a few ms). It is very challenging to validate the parabolic phase change relation in Eq. 4-6, due to the fact that the temperature-induced phase change over two immediate TEs is small and often overwhelmed by noise. The noise over the echo train (from the 1<sup>st</sup> echo to the 8<sup>th</sup> echo) can be estimated by examining the non-heating baseline frames. For a given voxel in a given baseline frame, the absolute phase value increased over the time course of the echo train, and a slope can be obtained from linear fitting to those phase values. Over all baselines, the standard deviation of those slopes gave the noise in radians/s. For a voxel in the focus, a noise of 10 radians/s was obtained, which gave rise to a temperature noise of 1.24°C. This is the temperature noise within the echo train. However, in the rapid heating experiment, the temperature change within the echo train was only about 0.04°C (There was 30°C change in 20 s and 19 frames per second. And the echo train length was about one half of the time frame. Therefore,  $(30^\circ\text{C}) / (20 \text{ s}) / (19 \text{ frame/s}) / 2 = 0.04^\circ\text{C}$ ). The temperature noise of 1.24°C was much larger than the expected temperature change of 0.04°C. Thus, with the setting in the rapid heating experiment, we could not possibly measure the temperature change within the echo train.

It might still be possible to validate the temperature change over the train echo. One way is to increase temperature change by high-power heating source. Heating by several degrees Celsius within a sub-second period could provide measurable phase changes. Lasers, for instance, make such rapid heating possible. For a 5°C increase in

200 ms within a  $5 \times 5 \times 5 = 125 \text{ mm}^3$  volume in water gel phantom, we need a power of 13 W (specific heat capacity of water =  $4.186 \text{ joule/gram/}^\circ\text{C}$ ). Modern laser systems for thermal ablation can easily achieve this. For example, the LITT Brain system, developed by Visualase (Houston, Texas), delivers up to 30 W. Another way is to reduce the temperature noise by averaging repeated trials. For example in the rapid heating experiment, at least 1,000 repetition is required to reduce the temperature noise of  $1.24^\circ\text{C}$  below the expected temperature change of  $0.04^\circ\text{C}$  so the small change could be detected (SNR is proportional to square root of average:  $(1.24/0.04)^2 = 961$ ). It is certainly not a practical mean for the FUS setting in the rapid experiment. However, it might be useful when the power of heating source is high but not high enough to overcome the estimated noise.

The LSEPSI sequence provided a simple way to accelerate MR thermometry imaging as compared to echo-planar imaging (EPI). Modern parallel single-shot EPI sequences could achieve temporal and spatial resolutions comparable to the LSEPSI sequence that was implemented with sampling time of 53ms. However, the coil sensitivity encoding introduces noise enhancement and image artifacts. It also increases significantly the amount of computing time in post processing. In addition, EPI often suffers from distortions, signal voids, and ghosting. Distortion can be a considerable concern in the context of thermal ablation, as lesions must be located and tracked accurately. One can of course mitigate the distortion by shortening the echo-train length, for example by using interleaved EPI, or reducing the number of echoes, but there are always tradeoffs that compromise either temporal or spatial resolutions.

The advantage of an EPI sequence vs. the LSEPSI sequence is its 2D spatial coverage. However, while an EPI sequence provides better spatial coverage, the proposed technique provides better spectral coverage. Please note that the proposed method features a readout waveform very similar to that of an EPI sequence, and is just as efficient in terms of data acquisition rate. The main difference is that EPI has  $y$ -gradient blips in order to encode a second spatial frequency dimension in addition to the frequency-encoded dimension, while LSEPSI has no blips and covers one spatial dimension (frequency-encoded) and one spectral dimension. It is a trade-off for the purpose of ultra-fast thermometry. LSEPSI makes it possible to measure temperature via phase changes from TE to TE. It also makes it possible to measure temperature spectroscopically from TR to TR. Neither of these options is possible with a standard EPI. Concerning 2D spatial coverage, the present method could achieve it by sweeping columns through the desired ROI [111], although this comes with a price of reduced temporal resolution. Parallel imaging has also been applied to linescan sequences to increase scan efficiency [113] when more spatial coverage is necessary.

The spatial resolution of the present method is not as good as a regular 2D sequence, which could result in a partial volume effect in MR temperature imaging. However, LSEPSI could achieve a reasonable voxel size for thermal ablation applications. For example, the InSightec ExAblate 4000 TcMRgFUS system has a half-width-full-maximum focal region of about  $3.0 \times 3.0 \times 5.8$  mm, as provided by the manufacturer, so a resolution of 3.0 mm could therefore be considered reasonable. Column selection is performed through two intersecting RF-excitation profiles and a slice thickness of 3.0

mm is readily achievable. LSEPSI has been implemented with an even better resolution down to 1.5 mm (data not shown). Therefore, the partial volume effect can be avoided. In the case of a very small focus region, this method might not be applicable. High temporal resolution and high spatial resolution inevitably result in very low SNR, a problem shared by all MR imaging techniques.

In the calibration experiment, temperature changes over heating and cooling periods were compared between the LSEPSI sequence and a SPGR reference sequence (Figure 4-4d). Both measurements appeared to agree well, except for the peak temperature at 20 s. We suspect this might have been caused by the lower temporal resolution of the reference SPGR data, which were too low to accurately catch the peak temperature.

A study by Peters and Henkelman [88] showed that temperature-induced changes in electrical conductivity of the imaging object could result in phase-shift offsets in temperature sensitivity vs. TE, i.e., a non-zero intercept. A phase offset as large as  $-0.33$   $^{\circ}\text{C}$  was reported under certain experimental conditions. However, as seen in Figure 4-4b, we did not observe this effect (phase offset in our study:  $0.002$   $^{\circ}\text{C}$ ). As suggested in the paper, it was most likely because the heating source in our study was relatively small, as opposed to other calibration experiments [80] where heating occurred in large volumes. It was also possibly because the changes in electrical conductivity in our phantom were small, although this needs further investigation.

The temperature column mapping along time in Figure 4-5b does not show high image quality. This is mainly due to the high column sampling rate, which results in T1

saturation, and therefore images feature low SNR and high temperature noise. A possible way to tackle the issue is with FLASE [114], where flip angles larger than  $90^\circ$  are used to reduce T1 saturation for spin-echo sequences.

Accuracy of LSEPSI temperature measurements depends upon the phase-difference SNR,  $SNR_{\Delta\phi}$ , of the echo setting, which should be predetermined for different tissues before implementation of heating experiments. In the case when  $T2^*$  is known,  $SNR_{\Delta\phi}$  can be approximated with Eq. 4-5 and therefore TEs with acceptable noise levels could be derived. Otherwise, a non-heating experiment as done in rabbit brain followed by analysis of noise levels in both  $^\circ\text{C}$  and radians could help determine the appropriate echo setting. For some sampling rates, e.g., 20 Hz in the rapid measurement experiments, almost all echoes could be included in the echo setting and be utilized for temperature measurement. For others, the later echoes in the echo train might be discarded, which results in increased dead time without measurements, and decreased efficiency. This could be overcome by reducing readout bandwidth and performing complex average over these later echoes, and therefore most echoes could be used for temperature measurements.

The method is insensitive to motion outside of the column, potentially allowing for applications in the heart, such as for monitoring during thermal generation of transmural myocardial lesions for the treatment of tachyarrhythmias. Measurements of the water frequency in the heart were encouraging, indicating that a gating or triggering of the sequence could allow for stable measurements to permit temperature measurements via phase changes with adequate accuracy for monitoring thermal ablation.

We have demonstrated an ultrafast method for monitoring frequency or phase changes along selected columns, allowing for inter-TR temperature change estimates. With temporal resolution on the level of 50 ms, it may be possible to monitor the focal heating produced by short (less than one second) ultrasound pulses, such as thermal ablation in the heart.

## 5 Summary

A review of recent literature reveals that the temperature mapping based on water proton resonance frequency (PRF) shift has found general acceptance for use in magnetic resonance (MR) guided focused ultrasound (FUS) therapy. Ideally, the MR thermometry method provides both high temporal and spatial resolution to precisely monitor the temperature distribution within the targeted tissue. The temperature update time with standard MR methods, however, has impeded the therapy's acceptance for clinical applications that require high temporal resolution, such as thermal ablation in areas that are subject to motion or treatment with ultra short FUS exposure. The research reported in this thesis has aimed to further investigate MR thermometry techniques as to their ability to provide a fast and reliable tool for MR-guided FUS (MRgFUS) therapy.

In the first project, we demonstrated that a hybrid technique could be used to accelerate the thermometry used clinically for MRgFUS therapy. Analysis in the repeated experimental trials confirmed that the accelerated method was a rapid alternative to the conventional technique. Three existing fast imaging strategies were found well-suited for monitoring temperature distribution in the volume heated by FUS. A volume-selective 2DRF excitation pulse joined forces with a multi-coil technology (parallel imaging) and a well-established temporal strategy (UNFOLD) to speed up acquisition for temperature mapping. Temperature imaging was accelerated by as high as 24-fold compared to the clinically used 2D thermometry sequence in experiments with a tissue-mimicking phantom and an ex-vivo tissue heated by FUS. The temporal resolution achieved was

about 300 millisecond. Results were compared to those obtained from the clinical thermometry and a good agreement was observed ( $0.1^{\circ}\text{C} \pm 0.6$ ;  $R = 0.98$ ).

Later experiment demonstrated the implementation of the hybrid method in a 3D sequence. It helped to develop a framework, which facilitates the choice of acquisition parameters to achieve the optimal compromise especially for the situation when SNR is limited. It was also demonstrated that the accelerated sequence was able to perform in real time, through the successful integration of MR scanner, a real-time reconstruction host, and a real-time display system.

The reliability of the hybrid method, in terms of the reduction of the temperature error caused by the presence of lipids, was established in experiments using adipose phantoms. A specific 2DRF pulse was designed to spatially vary fat-water excitation so as to remove the fat signal from the ROI. Its effectiveness with respect to the fat cancelation was confirmed in a water-oil phantom. The temperature measurements of the modified hybrid method in cheese heating experiments showed that such method was capable of reducing the error from fat.

The hybrid method, in the first project, aimed to accelerate the clinical thermometry based on a GRE sequence. The FUS heating experiments in an ex-vivo human skull demonstrated that the hybrid technique could also be used to give an extra acceleration to a commonly-used fast MRI sequences, EPI. An accelerated EPI sequence was implemented for 3D imaging and temporal resolution of less than 1 s was achieved for spatial coverage of the whole skull.

The acceleration factor of the hybrid method is restricted by the ability of designing a practical 2DRF pulse to excite a very thin stripe. With the use of a novel sequence in which a single 1D column could be excited, the limit of temporal resolution for MR thermometry was investigated.

In the second project, we demonstrated that a temporal resolution in the range of 50 to 200 millisecond could be achieved for thermometry with a novel 1D spectroscopic sequence. The 1D column excitation was achieved via a slice selective  $90^\circ$ - $180^\circ$  pair of RF pulses and then sampled with a train of gradient echoes. Since only a 1D line is excited, no phase-encoding is required, and the temporal resolution of this sequence is its repetition time (TR). In a tissue-mimicking phantom, phase changes of each echo were correlated to clinical thermometry, and temperature monitoring was tested during focused ultrasound sonications. A good correlation ( $R=0.98\pm 0.03$ ) was found and showed that each echo in the readout train could be used for temperature measurements, i.e., multiple measurements could be obtained within temporal resolution of one TR. The limit of temporal resolution was tested in a rapid heating experiment at a 3-Tesla scanner. Measuring temperature changes from echo to echo ( $\sim 3.6$  millisecond) was not possible for the FUS setting in the heating experiment, due to the high temperature noise and low temperature change within the echo train. However, averaging measurements in repeated experimental trials (reducing temperature noise) and/or elevating the deposit power (increasing temperature change) could make the phase change measurable.

The rabbit brain experiment demonstrated how to evaluate the imaging parameters for the 1D thermometry and make the best choice before an in-vivo heating

experiment is conducted. The volunteer experiment showed that it is feasible to measure temperature change in a beating heart with the 1D approach.

The techniques investigated in this thesis offer temporal resolution higher than any other fast MR thermometry reported, which might promote the acceptance in MRgFUS therapy for applications during rapid ultrasound exposure in mobile organs.

## **6 Appendix A: The implementation of the hybrid method in an adipose phantom**

### **6.1 Introduction**

MR thermometry using the PRF-shift method can be corrupted by the presence of fat, due to the fact that the lipid resonance frequency is almost temperature-independent [5]. In voxels containing both fat and water, the MR signal consists of the complex sum of water and fat signal, each one with its own magnitude and phase. In such voxels, the temperature-induced phase changes to the water signal are essentially obscured by the temperature-independent fat signal, leading to errors in temperature measurements [10]. Another difficulty in PRF-shift thermometry is its long scan time, due to the long TE values used (TE is required to be comparable with  $T_2^*$  to increase temperature-to-noise-ratio [106]). As a consequence, achieving accurate temperature measurements with good temporal resolution in the presence of fat can be considered a very challenging task. In a previous study, 2DRF pulses have been proposed to address both fat-suppression and fast-imaging needs encountered in PRF-shift MR thermometry applications [67, 74, 84]. In the present study, a 2DRF pulse was combined with UNFOLD and parallel imaging to create a hybrid method, enabling fast imaging and/or 3D coverage, in addition to accurate temperature measurements in fatty tissue. For the hybrid method in 2D sequence, the scan efficiency was improved by eight-fold in terms of temporal resolution. For the hybrid method in 3D sequence the scan efficiency was improved by eight-fold in terms of through-plane volume coverage.

## 6.2 Materials and methods

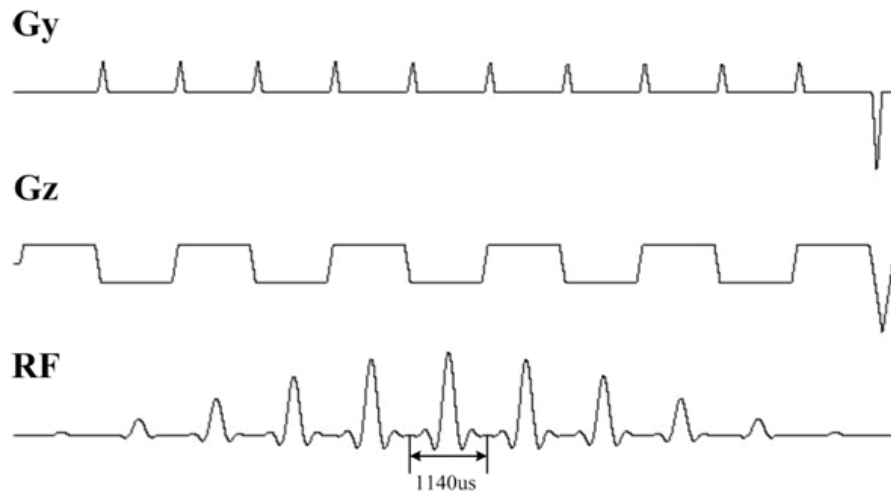


Figure 6-1: The waveform of the echo-planar 2DRF pulse used for fat suppression and rFOV imaging. The 2DRF pulse consists of 11 sinc sub-pulses and the sub-pulse duration is 1140  $\mu$ s. The amplitude of the sub-pulses is modulated by a Gaussian envelope.

A total of 11 sub-pulses, each with 1140  $\mu$ s pulse width and modulated with a Gaussian envelope, were used for the 2DRF pulse (Figure 6-1). Total duration of the pulse was 12.5 ms. Such RF pulse can spatially vary fat-water excitation by exploiting the strong chemical-shift sensitivity of the 2DRF in the phase-encoding direction [115], in addition to generating transverse magnetization within stripe shaped excitation patterns in two dimensions. The 2DRF excitation profiles due to this pulse were examined on a GE Excite Signa 3-Telsta scanner (GE Healthcare, Milwaukee, WI) with a fat-water phantom consisting of vegetable oil and water. Figure 6-2a is the reference image produced by the original 2D gradient-echo sequence with a normal slice-selective RF pulse. Figure 6-2b shows the 2DRF excitation profile, where the excitations are restricted to narrow stripes both in the fat and water although the location of the stripes varies for

fat and water due to their different resonant frequencies. In the center of the FOV, only the water was excited whereas the fat in this region was suppressed. At the side of the FOV, on the other hand, only the fat was excited and the water in these regions was suppressed.

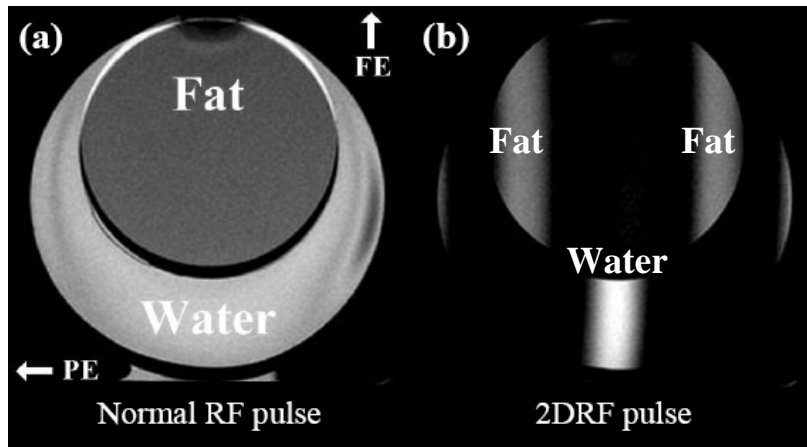


Figure 6-2: Excitation profile in a water-oil phantom. a) Fat-water phantom imaged using a normal RF Pulse. PE and FE denote phase and frequency-encoding directions, respectively. b) Excitation profiles for the  $11 \times 1140 \mu\text{s}$  2DRF pulse, where fat and water are excited at varied locations.

This 2DRF pulse was played out in a cheese phantom with homogeneous mixture of fat and water (Original Velveeta, 21% fat, Kraft Foods Inc., Northfield, IL). The excitation profile imaged in the cheese phantom is shown in Figure 6-3. Only lipid signal was excited at the edges of the FOV by the 2DRF pulse, while only aqueous signal was excited in the central region. The distance between fat and water lobes in this case ( $1/4$  FOV) is multiple of the chosen rFOV size ( $1/8$  FOV) so that in rFOV images the excited fat at the FOV edges and some water will wrap around on top of the water signal in the central region. This wrapping (or aliasing) is then removed by parallel imaging [100] and UNFOLD [95] as described in detail in Section 3.2.

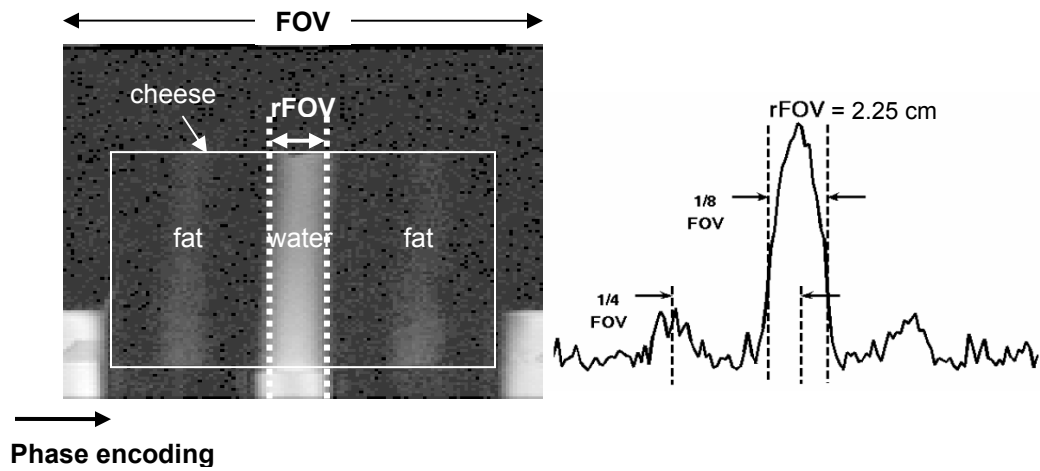


Figure 6-3: Excitation profile in a cheese phantom. *Left:* MR image of a cheese phantom using proposed 2DRF pulses. Fat was suppressed in the central striped region (lobe), while water was suppressed in the side lobes. Signals outside these lobes were fully suppressed by the 2DRF pulse. *Right:* Relative signal intensity in the phase-encoding direction. The distance between side lobes (fat) and center lobe (water) is a multiple of rFOV size (2.25 cm). In rFOV imaging, aliasing could be removed by paralleling and UNFOLD.

GE product 2D and 3D spoiled gradient-echo (SPGR) sequences were modified to incorporate the hybrid method. A single-element transducer (diameter: 10 cm, radius of curvature: 10 cm, frequency: 1.5 MHz) described in Section 2.1 was used to generate ultrasound fields. The cheese phantom was sonicated for 30 sec with acoustic power of 4 W and 2D rFOV images with the proposed 2DRF pulse (i.e., fat-suppressed and accelerated) were acquired during heating and cooling. The following scan parameters were used for the single-slice, 2DRF, rFOV imaging: TE/TR: 9.2/30 ms, flip angle: 23°, BW:  $\pm 15.6$  kHz, matrix size: 16 $\times$ 128, FOV: 2.25 $\times$ 18 cm, and slice thickness: 3 mm. Full FOV images (18 cm) with the same 2DRF pulse (i.e., fat-suppressed but not accelerated) and a conventional 2D thermometry (i.e., neither fat-suppressed nor accelerated) were also acquired for comparison. Imaging with the 3D rFOV sequence was performed in the

cheese phantom, which was heated for 30 sec with FUS (acoustic power: 16 W). The 3D rFOV images were acquired during heating and cooling (TE/TR: 9.2/30 ms, flip angle: 23°, BW:  $\pm 15.6$  kHz, matrix: 16 $\times$ 128, FOV: 1.25 $\times$ 10 cm, slice number: 8, and slice thickness: 5 mm).

The data acquired with the modified 2D/3D SPGR sequences were reconstructed using SENSE and UNFOLD. The phase images of all experiments were used for generating temperature maps. Detailed description of image reconstruction is depicted in Section 3.3.7.

### 6.3 Results

Results from the cheese phantom heating experiment, with a 2D eight-fold accelerated sequence, are shown in Figure 6-4 and Figure 6-5. Temporal resolution of the accelerated sequence was 480 ms. Since the accelerated results featured high temporal resolution, leading to high noise levels, temporal averaging over a sliding window of eight time frames was performed on the data shown in Figure 6-4 and Figure 6-5, to make the temporal resolution comparable to that of the non-accelerated reference. A temperature map for the time frame with maximum heating is shown in Figure 6-4. The noise on the sides parallel to the FUS beam is due to the excitation tails of water lobe (Gaussian), as smaller signal magnitude leads to higher phase/temperature SNR. Temperature changes for a  $3 \times 3$  ROI within the focus of heating are plotted in Figure 6-5. The discrepancy between the conventional sequence (magenta) and the non-accelerated fat-suppressed sequence (blue) shows how the presence of fat corrupts results when using a sequence without fat suppression. The accelerated fat-suppressed sequence (green) shows heating results similar to the non-accelerated fat-suppressed case.

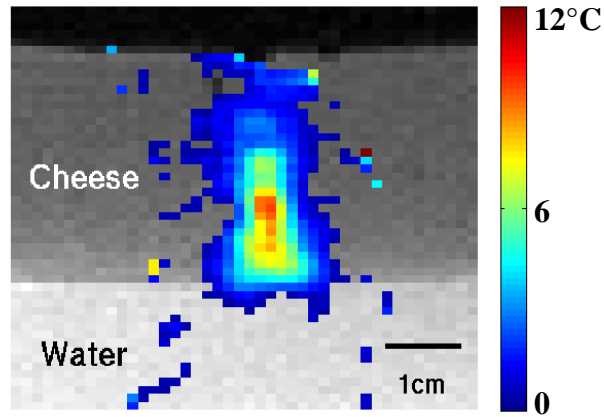


Figure 6-4: The temperature map of the time frame with the maximum heating in a cheese experiment. It was obtained from accelerated fat-suppressed sequence. Spatial average of 9 voxels and temporal average of 8 frames were performed for the map.

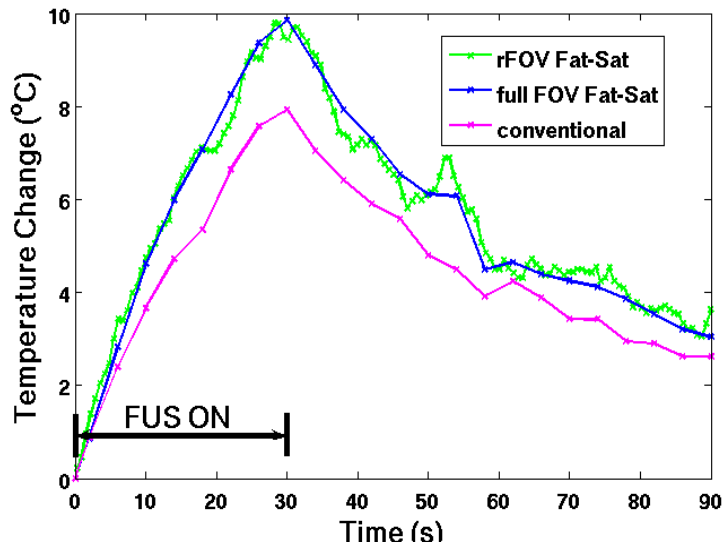


Figure 6-5: Temperature changes of the hottest voxel in 2D cheese experiments. While the conventional sequence (magenta) underestimated temperatures due to the presence of fat, the present method (green) suppressed fat and reduced imaging time by eight-fold, resulting in a temporal resolution of 480 ms. Green line is the result of temporal average over a sliding window of eight time frames.

The rFOV 3D temperature measurements are shown in Figure 6-6. temperature changes in five out of eight slices are displayed within a 3×3 ROI in the focus. The heating in the central slice (i.e., slice # 5, shown in red) showed maximum temperature changes up to 20°C, while the heating in its neighbor slices (i.e., slices # 4 and 6, shown in blue) showed temperature changes of 5°C . For even further slices (i.e., slices # 3 and 7, shown in green), no temperature changes were observed over the time course of monitoring. With the accelerated sequence, in-plane coverage is reduced by a factor of eight and through-plane coverage is increased by the same amount. Accordingly, the ROI (focus) was imaged in 3D with the scan time as same as the conventional full FOV 2D sequence. The scan time for the 3D acquisition is 3.8 s.

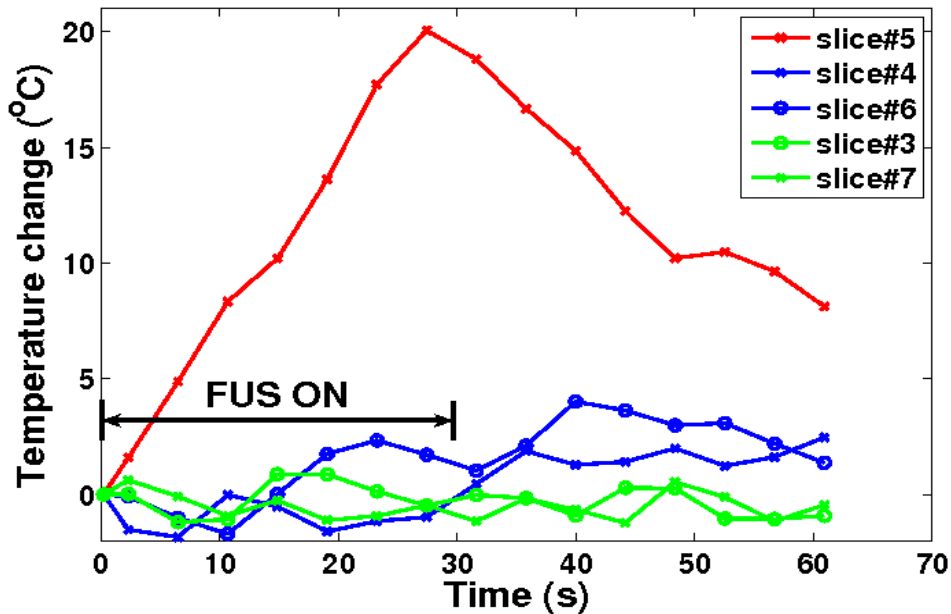


Figure 6-6: Temperature changes of a 3×3 ROI within focus for five (out of eight) slices in the 3D cheese heating experiments. The central slice (red) contained ultrasound focus and exhibited maximum temperature changes. The neighbor slices (blue and green) showed little or no temperature changes as they were at least 5 mm away from the focus. The temporal resolution remained the same as a conventional 2D thermometry (3.8 sec/measurement), but scan efficiency was increased by eight-fold in terms of the focus' coverage.

## 6.4 Discussion

We have demonstrated that the proposed hybrid method, combining 2DRF pulses, SENSE, and UNFOLD, can fulfill both tasks at once, suppressing fat signals in the ROI while exciting only portions of the FOV, which enables accurate and fast imaging with reduced FOV. Accurate temperature measurements were achieved in a cheese phantom with temporal resolution of 480 ms, an eight-fold improvement as compared to a conventional 2D-thermometry sequence. The hybrid method was also implemented in a 3D sequence, where the scan efficiency was improved in terms of the ROI's spatial coverage, rather than temporal resolution.

Other fat-suppression methods may be considered for temperature mapping, such as the use of spectrally selective RF pulse [116], short tau inversion recovery (STIR) [117], and Dixon methods [118, 119]. These approaches, however, could not provide the option for fast imaging. Some of them even increase scan time.

The main drawback of the proposed method is its sensitivity to off-resonance effects, such as  $B_0$  inhomogeneity, susceptibility, and PRF shifts induced by heating itself [83]. Such local resonance frequency shifts may lead to spatial shifts in temperature maps, resulting in inaccurately locating lesion. A good magnetic shimming could keep field inhomogeneity to a minimum and overcome the  $B_0$  inhomogeneity and susceptibility artifacts. Moreover, since the heating-induced PRF shift could be predicted, a careful calibration of the 2DRF pulse could alleviate the distortion caused by heating.

To conclude, accurate and fast MR thermometry using a hybrid method combining 2DRF, parallel imaging, and UNFOLD, was implemented. It enables both fat

suppression and rFOV imaging. This technique is promising for real-time temperature monitoring of FUS thermal therapies in adipose organs.

## 7 Appendix B: The modification of the hybrid method from GRE to EPI

### 7.1 Introduction

EPI is one of the fastest MRI pulse sequences [61]. It differs from conventional pulse sequence, such as GRE, in that the manner in which the readout and phase-encoding gradients are applied. The difference is most clearly understood when considering their  $k$ -space trajectories. In a typical GRE sequence a single  $k$ -space line is acquired (or sampled) in one TR period, whereas in EPI multiple  $k$ -space lines are acquired in one TR. The hybrid method described in Chapter 3 is based on modifications to the RF pulse design (2DRF), modification to the reconstruction using data from receiver coil array (parallel imaging), and use of a special temporal sampling strategy (UNFOLD). These sequence modifications that are applied in implementing the method do not require that the sequence is a GRE as was used in Chapter 3. The method can be incorporated into a pulse sequence with a variety of  $k$ -space trajectories. In this study, we merged the hybrid technique into an EPI pulse sequence to further reduce acquisition time. A 3D EPI sequence was implemented to enable volumetric MR thermometry.

Transcranial MR-guided focused ultrasound therapy [52, 120] was proffered for demonstration of the fast 3D thermometry. In TcMRgFUS therapy, fast temperature monitoring in 3D is essential to avoid overheating the skull and to detect secondary heating sites away from the focal point [51]. The hybrid method seems especially appropriate for this application. In TcMRgFUS therapy, a water bath surrounding the head provides acoustic coupling and an unusually large FOV is required to accommodate

it, resulting in a longer scan time. The 2DRF pulse could suppress excitation from the water bath along phase-encoding direction, and reduce scan time if rFOV imaging is used. Along with UNFOLD and parallel imaging, fast 3D temperature monitoring in a human skull phantom was achieved with temporal resolution of about 1 second and isotropic spatial resolution of  $3\times 3\times 3$  mm.

## 7.2 Materials and methods

A GE product EPI sequence was modified to incorporate the hybrid method for 3D acquisitions. The entire slab volume was excited on each TR period while one  $k$ -space  $k_x$ - $k_y$  section is acquired using standard EPI readout gradients and phase-encode blips. The data for one  $k_x$ - $k_y$  plane was obtained on each TR. A 3D  $k$ -space dataset comprise of all  $k_z$  planes were acquired with a series of TRs (number of TRs = number of planes). The pulse sequence is shown in Figure 7-1. Before rFOV imaging is applied, sixty-four echoes are acquired in one TR of 60 ms and there are fifty slice-encoding steps to acquire 50 slices (planes). The non-accelerated 3D EPI acquisition gave a temporal resolution of 3s (= 50 slices  $\times$  60 ms/slice).

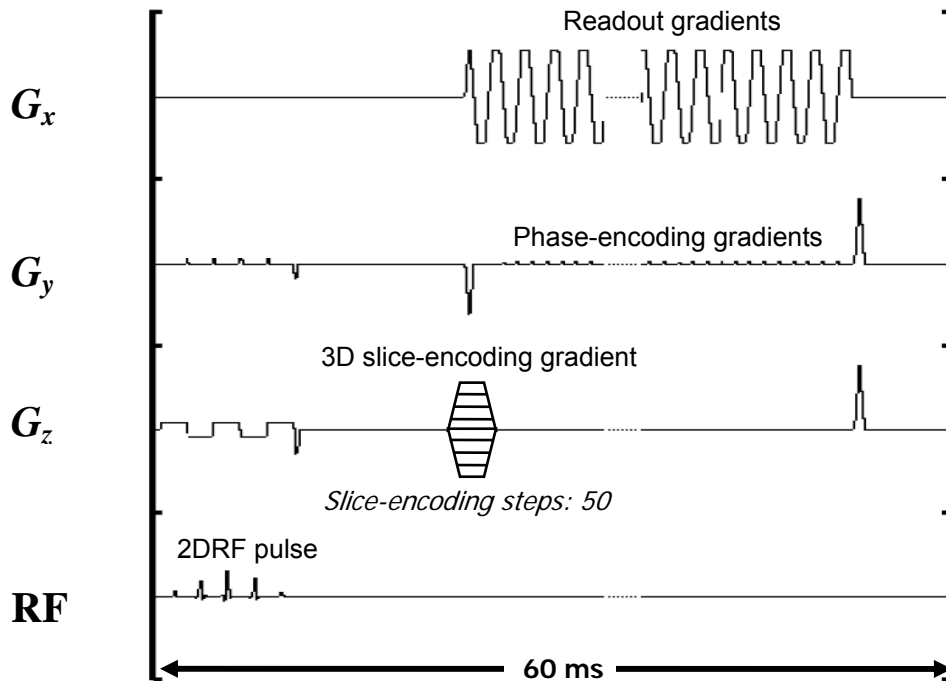


Figure 7-1: The modified 3D-EPI pulse sequence diagram in one TR. 2DRF consists of 5 subpulses with total pulse width of 6 ms. There are 64 echoes in one TR of 60 ms. A total of fifty planes are acquired in fifty encoding steps. With this plot, we are able to achieve temporal resolution of 3s.

With a 2DRF pulse along with rFOV imaging where the reduced FOV is in phase-encoding direction, we can reduce the ETL, and therefore mitigate off-resonance artifacts caused by the long ETL. In addition, reducing ETL shortens TR, leading to some reduced acquisition time. In this case, the reduction of the temporal resolution is not significant (only due to the shorter TR). In Figure 7-1, for example, even though the ETL is cut by half and TR can be diminished to about 40 ms, the total scan time is 2 s (= 50 slices  $\times$  40 ms/slice), which is only a 1.5-fold acceleration. To significantly speed up acquisition, we also need to reduce the number of encoding steps. This was done in this study by combining the UNFOLD and GRAPPA methods.

UNFOLD is a fast imaging technique that manipulates the time evolution of aliased signals by shifting the sampling function from time frame to time frame in acquisition  $k$ -space (see Sec. 2.3.2 for details). GRAPPA is a parallel imaging technique used to speed up MRI pulse sequences [99]. The main differences between GRAPPA and SENSE (see Section 2.4.3) are that in GRAPPA the image is constructed in frequency domain (i.e.,  $k$ -space), before Fourier transformation, and GRAPPA requires additional lines in the center of  $k$ -space. GRAPPA has been shown to be well suited for EPI due to the fact that the  $k$ -space based reconstruction of missing data is not affected by image distortion, a problem found in SENSE with EPI sequence [121]. In our implementation, UNFOLD and GRAPPA were both applied along the  $k_z$  direction. Figure 7-2 illustrates how UNFOLD was applied in conjunction with GRAPPA. The left diagram represents the full set of 3D  $k$ -space data that is acquired in odd time intervals while the right represents the data in even time intervals. The full 3D  $k$ -space data consists of red, green

and black planes. The red planes represent data that were actually acquired. The green and the black planes represent the data acquisition that was skipped due to the use of UNFOLD and GRAPPA, respectively. Other than at the center of  $k$ -space, only every fourth  $k_z$  dataset was acquired and missing  $k_z$  datasets were reconstructed by UNFOLD and GRAPPA. A total of 3-fold temporal acceleration was achieved with such acquisition scheme.

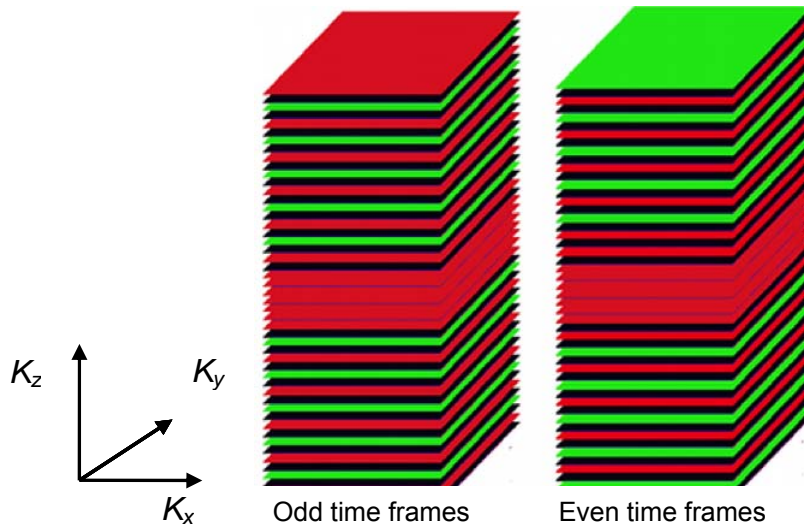


Figure 7-2: Diagram of the 3D  $k$ -space sampling function, for UNFOLD-GRAPPA acquisition. Red planes represent acquired data while green and black ones represent reconstructed data using UNFOLD and GRAPPA. UNFOLD was used to reconstruct the green  $k_z$  planes and GRAPPA was used to reconstruct black  $k_z$  planes.

A FUS heating experiment of a gel phantom was conducted in a 3-Tesla GE scanner using a GE eight-channel head coil. The experimental setup was described in detail in Section 2.2.1. Initial baseline scans were acquired before heating, and then sonication was performed for 30 s at 15 W, using a 1.5 MHz transducer. Additional images were acquired during cooling. The 3D EPI acquisitions with 2×UNFOLD and 2×GRAPPA were performed to monitor the temperature changes. The imaging

parameters were as follows: TE/TR: 30/60ms, readout bandwidth:  $\pm 100$  kHz, flip angle:  $15^\circ$ , ETL: 64, FOV:  $192 \times 192 \times 150$  mm, matrix size:  $64 \times 64 \times 17$ , spatial resolution: 3 mm isotropic, temporal resolution: 1 s. High order shim (1<sup>st</sup> and 2<sup>nd</sup> order) was applied in the phantom to mitigate the distortion artifacts.

A second heating experiment was performed with FUS through a human skull in a 3-Tesla scanner. u Imaging was performed using the GE eight-channel cardiac coil. The experimental set-up is shown in Figure 7-3. A 1.1 MHz array-transducer operated at mode 0, as described in Section 2.1, was used to deliver acoustic energy. A human skull was partially filled with agar and placed in a water tank in between the transducer and a gel phantom. Fifty coronal slices were prescribed to cover the skull. High-order-shim was applied in regions where the heating was expected (i.e., the skull base and the focus). Signal from the water tank was suppressed by the 2DRF pulse. During 30-s sonication at 20 W, the accelerated 3D EPI sequence (2 $\times$ UNFOLD and 2 $\times$ GRAPPA along slice-encoding direction, FOV reduced by 35% along phase-encoding direction) was performed to monitor the temperature changes over the skull. The imaging parameters were as follows: TE/TR: 30/60ms, readout bandwidth:  $\pm 100$  kHz, flip angle:  $15^\circ$ , ETL: 42, FOV:  $192 \times 192 \times 150$  mm, matrix size:  $64 \times 42 \times 17$ , spatial resolution: 3 mm isotropic, temporal resolution: 1 s.

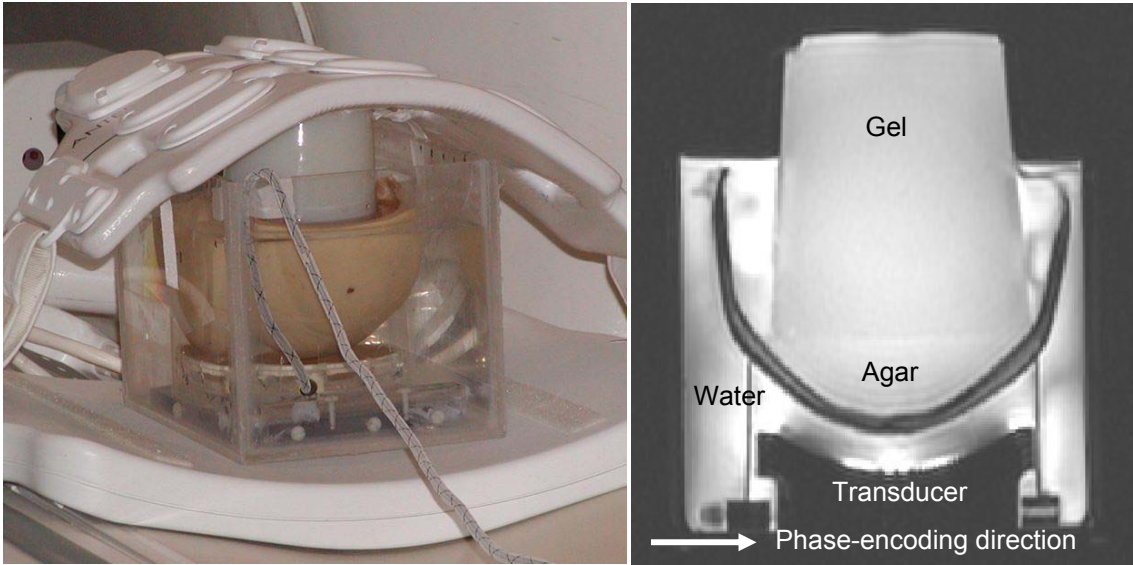


Figure 7-3: Experimental set-up for the human skull heating experiments. Transducer of 1.1 MHz was attached on the bottom of the water tank. A plastic holder was used to hold the skull. In the bottom of the human skull, agar was filled to provide acoustic coupling. Gel phantom was placed on the top of the agar for heating and imaging medium.

In all heating experiments, temperature changes were estimated through phase differences based on temperature dependence of proton resonance frequency shift [84].

### 7.3 Results

In the gel heating experiments, MR temperature measurements for voxels at and away from the focal point for the accelerated 3D EPI case (2×UNFOLD and 2×GRAPPA along slice encoding) are shown in Figure 7-4. Curves in red are displayed for the four hottest, adjacent voxels in the plane perpendicular to FUS beam. Measurements in a voxel 12 mm away from the focus are also shown in blue. A temporal resolution of 1 s was achieved for the accelerated case, which is a 3× improvement compared to the fully-acquired case (4-fold subsampled outer  $k$ -space regions and fully-acquired central region, for a net acceleration of 3). The noise level was measured at 0.2°C (standard deviation through time, averaged over the region away from ultrasound beam).

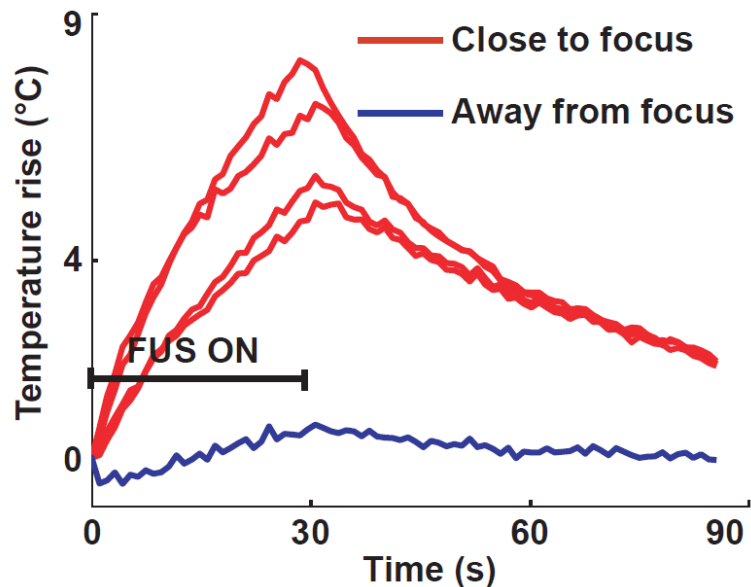


Figure 7-4: MR temperature measurements using 3D EPI in the gel heating experiment. Temperature changes were monitored with the accelerated 3D EPI sequence (2×UNFOLD and 2×GRAPPA). Heating curves are shown for the four hottest voxels at focus (red), and for a voxel away from focus (blue). The acquisition rate was one 3D volume per second. Noise level was 0.2°C.

In the skull heating experiments, temperature rise of the skull was observed in the agar close to the skull, and focal heating was obtained in the gel phantom. Figure 7-5 shows the temperature maps of different slices in the 3D volume at the time point with the maximum heating (i.e., the time point when FUS stopped). Figure 7-5a displays the temperature map of the slice at the skull bottom. The skull heating was conducted to the agar and maximum temperature rise of 1.5°C was observed in the agar. Temperature rise was also observed in the water; however the measurements were not reliable probably due to phase fluctuations from movement in the water. The skull itself does not provide MR signal and therefore should not show temperature rise. The temperature rise seen in the skull is due to partial volume effect (the cross section of the skull consisted of some water). Figure 7-5b displays the temperature map of the slice 9 mm away from the slice in Figure 7-5a. Maximum temperature rise of 1.0°C was observed in the agar. The rise was not as large as in Figure 7-5a, as expected, since this slice is further away from the transducer. Figure 7-5c displays the temperature map of the slice containing the focus. The slice was 78 mm away from the slice in Figure 7-5a. We do not expect to see a temperature rise in the skull in this slice because the ultrasound beam did not travel through this part of the skull. We also did not expect much heating in the focus area since most of the energy was absorbed by the skull. A temperature rise of 0.5°C was observed in the focus area in the gel phantom. Temperature noise was measured at 0.2°C (estimated by standard deviation through time, averaged over the region away from ultrasound beam) for these slices.

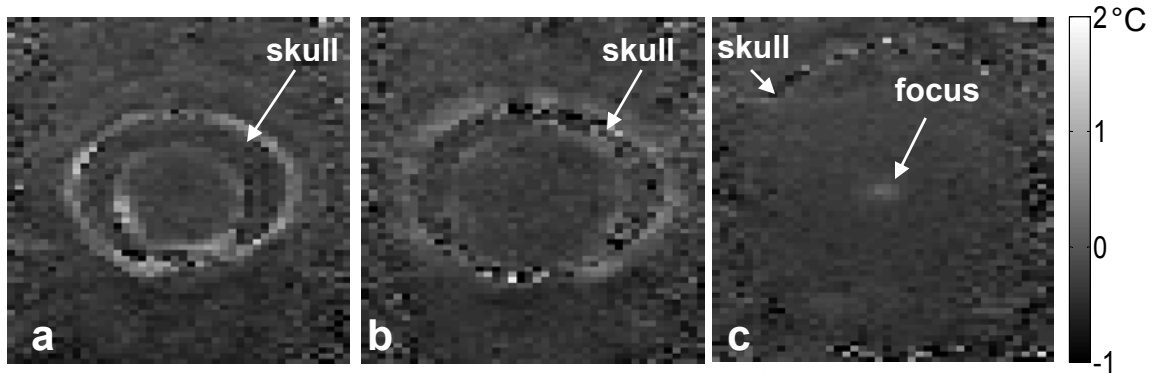


Figure 7-5: Thermal maps of various slices with the maximum temperature rises in the skull heating experiments. a) Temperature map of the slice in the skull bottom. Heating occurred inside skull in the agar and outside skull in the water. b) Temperature map of the slice 9 mm away from the slice in (a). Heating occurred inside and outside skull but temperature rise was not as large as in (a). c) Temperature map of the slice containing focus. Heating was not observed in agar since ultrasound beam did not pass the skull in this slice. Temperature rises of 1.5, 1.0, and 0.5°C were observed in (a), (b), and (c), respectively. Temperature noise was 0.2°C.

## 7.4 Discussion

The hybrid method implemented in a 3D EPI sequence was demonstrated. With the EPI sequence where one plane of  $k$ -space data was acquired in one TR of 60 ms, a 3D volume of fifty slices was achieved with a temporal resolution of 3 s. With 2×UNFOLD and 2×GRAPPA applied in the  $k_z$ -encoding direction, the acquisition time was reduced to 1 s. Further improvement in temporal resolution was gained when the 2DRF pulse and rFOV imaging were applied in the phase-encoding direction.

Currently 2×UNFOLD and 2×GRAPPA were performed in the  $k_z$ -encoding direction, allowing a net acceleration of 3. To further decrease the scan time, UNFOLD and GRAPPA could also be performed in the  $k_y$ -encoding direction. By applying additional 2×GRAPPA in a second encoding direction, the ETL was reduced from 64 to 40, allowing scan time to be reduced from 1s to 0.82s (results not shown).

As compared to regular gradient echo sequences, EPI allows higher frame rate at a price in terms of increased image distortion resulting from the long ETL. Distortion can be mitigated to some degree through the use of high order shimming. But in addition to good shimming, the use of acceleration in phase-encoding direction can also help reduce distortion, through a reduction in the ETL.

The use of GRAPPA by itself could provide an acceleration of 3 with the eight-channel coil. In the hybrid method, however, UNFOLD was used for the main accelerating technique. It is because of so-called g-factor noise enhancement in parallel imaging. The more the acquisition gets accelerated by parallel imaging, the more the g-factor effect comes in. Furthermore, the g-factor artifact happens right around the center

of the imaging subject, which is around the locations of foci in the ExAblate 4000 TcMRgFUS system. Therefore, we can not accelerate too much with GRAPPA, even though theoretically eight-fold acceleration is achievable when an eight-channel coil is used, and UNFOLD was used instead to accelerate the acquisition.

As mentioned in Appendix A, the presence of fat would degrade the temperature accuracy. The proposed method is compatible with 2DRF pulses featuring fat-suppression capabilities [107, 108, 115].

The main drawback of this technique is the low spatial resolution, which is 3 mm isotropic. When focal heating is smaller than 3 mm, partial volume effects can be a problem. However, the half-width-full-maximum focal region produced by the InSightec's TcMRgFUS system is roughly 3.0x3.0x5.8 mm (according to specifications provided by the manufacturer), and therefore the 3 mm isotropic spatial resolution should be high enough to avoid serious voxel averaging effect in our target system. When higher spatial resolution is needed, we could consider combining this hybrid method with a multi-resolution acquisition strategy [122], which permits higher spatial resolution in the region of the focal heating while maintaining volumetric coverage with the same temporal resolution.

To conclude, by combining the strengths of UNFOLD, GRAPPA, and 2DRF methods, 3D MR temperature imaging could be performed here with a frame rate of about 1 fps, while maintaining reasonable values for the matrix size and echo train length.

## 8 Appendix C: Publication list

### Publications

Chang-Sheng Mei, Robert V. Mulkern, Koichi Oshio, Nan-kuei Chen, Bruno Madore, Lawrence P. Panych, Kullervo Hynynen, Nathan J. McDannold, “Ultrafast 1D MR thermometry using phase or frequency mapping”, *Magn. Reson. Mater. Phys. Biol. Med.*, published online: 29 Jul 2011, DOI: 10.1007/s10334-011-0272-9

Chang-Sheng Mei, Lawrence P. Panych, Jing Yuan, Nathan J. McDannold, Lisa H. Treat, Yun Jing, Bruno Madore, “Combining Two-Dimensional Spatially Selective RF Excitation, Parallel Imaging and UNFOLD for Accelerated MR Thermometry Imaging”, *Magn. Reson. Med.*, Jul 2011, 66(1): 112-122

Jing Yuan, Chang-Sheng Mei, Bruno Madore, Nathan J. McDannold, Lawrence P. Panych, “Fast fat-suppressed reduced field-of-view temperature mapping using 2D RF excitation pulses”, *J. Magn. Reson.*, May 2011, 210(1): 38-43

Bruno Madore, Lawrence P. Panych, Chang-Sheng Mei, Jing Yuan, Renxin Chu, “Multi-pathway sequences for MR thermometry”, *Magn. Reson. Med.*, Sep 2011, 66(3): 658-68

Nathan J. McDannold, Eun-Joo Park, Chang-Sheng Mei, Eyal Zadicario, Ferenc Jolesz, “Evaluation of Three-Dimensional Temperature Distributions Produced by a Low-Frequency Transcranial Focused Ultrasound System Within Ex Vivo Human Skulls”, *IEEE Trans. Ultrason. Ferroelectr. Freq. Control*, Sep 2010, 57(9): 1967-76

### Conference Proceedings

Chang-Sheng Mei, Onur Afcan, Jing Yuan, Lawrence P. Panych, Bruno Madore, Nathan J. McDannold, “Multi-shot high-speed 3D-EPI thermometry using a hybrid method combining 2DRF excitation, parallel imaging, and UNFOLD”, in: *Proceedings of the Nineteenth Meeting of the International Society for Magnetic Resonance in Medicine. Montreal, Canada, 2011*

Bruno Madore, Renxin Chu, Chang-Sheng Mei, Jing Yuan, Tzh-Chen Chao, Lawrence P. Panych, “Modified EPI sequence for improved MR thermometry”, in: *Proceedings of the Nineteenth Meeting of the International Society for Magnetic Resonance in Medicine. Montreal, Canada, 2011*

Nathan J. McDannold, Eun-Joo Park, Chang-Sheng Mei, Eyal Zadicario, Ferenc Jolesz, “Evaluation of three-dimensional temperature distributions produced by a low-frequency transcranial focused ultrasound system within ex vivo human skulls”, in: *IEEE International Ultrasonics Symposium, San Diego, USA, 2010*

Chang-Sheng Mei, Jing Yuan, Lawrence P. Panych, Bruno Madore, Nathan J. McDannold, “3D reduced-FOV MR thermometry with fat suppression using a hybrid

method combining a 2DRF pulse, parallel imaging, and UNFOLD”, in: *Proceedings of the Eighteenth Meeting of the International Society for Magnetic Resonance in Medicine. Stockholm, Sweden, 2010*

Bruno Madore, Lawrence P. Panych, Chang-Sheng Mei, Renxin Chu, “Dual-Echo Sequence for MR Thermometry in Moving Objects”, in: *Proceedings of the Eighteenth Meeting of the International Society for Magnetic Resonance in Medicine. Stockholm, Sweden, 2010*

Bruno Madore, Lawrence P. Panych, Chang-Sheng Mei, Renxin Chu, “MR Thermometry in Moving Objects Using a Novel Referenceless and User-Independent Approach”, in: *Proceedings of the Eighteenth Meeting of the International Society for Magnetic Resonance in Medicine. Stockholm, Sweden, 2010*

Chang-Sheng Mei, Jing Yuan, Nathan J. McDannold, Lawrence P. Panych, “Fast Temperature Measurement Using a 2DRF Pulse Enables Both Reduced-FOV Imaging and Fat Suppression”, in: *Proceedings of the Seventeenth Meeting of the International Society for Magnetic Resonance in Medicine. Honolulu, USA, 2009*

Bruno Madore, Jing Yuan, Chang-Sheng Mei, Lawrence P. Panych, “Fast Imaging Sequence for Temperature Monitoring in Moving Objects”, in: *Proceedings of the Seventeenth Meeting of the International Society for Magnetic Resonance in Medicine. Honolulu, USA, 2009*

Chang-Sheng Mei, Jing Yuan, Bruno Madore, Nathan J. McDannold, Lawrence P. Panych, “Combining 2D RF Excitation, Parallel Imaging and UNFOLD in Focused Ultrasound Heating Experiment”, in: *Proceedings of the Sixteenth Meeting of the International Society for Magnetic Resonance in Medicine. Toronto, Canada, 2008*

Jing Yuan, Chang-Sheng Mei, Lawrence P. Panych, “Ultra-Short 2D RF Pulse for Reduced Field-Of-View SSFP Imaging”, in: *Proceedings of the Sixteenth Meeting of the International Society for Magnetic Resonance in Medicine. Toronto, Canada, 2008*

Zientara G, Chu R, Hoge S, Madore, Tokuda J, Liu H, Hata N, Mei C-S, Panych L, “Real-time MR Data Acquisition System for IGT in the AMIGO Suite”, in: *Proceedings of the Seventh Interventional MRI Symposium. Baltimore, USA, 2008*

## 9 Appendix D: Abbreviations

Abbreviation	Translation
2DRF	two-dimensional spatially selective RF
BW	bandwidth
°C	degrees centigrade
cm	centimeters
EPI	echo planar imaging
ETL	echo train length of EPI pulse sequence
FFT	fast Fourier transform
FOV	field of view
SPGR	spoiled gradient echo
FUS	focused ultrasound
G	Gauss
GRAPPA	one of the parallel imaging techniques: generalized auto-calibrating partially parallel acquisitions
GRE	gradient echo sequence
h	hour
Hz	Hertz
LSEPSI	line scan echo-planar spectroscopic imaging
m	meters
MHz	megahertz
MRI	Magnetic resonance imaging
min	minutes
mm	millimeters
ms	milliseconds
NEX	number of excitations
ppm	parts per million
PRF	proton resonance frequency
PVC	polyvinyl chloride
RF	radio frequency
rFOV	reduced FOV
ROI	region of interest
s	seconds
SENSE	one of the parallel imaging techniques: sensitivity encoding for fast MRI
SNR	signal to noise ratio
SPGR	spoiled gradient echo
T	Tesla
TcMRgFUS	transcranial MR-guided focused ultrasound

TE	echo time of a MRI pulse sequence
TNR	temperature to noise ratio
TR	repetition time of a MRI pulse sequence
UNFOLD	unaliasing by Fourier-encoding the overlaps using the temporal dimension
W	Watts

---

**Table 9-1: Abbreviations used in this thesis**

## 10 References

- 1 Jolesz FA, McDannold N (2008) Current status and future potential of MRI-guided focused ultrasound surgery. *J Magn Reson Imaging* 27:391-399.
- 2 Hall LD, Talagala SL (1985) Mapping of pH and Temperature Distribution Using Chemical-Shift-Resolved Tomography. *J Magn Reson* 65:501-505.
- 3 Lutz NW, Kuesel AC, Hull WE (1993) A <sup>1</sup>H-NMR method for determining temperature in cell culture perfusion systems. *Magn Reson Med* 29:113-118.
- 4 Kuroda K, Oshio K, Chung AH, et al. (1997) Temperature mapping using the water proton chemical shift: A chemical shift selective phase mapping method. *Magn Reson Med* 38:845-851.
- 5 Kuroda K, Oshio K, Mulkern RV, et al. (1998) Optimization of chemical shift selective suppression of fat. *Magn Reson Med* 40:505-510.
- 6 Todd N, Vyas U, de Bever J, et al. (2011) The effects of spatial sampling choices on MR temperature measurements. *Magn Reson Med* 65:515-521.
- 7 Weidensteiner C, Quesson B, Caire-Gana B, et al. (2003) Real-time MR temperature mapping of rabbit liver in vivo during thermal ablation. *Magn Reson Med* 50:322-330.
- 8 Stafford RJ, Price RE, Diederich CJ, et al. (2004) Interleaved echo-planar imaging for fast multiplanar magnetic resonance temperature imaging of ultrasound thermal ablation therapy. *J Magn Reson Imaging* 20:706-714.
- 9 Stafford RJ, Hazle JD, Glover GH (2000) Monitoring of high-intensity focused ultrasound-induced temperature changes in vitro using an interleaved spiral acquisition. *Magn Reson Med* 43:909-912.
- 10 de Zwart JA, Vimeux FC, Delalande C, et al. (1999) Fast lipid-suppressed MR temperature mapping with echo-shifted gradient-echo imaging and spectral-spatial excitation. *Magn Reson Med* 42:53-59.
- 11 de Zwart JA, Vimeux FC, Palussiere J, et al. (2001) On-line correction and visualization of motion during MRI-controlled hyperthermia. *Magn Reson Med* 45:128-137.
- 12 Scheffler K (2004) Fast frequency mapping with balanced SSFP: theory and application to proton-resonance frequency shift thermometry. *Magn Reson Med* 51:1205-1211.
- 13 Paliwal V, El-Sharkawy AM, Du XY, et al. (2004) SSFP-based MR thermometry. *Magn Reson Med* 52:704-708.
- 14 Rieke V, Hargreaves B, Butts Pauly K (2006) PRF shift thermometry using multiple-acquisition phase-cycled SSFP. *Proc Interv MRI Symp*:39.

- 15 Weidensteiner C, Kerioui N, Quesson B, et al. (2004) Stability of real-time MR temperature mapping in healthy and diseased human liver. *J Magn Reson Imaging* 19:438-446.
- 16 Bankson JA, Stafford RJ, Hazle JD (2005) Partially parallel imaging with phase-sensitive data: Increased temporal resolution for magnetic resonance temperature imaging. *Magn Reson Med* 53:658-665.
- 17 Holbrook AB, Santos JM, Kaye E, et al. (2010) Real-Time MR Thermometry for Monitoring HIFU Ablations of the Liver. *Magn Reson Med* 63:365-373.
- 18 Hardy CJ, Cline HE (1989) Spatial Localization in 2 Dimensions Using Nmr Designer Pulses. *J Magn Reson* 82:647-654.
- 19 Pauly J, Nishimura D, Macovski A (1989) A K-Space Analysis of Small-Tip-Angle Excitation. *J Magn Reson* 81:43-56.
- 20 Hynynen K, Lulu BA (1990) Hyperthermia in Cancer Treatment. *Invest Radiol* 25:824-834.
- 21 Hynynen K (1990) Biophysics and technology of ultrasound hyperthermia. In: Gautherie M (ed) *Methods of External Hyperthermic Heating*. Springer-Verlag, New York, pp 61-115.
- 22 Lalonde R (1995) Variable frequency field conjugate lenses for ultrasound hyperthermia. *IEEE Trans Ultrason Ferroelectr Freq Contr* 42:825.
- 23 Fjield T, Sorrentino V, Cline H, et al. (1997) Design and experimental verification of thin acoustic lenses for the coagulation of large tissue volumes. *Phys Med Biol* 42:2341-2354.
- 24 Cain C, Umemura S (1986) Concentric-ring and sector-vortex phased-array applicators for ultrasound hyperthermia. *IEEE Trans Microw Theory Tech* 34:542-551.
- 25 Hynynen K, Chung A, Fjield T, et al. (1996) Feasibility of using ultrasound phased arrays for MRI monitored noninvasive surgery. *IEEE Trans Ultrason Ferroelectr Freq Contr* 43:1043.
- 26 Daum D, Smith N, King R, et al. (1999) In vivo demonstration of non-invasive thermal surgery of the liver and kidney using an ultrasonic phased array. *Ultrasound Med Biol* 25:1087-1098.
- 27 Clement G, Sun J, Giesecke T, et al. (2000) A hemisphere array for non-invasive ultrasound brain therapy and surgery. *Phys Med Biol* 45:3707-3719.
- 28 Duck FA, Baker AC, Starritt HC (1998) *Ultrasound in medicine*. Bristol, Philadelphia.
- 29 Sokka SD, King R, K H (2003) MRI-guided gas bubble enhanced ultrasound heating in in vivo rabbit thigh. *Phys Med Biol* 48:223-241.

- 30 Kim J, Hahn E (1979) Clinical and biological studies of localized hyperthermia. *Cancer Res* 39:2258-2261.
- 31 Thomsen S (1991) Pathologic analysis of photothermal and photomechanical effects of laser-tissue interactions. *Photochem Photobiol* 53:825-835.
- 32 Pennes H (1948) Analysis of tissue and arterial blood temperatures in the resting human forearm. *J Appl Physiol* 1:93-122.
- 33 Billard B, Hynynen K, Roemer R (1990) Effects of physical parameters on high temperature ultrasound hyperthermia. *Ultrasound Med Biol* 16:409-420.
- 34 ter Haar G (2001) High intensity focused ultrasound for the treatment of tumors. *Echocardiography* 18:317-322.
- 35 Vaezy S, Martin R, Schmiedl U, et al. (1997) Liver hemostasis using high-intensity focused ultrasound. *Ultrasound Med Biol* 23:1413-1420.
- 36 Raymond S, Treat L, Dewey J, et al. (2008) Ultrasound enhanced delivery of molecular imaging and therapeutic agents in Alzheimer's disease mouse models. *PLoS ONE* 3:e2175.
- 37 Lynn JG, Zwemer RL, et al. (1942) A new method for the generation and use of focused ultrasound in experimental biology. *J Gen Physiol* 26:179-193.
- 38 Fry W, Barnard J, Fry E, et al. (1955) Ultrasonic lesions in the mammalian central nervous system. *Science* 122:517-518.
- 39 Fry W, Fry F (1960) Fundamental neurological research and human neurosurgery using intense ultrasound. *IRE Trans Med Electron* ME-7:166-181.
- 40 Lele P (1962) A simple method for production of trackless focal lesions with focused ultrasound: Physical factors. *J Physiol* 160:494-512.
- 41 Lele P (1967) Production of deep focal lesions by focused ultrasound--current status. *Ultrasonics* 5:105-112.
- 42 Kennedy J (2005) High-intensity focused ultrasound in the treatment of solid tumours. *Nat Rev Cancer* 5:321-327.
- 43 Dubinsky T, Cuevas C, Dighe M, et al. (2008) High-intensity focused ultrasound: current potential and oncologic applications. *AJR Am J Roentgenol* 190:191-199.
- 44 (2001) Proceedings of the first international workshop on the application of high intensity focused ultrasound (HIFU) in medicine.
- 45 Cline H, Schenck J, Hynynen K (1992) MR-guided focused ultrasound surgery. *J Comput Assist Tomogr* 16:956-965.
- 46 Hynynen K, Darkazanli A, Unger E, et al. (1993) MRI-guided noninvasive ultrasound surgery. *Med Phys* 20:107-115.

- 47 Hynynen K, Pomeroy O, Smith D, et al. (2001) MR imaging-guided focused ultrasound surgery of fibroadenomas in the breast: a feasibility study. *Radiology* 219:176-185.
- 48 Huber P, Jenne J, Rastert R, et al. (2001) A new noninvasive approach in breast cancer therapy using magnetic resonance imaging-guided focused ultrasound surgery. *Cancer Res* 61:8441-8447.
- 49 Gianfelice D, Khiat A, Amara M, et al. (2003) MR imaging-guided focused US ablation of breast cancer: histopathologic assessment of effectiveness-- initial experience. *Radiology* 227:849-855.
- 50 Hynynen K, Freund W, Cline H, et al. (1996) A clinical, noninvasive, MR imaging-monitored ultrasound surgery method. *Radiographics* 16:185-195.
- 51 McDannold N, Park E-J, Mei C-S, et al. (2010) Evaluation of Three-Dimensional Temperature Distributions Produced by a Low-Frequency Transcranial Focused Ultrasound System Within Ex Vivo Human Skulls. *IEEE Transactions on Ultrasonics Ferroelectrics and Frequency Control* 57:1967-1976.
- 52 Martin E, Jeanmonod D, Morel A, et al. (2009) High-Intensity Focused Ultrasound for Noninvasive Functional Neurosurgery. *Ann Neurol* 66:858-861.
- 53 Hynynen K, Vykhodtseva N, Chung A, et al. (1997) Thermal effects of focused ultrasound on the brain: determination with MR imaging. *Radiology* 204:247-253.
- 54 McDannold NJ, King RL, Jolesz FA, et al. (2000) Usefulness of MR imaging-derived thermometry and dosimetry in determining the threshold for tissue damage induced by thermal surgery in rabbits. *Radiology* 216:517-523.
- 55 Hazle J, Stafford R, Price R (2002) Magnetic resonance imaging-guided focused ultrasound thermal therapy in experimental animal models: correlation of ablation volumes with pathology in rabbit muscle and VX2 tumors. *J Magn Reson Imaging* 15:185-194.
- 56 McDannold N (2005) Quantitative MRI-based temperature mapping based on the proton resonant frequency shift: review of validation studies. *Int J Hyperthermia* 21:533-546.
- 57 Sapareto S, Dewey W (1984) Thermal dose determination in cancer therapy. *Int J Radiat Oncol Biol Phys* 10:787-800.
- 58 Chung A, Jolesz F, Hynynen K (1999) Thermal dosimetry of a focused ultrasound beam in vivo by magnetic resonance imaging. *Med Phys* 26:2017-2026.
- 59 Parker D, Roberts J, Alexander A, et al. (1999) Magnetic resonance angiography with sliding interleaved projection reconstruction (SLIPR) acquisition. *J Magn Reson Imaging* 10:569-575.
- 60 Ahn C, Kim J, Cho Z (1986) High-Speed Spiral-Scan Echo Planar NMR Imaging. *IEEE Trans Med Imaging* MI-5:2-7.

- 61 Mansfield P (1977) Multi-planar image formation using NMR spin echoes. *Journal of Physics C: Solid State Physics* 10:55-58.
- 62 Buonocore M, Gao L (1997) Ghost artifact reduction for echo planar imaging using image phase correction. *Magn Reson Med* 38:89-100.
- 63 Bloembergen N, Purcell E, Pound R (1948) Relaxation Effects in Nuclear Magnetic Resonance Absorption. *Physical Review* 73:679-712.
- 64 Parker D, Smith V, Sheldon P, et al. (1983) Temperature distribution measurements in two-dimensional NMR imaging. *MedPhys* 10:321-325.
- 65 Matsumoto R, Mulkern R, Hushek S, et al. (1994) Tissue temperature monitoring for thermal interventional therapy: comparison of T1-weighted MR sequences. *J Magn Reson Imaging* 4:65-70.
- 66 Graham S, Bronskill M, Henkelman R (1998) Time and temperature dependence of MR parameters during thermal coagulation of ex vivo rabbit muscle. *Magn Reson Med* 39:198-203.
- 67 Graham S, Stanisz G, Kecojevic A, et al. (1999) Analysis of changes in MR properties of tissues after heat treatment. *Magn Reson Med* 42:1061-1071.
- 68 Hynynen K, McDannold N, Mulkern R, et al. (2000) Temperature monitoring in fat with MRI. *Magn Reson Med* 43:901-904.
- 69 Bottomley P, Foster T, Argersinger R, et al. (1984) A review of normal tissue hydrogen NMR relaxation times and relaxation mechanisms from 1-100 MHz: dependence on tissue type, NMR frequency, temperature, species, excision, and age *Med Phys* 11:425-448.
- 70 Anzai Y, Lufkin R, Castro D, et al. (1991) MR imaging-guided interstitial Nd:YAG laser phototherapy: dosimetry study of acute tissue damage in an in vivo model. *J Magn Reson Imaging* 1:553-559.
- 71 Abragam A (1983) *The principles of nuclear magnetism*. Clarendon Press, Oxford.
- 72 Johnson F, Eyring H, Stover B (1974) *Theory of rate processes in biology and medicine*. John Wiley & Sons, New York.
- 73 Simpson J, Carr H (1958) Diffusion and Nuclear Spin Relaxation in Water. *Physical Review* 111:1201-1202.
- 74 le Bihan D, Delannoy J, Levin R (1989) Temperature mapping with MR imaging of molecular diffusion: application to hyperthermia. *Radiology* 171:853-857.
- 75 MacFall J, Prescott D, Fullar E, et al. (1995) Temperature dependence of canine brain tissue diffusion coefficient measured in vivo with magnetic resonance echo-planar imaging. *Int J Hyperthermia* 11:73-86.
- 76 Jackson J (1975) *Classical Electrodynamics*. John Wiley & Sons, New York.
- 77 Philo J, Fairbank W (1980) Temperature dependence of the diamagnetism of water. *J Chem Phys* 72:4429-4433.

- 78 Hindman JC (1966) Proton Resonance Shift of Water in the Gas and Liquid States. *J Chem Phys* 44:4582-4592.
- 79 Peters RD, Hinks R, Henkelman R (1999) Heat-source orientation and geometry dependence in proton-resonance frequency shift magnetic resonance thermometry. *Magn Reson Med* 41:909-918.
- 80 Peters RD, Hinks RS, Henkelman RM (1998) Ex vivo tissue-type independence in proton-resonance frequency shift MR thermometry. *Magn Reson Med* 40:454-459.
- 81 Kuroda K, Chung AH, Hynynen K, et al. (1998) Calibration of water proton chemical shift with temperature for noninvasive temperature imaging during focused ultrasound surgery. *J Magn Reson Imaging* 8:175-181.
- 82 De Poorter J (1995) Noninvasive MRI thermometry with the proton resonance frequency method: study of susceptibility effects. *Magn Reson Med* 34:359-367.
- 83 Sprinkhuizen S, Konings M, van der Bom M, et al. (2010) Temperature-induced tissue susceptibility changes lead to significant temperature errors in PRFS-based MR thermometry during thermal interventions. *Magn Reson Med* 64:1360-1372.
- 84 Ishihara Y, Calderon A, Watanabe H, et al. (1995) A Precise and Fast Temperature Mapping Using Water Proton Chemical-Shift. *Magn Reson Med* 34:814-823.
- 85 Kuroda K (2005) Non-invasive MR thermography using the water proton chemical shift. *Int J Hyperthermia* 21:547-560.
- 86 McDannold N, Barnes AS, Rybicki FJ, et al. (2007) Temperature mapping considerations in the breast with line scan echo planar spectroscopic imaging. *Magn Reson Med* 58:1117-1123.
- 87 Harth T, Kahn T, Rassek M, et al. (1997) Determination of laser-induced temperature distributions using echo-shifted TurboFLASH. *Magn Reson Med* 38:238-245.
- 88 Peters RD, Henkelman RM (2000) Proton-resonance frequency shift MR thermometry is affected by changes in the electrical conductivity of tissue. *Magn Reson Med* 43:62-71.
- 89 Vigen K, Daniel B, Pauly J, et al. (2003) Triggered, navigated, multi-baseline method for proton resonance frequency temperature mapping with respiratory motion. *Magn Reson Med* 50:1003-1010.
- 90 Rieke V, Vigen K, Sommer G, et al. (2004) Referenceless PRF shift thermometry. *Magn Reson Med* 51:1223-1231.
- 91 Grissom W, Rieke V, Holbrook A, et al. (2010) Hybrid referenceless and multibaseline subtraction MR thermometry for monitoring thermal therapies in moving organs. *Med Phys* 37:5014-5026.
- 92 Wlodarczyk W, Hentschel M, Wust P, et al. (1999) Comparison of four magnetic resonance methods for mapping small temperature changes. *Phys Med Biol* 44:607-624.

- 93 Umemura S, Cain C (1989) The sector-vortex phased array: acoustic field synthesis for hyperthermia. *IEEE Trans Ultrason Ferroelectr Freq Contr* 36:249.
- 94 Daum D, Buchanan M, Fjield T, et al. (1998) Design and evaluation of a feedback based phased array system for ultrasound surgery. *IEEE Trans Ultrason Ferroelectr Freq Contr* 45:431-438.
- 95 Madore B, Glover GH, Pelc NJ (1999) Unaliasing by Fourier-encoding the overlaps using the temporal dimension (UNFOLD), applied to cardiac imaging and fMRI. *Magn Reson Med* 42:813-828.
- 96 Madore B (2002) Using UNFOLD to remove artifacts in parallel imaging and in partial-Fourier imaging. *Magn Reson Med* 48:493-501.
- 97 Sodickson DK, Manning WJ (1997) Simultaneous acquisition of spatial harmonics (SMASH): fast imaging with radiofrequency coil arrays. *Magn Reson Med* 38:591-603.
- 98 Kyriakos W, Panych L, Kacher D, et al. (2000) Sensitivity profiles from an array of coils for encoding and reconstruction in parallel (SPACE RIP). *Magn Reson Med* 44:301-308.
- 99 Griswold M, Jakob P, Heidemann R (2002) Generalized autocalibrating partially parallel acquisitions (GRAPPA). *Magn Reson Med* 47:1202-1210.
- 100 Pruessmann KP, Weiger M, Scheidegger MB, et al. (1999) SENSE: Sensitivity encoding for fast MRI. *Magn Reson Med* 42:952-962.
- 101 Zhao L, Madore B, Panych LP (2005) Reduced field-of-view MRI with two-dimensional spatially-selective RF excitation and UNFOLD. *Magn Reson Med* 53:1118-1125.
- 102 Hardy CJ, Marinelli L, Foo TK (2007) Rapid M-mode MRI Using Undersampled 2D Excitation and Parallel Reconstruction. *Conf Proc 15th ISMRM, Berlin, Germany*,:359.
- 103 Gorny KR, Hangiandreou NJ, Hesley GK, et al. (2006) MR guided focused ultrasound: technical acceptance measures for a clinical system. *Phys Med Biol* 51:3155-3173.
- 104 Hayes CE, Roemer PB (1990) Noise Correlations in Data Simultaneously Acquired from Multiple Surface Coil Arrays. *Magn Reson Med* 16:181-191.
- 105 Bland JM, Altman DG (1986) Statistical-Methods for Assessing Agreement between 2 Methods of Clinical Measurement. *Lancet* 1:307-310.
- 106 Chung AH, Hynynen K, Colucci V, et al. (1996) Optimization of spoiled gradient-echo phase imaging for in vivo localization of a focused ultrasound beam. *Magn Reson Med* 36:745-752.
- 107 Mei C-S, Yuan J, Panych LP, et al. (2010) 3D reduced-FOV MR thermometry with fat suppression using a hybrid method combining a 2DRF pulse, parallel imaging, and

- UNFOLD. Conf Proc Joint Annual Meeting ISMRM-ESMRMB, Stockholm, Sweden,;5716.
- 108Yuan J, Madore B, Panych LP (2010) Spatially Varying Fat-Water Excitation Using Short 2DRF Pulses. *Magn Reson Med* 63:1092-1097.
- 109Sung K, Nayak K (2006) Reduced Field-of-View RF Pulse Designs with Fat-Suppression. Conf Proc 14th ISMRM, Seattle, Washington, USA,;3010.
- 110Oshio K, Kyriakos W, Mulkern RV (2000) Line scan echo planar spectroscopic imaging. *Magn Reson Med* 44:521-524.
- 111McDannold N, Hynynen K, Oshio K, et al. (2001) Temperature monitoring with line scan echo planar spectroscopic imaging. *Med Phys* 28:346-355.
- 112Gudbjartsson H, Patz S (1995) The Rician Distribution of Noisy Mri Data. *Magn Reson Med* 34:910-914.
- 113Chu R, Madore B, Panych PL, et al. (2009) Parallel Line Scan Diffusion Imaging with 2D Acceleration. *Proc Int Soc Magn Reson Med* 17:1376.
- 114Ma JF, Wehrli FW, Song HK (1996) Fast 3D large-angle spin-echo imaging (3D FLASE). *Magn Reson Med* 35:903-910.
- 115Yuan J, Mei C-S, Madore B, et al. (2011) Fast fat-suppressed reduced field-of-view temperature mapping using 2DRF excitation pulses. *J Magn Reson* 210:38-43.
- 116Meyer C, Pauly J, Macovski A, et al. (1990) Simultaneous spatial and spectral selective excitation. *Magn Reson Med* 15:287-304.
- 117Fleckenstein J, Archer B, Barker B, et al. (1991) Fast short-tau inversion-recovery MR imaging. *Radiology* 179:499-504.
- 118Dixon WT (1984) Simple proton spectroscopic imaging. *Radiology* 153:189-194.
- 119Glover GH, Schneider E (1991) Three-point Dixon technique for true water/fat decomposition with B<sub>0</sub> inhomogeneity correction. *Magn Reson Med* 18:371-383.
- 120McDannold N, Clement G, Black P, et al. (2010) Transcranial magnetic resonance imaging- guided focused ultrasound surgery of brain tumors: initial findings in 3 patients. *Neurosurgery* 66:323-332.
- 121Blaimer M, Breuer F, Mueller M, et al. (2004) SMASH, SENSE, PILS, GRAPPA: how to choose the optimal method. *Top Magn Reson Imaging* 15:223-236.
- 122Aljallad M, Yuan J, Pilatou M, et al. (2011) Multiresolution MRI temperature monitoring in a reduced field of view. *Magn Reson Imaging*: [PubMed: 21908128].